



# Neural metabolic imbalance induced by MOF dysfunction triggers pericyte activation and breakdown of vasculature

Bilal N. Sheikh <sup>1</sup>, Sukanya Guhathakurta <sup>1,2</sup>, Tsz Hong Tsang <sup>1,2</sup>, Marius Schwabenland <sup>3</sup>, Gina Renschler <sup>1,2</sup>, Benjamin Herquel<sup>1</sup>, Vivek Bhardwaj <sup>1</sup>, Herbert Holz<sup>1</sup>, Thomas Stehle<sup>1</sup>, Olga Bondareva<sup>4</sup>, Nadim Aizarani<sup>1,2</sup>, Omar Mossad <sup>2,3</sup>, Oliver Kretz<sup>5,6</sup>, Wilfried Reichardt <sup>7,8,9</sup>, Aindrila Chatterjee<sup>1</sup>, Laura J. Braun<sup>10</sup>, Julien Thevenon<sup>11,12</sup>, Herve Sartelet<sup>13</sup>, Thomas Blank<sup>3</sup>, Dominic Grün <sup>1</sup>, Dominik von Elverfeldt<sup>7</sup>, Tobias B. Huber<sup>5</sup>, Dietmar Vestweber<sup>10</sup>, Sergiy Avilov<sup>1</sup>, Marco Prinz <sup>3,14,15</sup>, Joerg M. Buescher <sup>1</sup> and Asifa Akhtar <sup>1</sup> ✉

**Mutations in chromatin-modifying complexes and metabolic enzymes commonly underlie complex human developmental syndromes affecting multiple organs. A major challenge is to determine how disease-causing genetic lesions cause deregulation of homeostasis in unique cell types. Here we show that neural-specific depletion of three members of the non-specific lethal (NSL) chromatin complex—*Mof*, *Kansl2* or *Kansl3*—unexpectedly leads to severe vascular defects and brain haemorrhaging. Deregulation of the epigenetic landscape induced by the loss of the NSL complex in neural cells causes widespread metabolic defects, including an accumulation of free long-chain fatty acids (LCFAs). Free LCFAs induce a Toll-like receptor 4 (TLR4)-NFκB-dependent pro-inflammatory signalling cascade in neighbouring vascular pericytes that is rescued by TLR4 inhibition. Pericytes display functional changes in response to LCFA-induced activation that result in vascular breakdown. Our work establishes that neurovascular function is determined by the neural metabolic environment.**

Embryonic development is an exquisitely fine-tuned process that demands the combination of proper gene expression and nutrients, which are utilized by the embryo for energy and basic building blocks of cellular structures. Consistent with this, mutations in both chromatin regulators and metabolic genes commonly underlie developmental syndromes<sup>1–4</sup>. Despite these mutations being present throughout the whole body, their effects on different cell types and organs vary greatly. A number of co-morbidities such as intellectual disability, visual impairments, hypotonia, craniofacial defects, cardiac anomalies, urogenital and kidney dysfunction with differing severities are commonly reported in patients with developmental disorders<sup>5–7</sup>. However, it remains to be ascertained whether a given genetic lesion causes deregulation of the same or dissimilar molecular networks in different cell types. In addition, given the extensive intercellular communication within and between organs, there are likely to be indirect changes in cellular functions that are difficult to determine in complex multi-organ disorders. Thus, a systemic approach is required to tease apart individual components of complex developmental disorders in affected cell types and tissues.

Regulation of transcription at the level of chromatin is critical during the developmental time frame. Chromatin structure is primarily regulated through post-translational modifications of histones and DNA<sup>8</sup>. Lysine acetylation is particularly widespread among chromatin modifications and promotes active gene transcription<sup>9,10</sup>. Lysine acetylation is catalysed by a conserved family of enzymes, the lysine acetyltransferases (KATs), and removed by lysine deacetylases (HDACs, KDACs)<sup>11,12</sup>. Research over the past decade has firmly established KATs as key mediators of embryonic development. Haploinsufficiency in KATs, including *EP300*, *CBP*, *KAT6A* and *KAT6B*, leads to human developmental syndromes that affect multiple organs and are typified by intellectual disability<sup>13–19</sup>. In addition, mouse models lacking the KATs *Mof* (also known as *Kat8*), *p300*, *Cbp*, *Kat6a*, *Kat6b*, *Gcn5*, *Tip60* or *Hbo1* display prenatal or perinatal lethality<sup>11,20</sup>. While KATs have generally been thought of as global regulators of transcription, it is becoming increasingly clear that they are likely to act in a cell-type- and context-specific manner<sup>21</sup>, encouraging the systematic investigation of their function.

<sup>1</sup>Max Planck Institute of Immunobiology and Epigenetics, Freiburg, Germany. <sup>2</sup>Faculty of Biology, Albert Ludwig University of Freiburg, Freiburg, Germany.

<sup>3</sup>Institute of Neuropathology, Medical Faculty, University of Freiburg, Freiburg, Germany. <sup>4</sup>Institute of Experimental and Clinical Pharmacology and Toxicology, University of Freiburg, Freiburg, Germany. <sup>5</sup>III. Department of Medicine, University Medical Center Hamburg-Eppendorf, Hamburg, Germany.

<sup>6</sup>Department of Neuroanatomy, Institute of Anatomy and Cell Biology, Faculty of Medicine, University of Freiburg, Freiburg, Germany. <sup>7</sup>Medical Physics, Department of Radiology, Faculty of Medicine, University of Freiburg, Freiburg, Germany. <sup>8</sup>German Consortium for Translational Cancer Research (DKTK), Heidelberg, Germany. <sup>9</sup>German Cancer Research Center (DKFZ), Heidelberg, Germany. <sup>10</sup>Max Planck Institute for Molecular Biomedicine, Münster, Germany. <sup>11</sup>Inserm UMR 1231 GAD, Genetics of Developmental disorders and Centre de Référence Maladies Rares Anomalies du Développement et syndromes malformatifs FHU TRANSLAD, Université de Bourgogne-Franche Comté, Dijon, France. <sup>12</sup>CNRS UMR 5309, INSERM, U1209, Institute of Advanced Biosciences, Université Grenoble-Alpes CHU Grenoble, Grenoble, France. <sup>13</sup>UF de foetopathologie, Service de génétique et procréation, CHU Grenoble-Alpes, Grenoble, France. <sup>14</sup>Signaling Research Centers BIOS and CIBS, University of Freiburg, Freiburg, Germany. <sup>15</sup>Center for Basics in NeuroModulation (NeuroModulBasics), Faculty of Medicine, University of Freiburg, Freiburg, Germany. ✉e-mail: [akhtar@ie-freiburg.mpg.de](mailto:akhtar@ie-freiburg.mpg.de)

Among KATs, MOF is particularly interesting for its ability to globally acetylate histone 4 lysine 16 (H4K16) and maintain chromatin in a relaxed and transcriptionally active conformation<sup>22–25</sup>. The addition of H4K16ac alone is sufficient to relax chromatin structure<sup>26</sup>. The importance of MOF extends to embryonic development. Mutations in members of the MOF-containing non-specific lethal (NSL) complex, *KANSL1* and *KANSL2*, result in human developmental syndromes that affect multiple organs and are typified by intellectual disability<sup>27–30</sup>. Mutations in *KANSL1*, which underlie the Koolen-de Vries syndrome (KdV), are relatively common and thought to occur in 1:16,000 live births<sup>31</sup>. Although KdV has been well described clinically<sup>32–34</sup>, the underlying molecular mechanisms leading to defective neurodevelopment, brain function and disease remain to be characterized.

In this study we set out to investigate the neural-specific role of the NSL complex. Using the neural-specific *Nestin-Cre* (*Nes-Cre*), we uncovered that a loss of *Mof*, *Kansl2* or *Kansl3* in neural cells results in inflammation and dysfunction of neighbouring brain vascular cells, leading to haemorrhaging. Through systematic fluorescence-activated-cell-sorting (FACS) isolation and molecular analyses of neural and vascular cells, we found that the NSL complex acts at the level of chromatin to regulate metabolic networks in the neural cell population. The loss of MOF catalytic activity in neural cells led to widespread metabolic changes including a significant accumulation of free long-chain fatty acids (LCFAs). LCFAs directly induced a Toll-like receptor 4 (TLR4)–NF $\kappa$ B-dependent inflammatory response in neighbouring pericytes, which was sufficient to elicit morphological changes. The LCFA-driven inflammatory response could be mitigated in pericytes through the administration of TLR4 inhibitors. Our work establishes that the neural metabolic environment is directly sensed by pericytes and triggers altered vascular function.

## Results

### NSL complex depletion in neural cells causes haemorrhaging.

We conditionally deleted the *Mof*, *Kansl2* and *Kansl3* genes using the neural-specific *Nes-Cre* to investigate the role of MOF and the NSL complex in neural development and function (Extended Data Fig. 1a). We were unable to recover any viable *Mof*<sup>fl/fl</sup> *Nes-Cre*<sup>fl/+</sup> (denoted *Mof*-nKO), *Kansl2*<sup>fl/fl</sup> *Nes-Cre*<sup>fl/+</sup> (*Kansl2*-nKO) or *Kansl3*<sup>fl/fl</sup> *Nes-Cre*<sup>fl/+</sup> (*Kansl3*-nKO) animals after birth, suggesting perinatal lethality. Consistent with this, detailed analysis of *Mof*-nKO mutants showed their presence at normal Mendelian frequencies during embryogenesis but not after birth (Extended Data Fig. 1b–h).

To determine the cause of death in the *Mof*-nKO, *Kansl2*-nKO and *Kansl3*-nKO embryos, we undertook detailed morphological and histological analyses during the embryonic stages. We observed signs of haemorrhaging in 100% of *Mof*-nKO, *Kansl2*-nKO and *Kansl3*-nKO brains by midday on embryonic day 14 (E14.5;  $n > 50$  embryos per genotype; Fig. 1a–h). The haemorrhaging was particularly severe in E14.5 *Kansl2*-nKO and *Kansl3*-nKO embryos, which displayed extensive intraventricular bleeding (Fig. 1e–h). In contrast, the phenotype was less severe in *Mof*-nKO embryos, which showed localized haematomas in the brain parenchyma (Fig. 1c,d,j). These observations were consistent with the NSL complex hierarchy, whereby depletion of either *KANSL2* or *KANSL3*, but not MOF, results in complex destabilization<sup>35</sup> (Extended Data Fig. 1e–h).

The haemorrhaging was most severe in the region of the ganglionic eminence (Fig. 1i–l), an area containing particularly immature vasculature that is highly prone to haemorrhaging during development<sup>36,37</sup>. There was disruption of the ganglionic eminence in all *Mof*-nKO, *Kansl2*-nKO and *Kansl3*-nKO embryos that were histologically analysed (Fig. 1i–l). We quantified the severity of the haemorrhaging by analysing the number of Ter-119<sup>+</sup>CD11b<sup>+</sup> red blood cells in the brain parenchyma and detected an increase in

the *Kansl2*-nKO and *Kansl3*-nKO brains (Fig. 1m). Together, these analyses suggest that depletion of NSL-complex members leads to haemorrhaging, which is evident from E14.5 onwards.

We observed an expansion in the ventricular size in the histological analyses (Fig. 1l), a phenotype that has also been reported in human patients with KdV<sup>33</sup>. Thus, we quantified the ventricular volume from magnetic-resonance-imaging (MRI) scans of *Mof*-nKO, *Kansl2*-nKO and *Kansl3*-nKO embryos at E14. All three knockouts exhibited a marked expansion of the lateral ventricle (Fig. 1n).

We next determined whether further neural developmental abnormalities were evident following neural depletion of NSL complex members. Given the strong concordance of gene expression changes in *Mof*-nKO, *Kansl2*-nKO and *Kansl3*-nKO brains at E14.5 (Fig. 1o) and that the MOF–NSL subunits also form a molecular complex in the E14.5 brain (Extended Data Fig. 1i), we focused on the *Mof*-nKO model as it depletes the enzymatic component of the NSL complex. Consistent with the disorganization and haemorrhaging in the ganglionic eminence, we observed extensive cell death in this region in *Mof*-nKO brains (Extended Data Fig. 2b). In contrast, no significant cell death was evident in the developing *Mof*-nKO cortex at E14.5 (Extended Data Fig. 2c). The *Mof*-nKO cortex showed normal layering at E14.5 but was severely disorganized at E16.5 (Extended Data Fig. 2c,d). Furthermore, the integrity of the ependymal layer, structure of the choroid plexus as well as cell proliferation in the stem cell niche adjacent to the lateral ventricle were normal in *Mof*-nKO brains at E14.5 (Extended Data Fig. 2e–g). Together, these analyses revealed that the most striking phenotype following depletion of members of the NSL complex from the E14.5 brain was haemorrhaging.

***Nes-Cre* is specifically active in neural cells.** Haemorrhaging in the NSL-complex-nKO animals signalled the presence of vascular defects. We therefore wanted to confirm that the *Nes-Cre* was indeed neural specific. We isolated neural cells, microglia, and vascular mural and endothelial cells from *Mof*-nKO brains using the FACS-based EMBRACE methodology<sup>38</sup> and analysed the levels of *Mof* mRNA (Extended Data Fig. 3a). Mural cells control the permeability and stability of blood vessels, and are a combination of pericytes that are present on capillaries as well as the closely related smooth muscle cells that are found on larger blood vessels. Isolation of mural cells via EMBRACE yields about 96% pericytes ( $n = 340$  of 354) and approximately 4% smooth muscle cells ( $n = 14$  of 354) from the E14.5 brain and thus, we refer to this cell population as pericytes from here on. Consistent with the expected neural-specific expression of the *Nes-Cre*, we measured a depletion of *Mof* mRNA of approximately 90% in the *Mof*-nKO neural population (Fig. 2a). In contrast, pericytes, endothelial cells and microglia isolated from the same *Mof*-nKO brains did not show a reduction in *Mof* mRNA (Fig. 2a), suggesting that the *Nes-Cre* is indeed not active in these cell types. In addition, using *Cre*-reporter mice, we detected high levels of *Nes-Cre* activity in neural cells but not in populations enriched for pericytes, endothelial cells or microglia (Extended Data Fig. 3b–d). Together, these analyses confirm that the *Nes-Cre* is indeed neural specific at E14.5 and the vascular defects underlying haemorrhaging in *Mof*-nKO, *Kansl2*-nKO and *Kansl3*-nKO animals are indirect and caused by the lack of NSL complex activity in neural cells.

### Neural NSL-complex depletion causes distinct molecular defects in neural and vascular cells.

To systematically determine the cell-type-specific changes underlying the haemorrhaging phenotype, we isolated neural cells, pericytes, endothelial cells and microglia from E14.5 brains using EMBRACE<sup>38</sup> and performed transcriptomic analyses. As expected, RNA sequencing (RNA-seq) tracks showed a loss of *Mof* mRNA in *Mof*-nKO neural cells, whereas

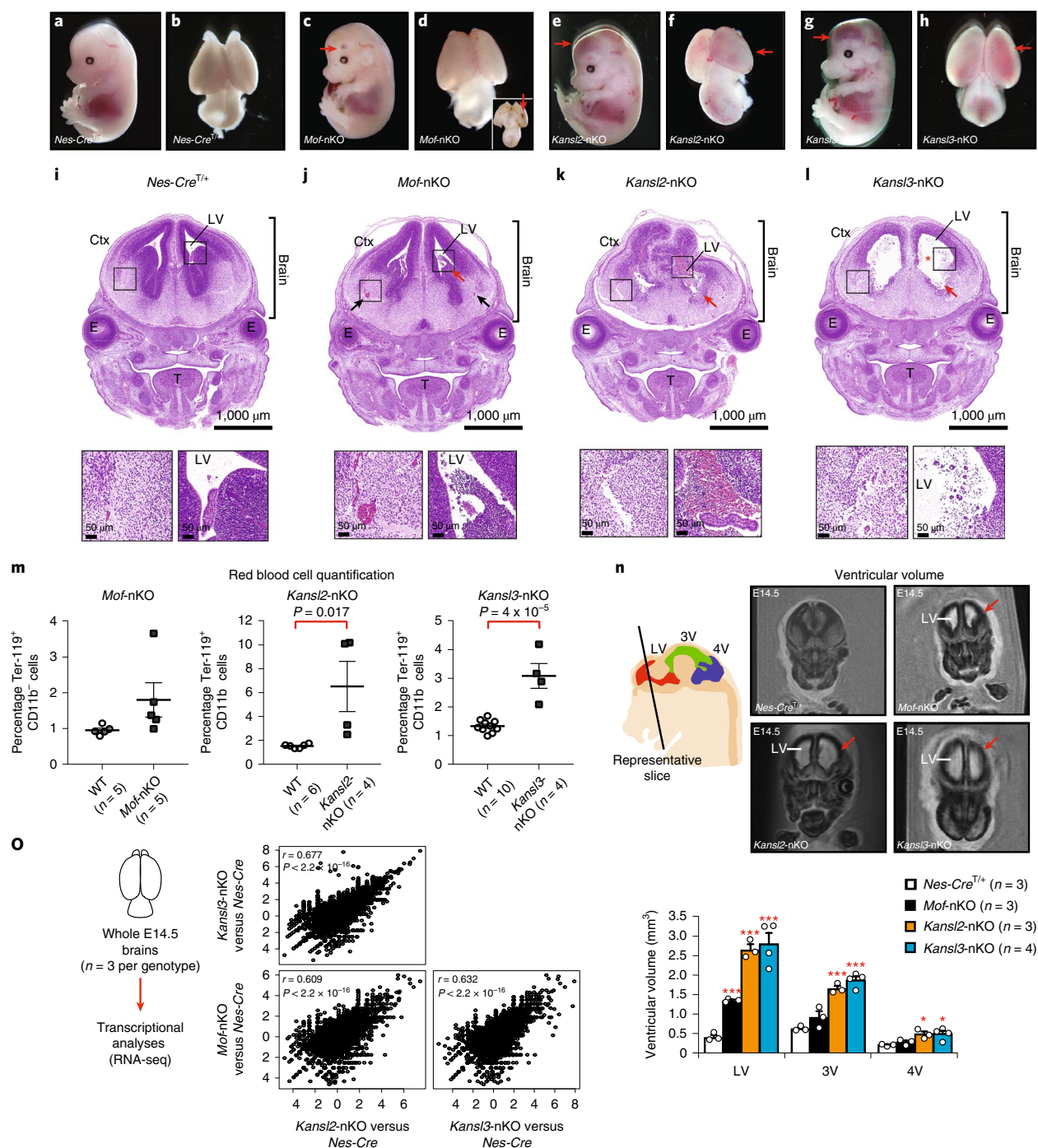


**Fig. 1 | NSL complex deletion causes haemorrhaging in the developing brain.** **a–h**, Representative images of *Nes-Cre*<sup>T/+</sup> (**a**), *Mof*-nKO (**c**), *Kansl2*-nKO (**e**) and *Kansl3*-nKO (**g**) embryos at E14.5 as well as brains extracted from *Nes-Cre*<sup>T/+</sup> (**b**), *Mof*-nKO (**d**), *Kansl2*-nKO (**f**) and *Kansl3*-nKO (**h**) embryos. The nKO embryos showed signs of haemorrhaging by midday on E14.5 (red arrows; 56–91 embryos analysed per genotype). *Kansl2*-nKO and *Kansl3*-nKO embryos displayed a more severe phenotype with intraventricular bleeding, whereas *Mof*-nKO embryos typically showed localized bleeding that was generally best observed from the ventral side (**d**, inset). **i–l**, Representative histological sections with haematoxylin-and-eosin staining of *Nes-Cre*<sup>T/+</sup> (**i**), *Mof*-nKO (**j**), *Kansl2*-nKO (**k**) and *Kansl3*-nKO (**l**) embryos at E14.5. Disruption of the ganglionic eminence was observed in all nKO brains (red arrows). Haematomas are evident in the *Mof*-nKO section (**j**, black arrows), whereas the *Kansl2*-nKO section shows intraventricular haemorrhaging (**k**, inset). Three animals were analysed per genotype. Magnified views of the areas in the black boxes are shown (bottom). Ctx, cortex; E, eye; LV, lateral ventricle; T, tongue. **m**, FACS quantification of red blood cells (Ter-119<sup>+</sup>CD11b<sup>-</sup>) in the brains of *Mof*-nKO, *Kansl2*-nKO and *Kansl3*-nKO mice as well as their WT littermates at E14.5. The red arrows mark dilated lateral ventricles. **n**, MRI imaging (top) and quantification (bottom) of the ventricular size of the brains of *Nes-Cre*<sup>T/+</sup>, *Mof*-nKO, *Kansl2*-nKO and *Kansl3*-nKO embryos at E14.5. LV, lateral ventricle; 3V, third ventricle; 4V, fourth ventricle; \**P* < 0.05 and \*\*\**P* < 0.001. The precise *P* values are provided in Source Data Fig. 1. **m, n**, Data are presented as the mean ± s.e.m. and were analysed using a two-tailed Student's *t*-test; *n*, number of animals examined. **o**, Correlation between gene expression changes in the brains of *Mof*-nKO, *Kansl2*-nKO and *Kansl3*-nKO embryos. Each data point represents the expression of a single gene averaged across the three replicates (animals). Gene expression changes in the presented comparisons were used to calculate the Pearson's coefficient (*r*). Statistical source data are provided.

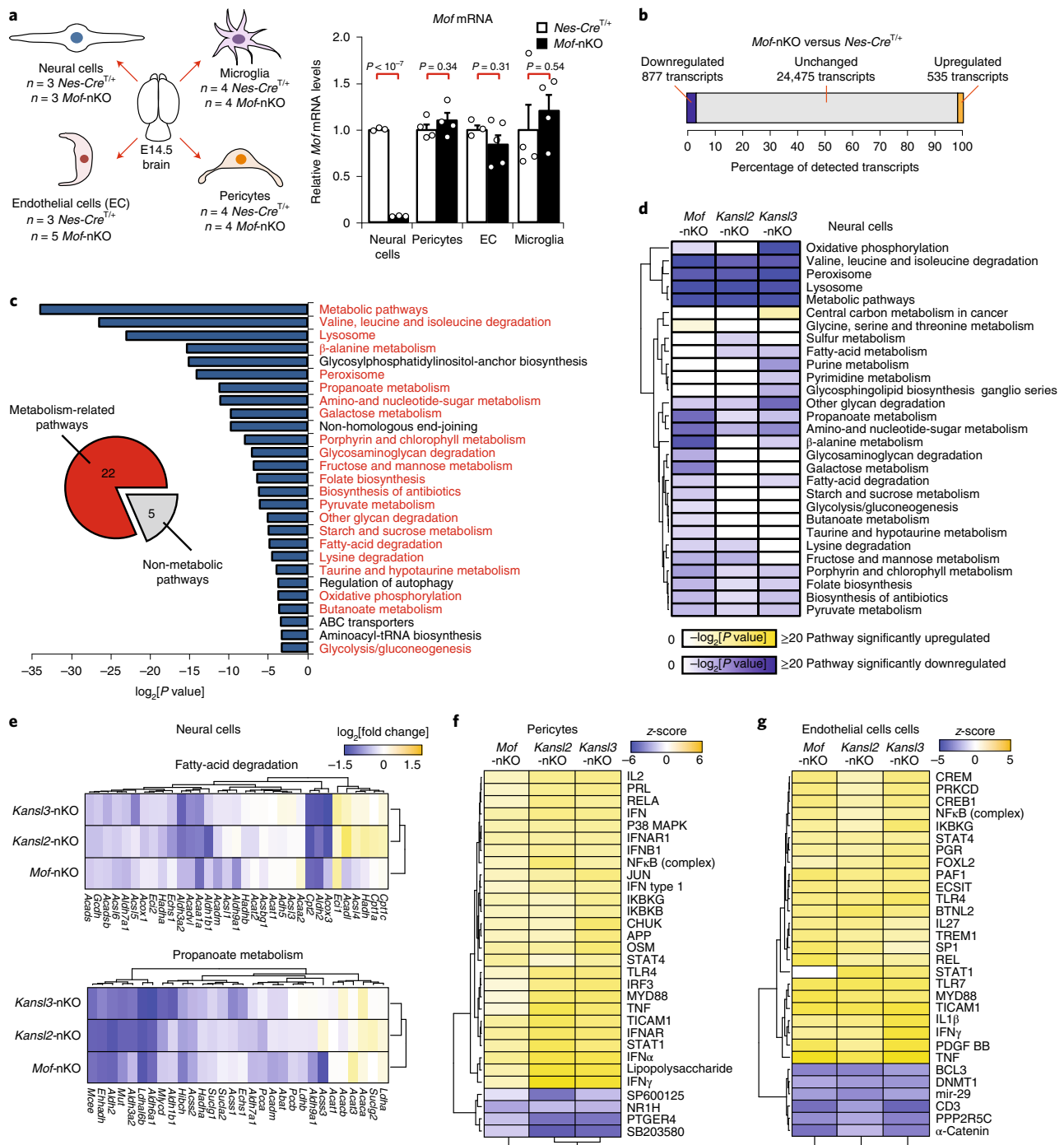


**Fig. 2 | Neural depletion of the NSL complex disrupts neural metabolic networks and causes vascular inflammation.** **a**, The EMBRACE technique<sup>38</sup> was used to isolate neural cells (PDGFR $\beta$ -CD45-CD41-CD11b-PECAM1-CD102<sup>-</sup>), pericytes (PDGFR $\beta$ <sup>high</sup>CD45-CD41-CD11b-PECAM1-CD102<sup>-</sup>), endothelial cells (PECAM1<sup>+</sup>CD102<sup>+</sup>CD45-CD41<sup>-</sup>) and microglia (CD11b<sup>+</sup>CD45<sup>medium</sup>PECAM1-PDGFR $\beta$ <sup>-</sup>) from *Mof*-nKO and *Nes-Cre*<sup>T/+</sup> brains (left). The levels of *Mof* mRNA were quantified using quantitative reverse-transcription PCR (right). Data are presented as the mean  $\pm$  s.e.m. and were analysed using a two-tailed Student's *t*-test; *n*, number of animals examined. **b**, Number of differentially expressed genes in *Mof*-nKO versus *Nes-Cre*<sup>T/+</sup> neural cells (false discovery rate (FDR) < 0.05,  $\log_2[\text{fold change}] > |0.5|$ ). **c**, List of Kyoto Encyclopedia of Genes and Genomes (KEGG) pathways significantly enriched among genes downregulated in *Mof*-nKO neural cells. Of the 27 significantly enriched pathways, 22 were related to metabolism (red). **d**, Comparison of changes in KEGG metabolic pathways in *Mof*-nKO, *Kansl2*-nKO and *Kansl3*-nKO neural cells. All metabolism-associated pathways significantly up- or downregulated in one or more of the *Mof*-nKO, *Kansl2*-nKO or *Kansl3*-nKO neural datasets have been included in this list. **c,d**, Data were analysed using a Fisher's exact test. **e**, Heatmaps showing reduced expression of genes in the KEGG fatty-acid-degradation and propanoate-metabolism pathways in *Mof*-nKO, *Kansl2*-nKO and *Kansl3*-nKO neural cells. **b-e**, Three animals were analysed per genotype. **f**, Top activated and repressed molecular networks in pericytes isolated from *Mof*-nKO, *Kansl2*-nKO and *Kansl3*-nKO brains. Networks were identified using Ingenuity network analysis. Data were collected from  $n = 4$  (*Nes-Cre*<sup>T/+</sup> and *Kansl3*-nKO) and 3 (*Mof*-nKO and *Kansl2*-nKO) animals. **g**, Top activated and repressed molecular networks in endothelial cells isolated from nKO brains. Data were collected from  $n = 4$  (*Nes-Cre*<sup>T/+</sup> and *Mof*-nKO) and 3 (*Kansl2*-nKO and *Kansl3*-nKO) animals. **f,g**, The top 30 networks (ranked on the absolute z-score) are shown. Statistical source data are provided.

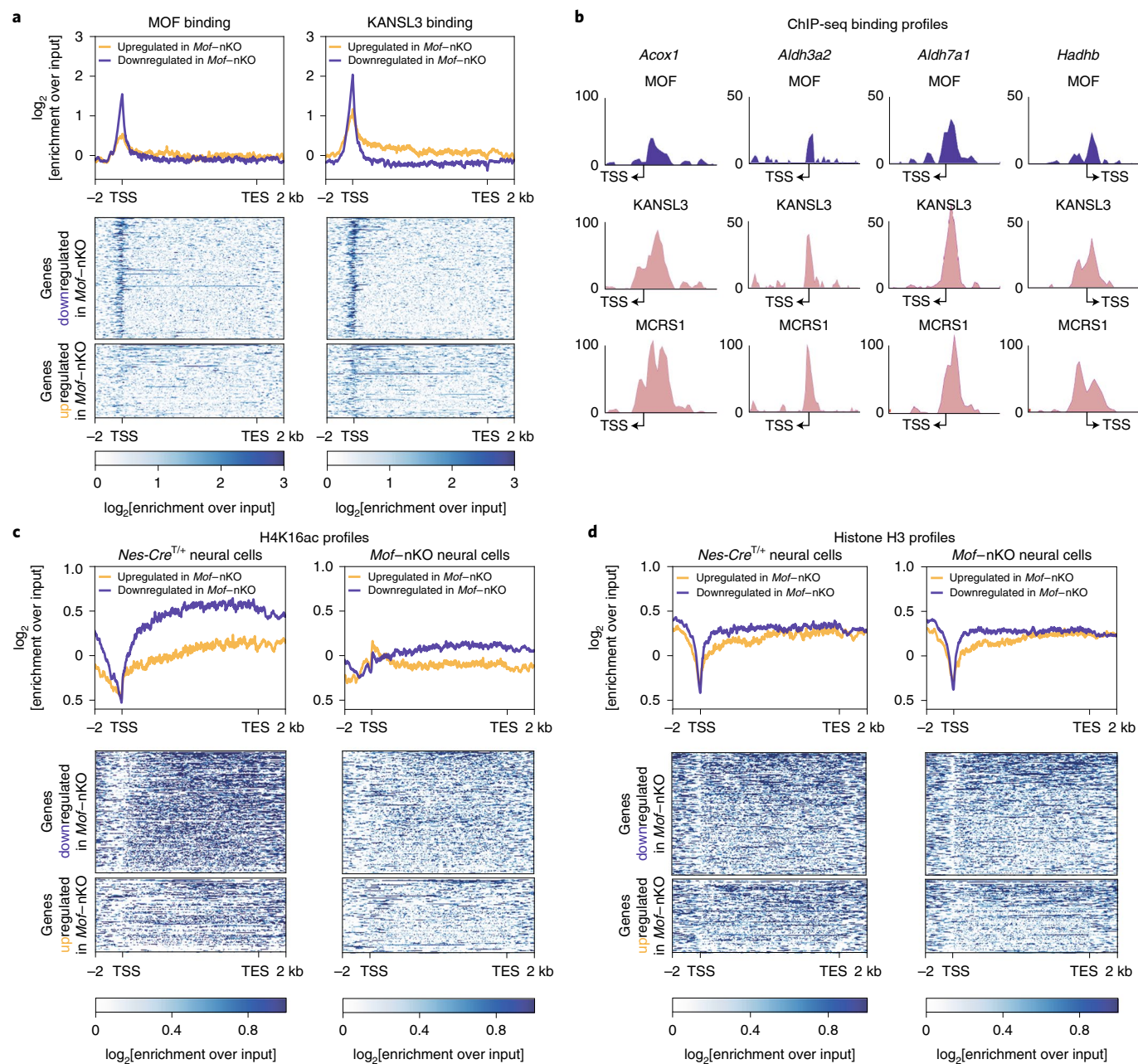


**Fig. 3 | MOF regulates metabolic gene expression via H4K16ac.** **a**, MOF (left) and KANSL3 (right) strongly bind to the TSS of genes significantly downregulated in *Mof*-nKO neural cells. The list of differentially expressed genes in *Mof*-nKO neural cells was compared with the MOF and KANSL3 ChIP-seq profiles<sup>25</sup>. Enrichment values are provided on a  $\log_2$  scale and were calculated after standardizing all data to the input. The genes that were downregulated in *Mof*-nKO neural cells showed stronger binding of MOF and KANSL3 compared with upregulated genes ( $P < 2.2 \times 10^{-16}$ ; two-sided Wilcoxon rank-sum test). Three animals were subjected to RNA-seq analyses per genotype. **b**, Representative Integrative Genomics Viewer (IGV) outputs showing enrichment of the NSL complex members MOF, KANSL3 and MCERS1 at the TSS of the metabolic genes *Acox1*, *Aldh3a2*, *Aldh7a1* and *Hadhb*. MCERS1 is found in both the NSL and INO80 complexes<sup>30</sup>. **c**, H4K16ac ChIP-seq profiles in control *Nes-Cre*<sup>T/+</sup> (left) and *Mof*-nKO (right) neural cells. The H4K16ac levels were standardized to the input and compared between genes that were transcriptionally down- or upregulated in *Mof*-nKO neural cells. Note the loss of H4K16ac in *Mof*-nKO neural cells (right) compared with *Nes-Cre*<sup>T/+</sup> controls (left;  $P < 10^{-10}$ ; two-sided Wilcoxon rank-sum test). **d**, Histone H3 profiles in control *Nes-Cre*<sup>T/+</sup> (left) and *Mof*-nKO (right) neural cells. Histone H3 levels were unchanged across genes that were up- or downregulated in *Mof*-nKO neural cells. The levels of histone H3 were standardized to the input before visualization. **c,d**,  $n = 3$  *Mof*-nKO and 2 (WT littermate and *Nes-Cre*<sup>T/+</sup> control) embryos. TES, transcription end site. TSS, transcription start site.

*Mof* levels were normal in pericytes, and endothelial and microglial cells (Extended Data Fig. 4a,b).

Neural cells isolated from *Mof*-nKO brains displayed 1,412 differentially expressed genes (Fig. 2b). We focused on downregulated genes, as they were most likely to be direct targets of the

transcriptional activator MOF. Interestingly, 22 of the 27 pathways significantly enriched among the downregulated genes were related to metabolism (Fig. 2c). In contrast, the upregulated genes were enriched for pathways involved in stress response (Extended Data Fig. 4c). Moreover, the downregulation of metabolic pathways

was shared among neural cells lacking MOF, KANSL2 or KANSL3 (Fig. 2d,e and Extended Data Fig. 4d,e). These transcriptomic analyses revealed that depletion of the NSL complex results in reduced transcription of global metabolic networks.

We next investigated which molecular networks were deregulated in vascular pericytes and endothelial cells. In contrast to neural cells, pericytes and endothelial cells showed strong activation of inflammatory gene networks (Fig. 2f,g). In particular, the TLR–NF $\kappa$ B and the STAT signalling pathways were strongly activated. Together, these analyses suggest that depletion of the NSL complex leads to a deregulated neural metabolic environment, which in turn induces an inflammatory response in vascular cells.

**MOF directly regulates metabolic gene networks.** We investigated whether the deregulation of neural metabolic networks was a direct consequence of MOF–NSL depletion. We compared MOF and KANSL3 chromatin immunoprecipitation–sequencing (ChIP–seq) profiles<sup>25</sup> with transcriptional data from *Mof*-nKO neural cells. MOF and KANSL3 directly bound to the transcriptional start site (TSS) of genes that were downregulated following *Mof* depletion (Fig. 3a,b;  $P < 2.2 \times 10^{-16}$ ). We next analysed levels of the MOF target modification, H4K16ac. Genes downregulated in *Mof*-nKO neural cells displayed a concomitant loss of H4K16ac relative to *Nes-Cre*<sup>fl/+</sup> controls (Fig. 3c;  $P < 10^{-10}$ ). In contrast, histone H3 levels did not show strong changes in *Mof*-nKO neural cells (Fig. 3d). Together, these findings establish that MOF directly regulates the expression of metabolic transcriptional networks in neural cells via H4K16ac.

**MOF depletion disrupts the neural metabolic environment.** Given that MOF directly maintains metabolic gene networks, we hypothesized that MOF depletion will induce a deregulated metabolic environment. We utilized two complementary strategies to screen for metabolic changes in *Mof*-deficient neural cells. First, Seahorse assays revealed that both basal and ATP-linked respiration were significantly compromised in *Mof*-nKO cells (Extended Data Fig. 5a–d). Second, we adopted an unbiased mass spectrometry (MS)-based metabolomics approach to globally chart the neural metabolic environment. As the brain is a highly complex environment undergoing constant modulation through blood flow and cerebrospinal fluid, we established neurosphere cultures, which consist of neural stem cells, progenitors and differentiating cells, from *Mof*-floxed animals at E14.5 harbouring the tamoxifen-inducible *Caag-Cre-ERT2*. *Mof*-KO neurospheres showed broad changes in their metabolite profile (Fig. 4a and Extended Data Fig. 5e). When ranked according to the *P* values, the most striking change in *Mof*-KO cultures was the accumulation of the LCFAs palmitic acid and stearic acid as well as glycerol phosphate (Fig. 4b–d). This was particularly interesting, as these metabolites form the precursors for more complex lipids. In contrast, the abundances of a number of central cellular metabolites

such as pyruvic acid were not significantly altered in *Mof*-KO neurospheres (Fig. 4e).

Given the significant changes in lipid precursors in *Mof*-KO neurospheres, we undertook MS-based lipidomics. We observed a significant shift in the overall lipid profile of *Mof*-KO neurospheres (Fig. 4f, principal component analysis), with a significant accumulation of the LCFAs C20:0 (arachidic acid), C16:0 (palmitic acid) and C18:0 (stearic acid) (Fig. 4f). In contrast, there was a reduction in more complex lipid species in *Mof*-KO neurospheres. We confirmed the accumulation of LCFAs in *Mof*-KO neurospheres using a gas chromatography–MS (GC–MS)-based method<sup>39</sup> that specifically measures free LCFAs (Fig. 4g). We next tested whether MOF was also responsible for maintaining LCFA levels in an independent cell type. We established primary mouse embryonic fibroblast (MEFs) from *Mof*-floxed animals crossed to the *Caag-Cre-ERT2*. *Mof*-KO MEFs showed increased accumulation of LCFAs, which could be rescued by re-expressing wild-type (WT) MOF but not the catalytically dead E350Q MOF (Extended Data Fig. 5f–l). These analyses suggest that MOF catalytic activity is required to maintain normal cellular levels of LCFAs.

Together, our battery of MS-based metabolomics assays revealed a consistent and striking accumulation of free LCFAs in *Mof*-deficient neural cells.

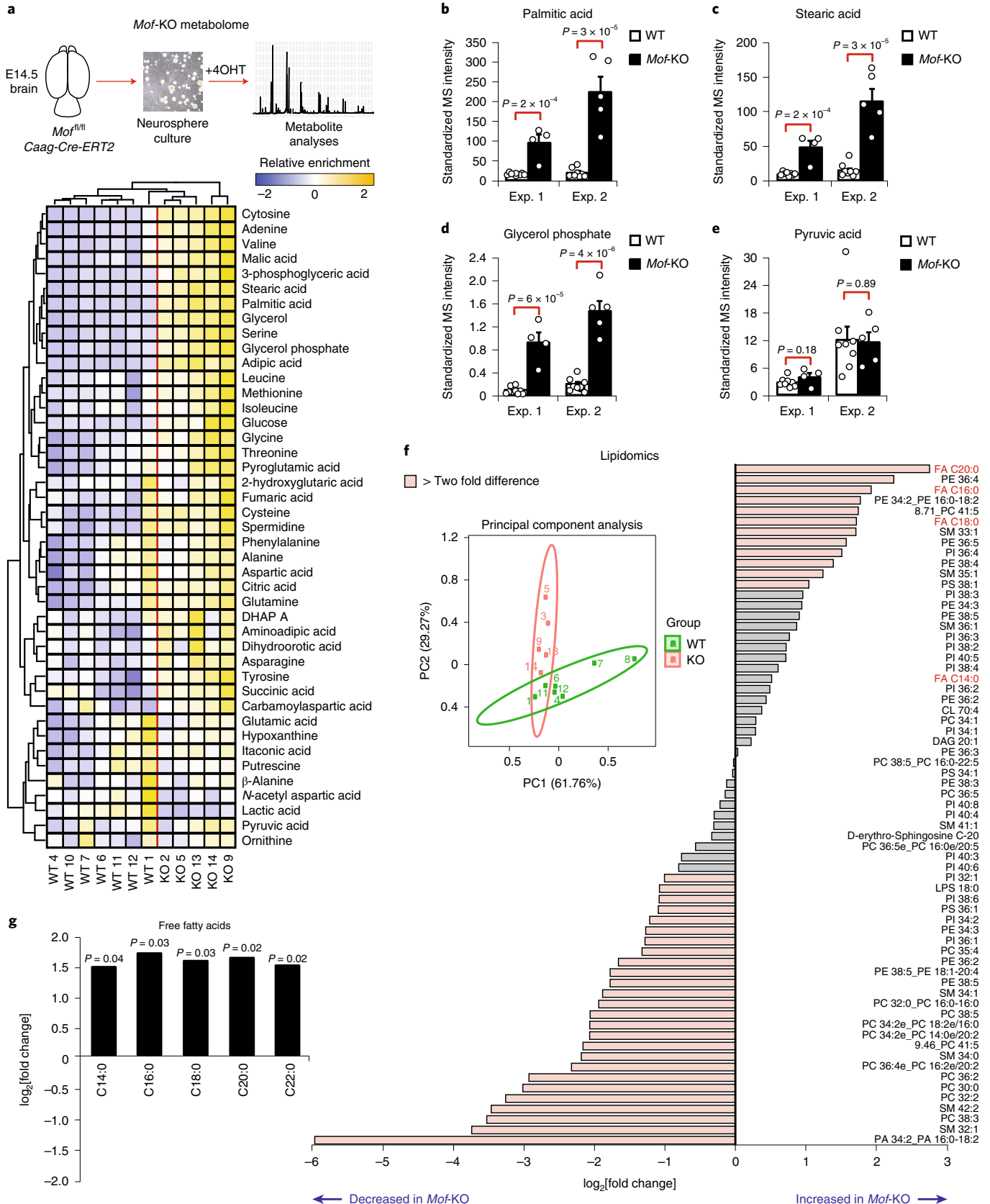
**LCFAs induce an NF $\kappa$ B-driven pro-inflammatory response in brain pericytes.** The accumulation of free LCFAs in *Mof*-deficient neural cells coupled with the strong activation of the TLR–MYD88–NF $\kappa$ B pathway in *Mof*-nKO, *Kansl2*-nKO and *Kansl3*-nKO vascular cells (Fig. 5a) led us to speculate that LCFAs trigger NF $\kappa$ B activation in brain vascular cells. Consistent with our hypothesis, treatment of primary brain pericytes with LCFAs showed strong activation of NF $\kappa$ B, as evidenced by an increased nuclear accumulation of NF $\kappa$ B as well as S536 phosphorylation of the NF $\kappa$ B RelA subunit (Fig. 5b,c and Extended Data Fig. 6a). Interestingly, this response was specific to pericytes and not observed in brain endothelial cells (Fig. 5d,e). We next compared the activation of global gene networks in LCFA-treated pericytes against pericytes isolated from *Mof*-nKO, *Kansl2*-nKO and *Kansl3*-nKO brains. Comparison of the RNA-seq datasets revealed a strong inflammatory signature including activation of the TLR–MYD88–NF $\kappa$ B signalling axis under both conditions (Fig. 5f). This supports our hypothesis that LCFA accumulation is a major cause of the inflammatory response elicited in *Mof*-nKO, *Kansl2*-nKO and *Kansl3*-nKO pericytes.

**LCFA treatment or depletion of neural MOF results in breakdown of the microvasculature.** We next determined the consequences of LCFA-induced pericyte activation. Using electric cell-substrate impedance sensing (ECIS) measurements, we found that LCFA treatment led to the loss of impedance in brain pericytes

**Fig. 4 | MOF deficiency leads to an altered neural metabolic environment.** **a**, Neurosphere cultures were established from *Mof*<sup>fl/fl</sup>; *Caag-Cre-ERT2*<sup>+/+</sup> (*Mof*-KO) and *Mof*<sup>fl/fl</sup> (WT) brains at E14.5 and treated with tamoxifen (4OHT) to induce *Mof* deletion. Metabolites were extracted and quantified by GC–MS. The average of two independent experiments is presented in the heatmap. Relative enrichment was calculated using the formula  $(MI - \text{average}(MI)) \div \text{s.d.}$ , where MI is the MS intensity of the metabolite and  $\text{average}(MI)$  refers to the average MS intensity of a given metabolite across all measured samples. s.d., standard deviation. Data were analysed using a two-tailed Student's *t*-test. **b–d**, Quantification of the three most significantly changed metabolites (ranked by the *P* value) detected via GC–MS in *Mof*-KO neurospheres. Data from the two independent experiments are shown separately. **e**, Quantification of pyruvic acid (acid form of pyruvate) extracted from *Mof*-KO versus WT neurosphere cultures. **a–e**, Replicates (independent neurosphere cell lines, each generated from one embryo and independently measured by MS): Exp. 1,  $n = 4$  *Mof*-KO and 8 WT; and Exp. 2,  $n = 5$  *Mof*-KO and 8 WT. **b–e**, Data are presented as the mean  $\pm$  s.e.m. and were analysed using a two-tailed Student's *t*-test. **f**, Quantification of lipid species in *Mof*-KO versus WT neurospheres via liquid chromatography coupled to a quadrupole time-of-flight (LC–QTOF) MS. Negative values on the *x* axis represent lipid species that are reduced in *Mof*-KO cells and positive values indicate lipid species that accumulate in *Mof*-KO neurospheres. The inset depicts principal component analysis (PCA) showing relative changes in the overall lipid profiles of each *Mof*-KO and WT neurosphere cell line;  $n = 5$  *Mof*-KO and 8 WT independent neurosphere cell lines. **g**, Quantification of free LCFAs in *Mof*-KO versus WT neurospheres via GC–MS. Data were analysed using a two-tailed Student's *t*-test;  $n = 3$  *Mof*-KO and 5 WT independent neurosphere cell lines. **a–g**, Data were standardized to the total cell number (protein concentration). Each neurosphere cell line analysed was generated from one embryo. **a–e,g**, Data were additionally standardized to spike-in controls. Statistical source data are provided.

but not endothelial cells (Fig. 6a), indicating an abrupt change in their morphology. Given that pericytes tightly regulate the permeability of neural vasculature, the ECIS experiments led us to hypothesize that pericyte function may be impaired in *Mof*-nKO brains.

To test our hypothesis, we undertook detailed analyses of the neural vasculature in *Mof*-nKO brains using transmission electron microscopy. We observed widespread and severe defects in the microvasculature, concomitant with prominent changes in pericyte



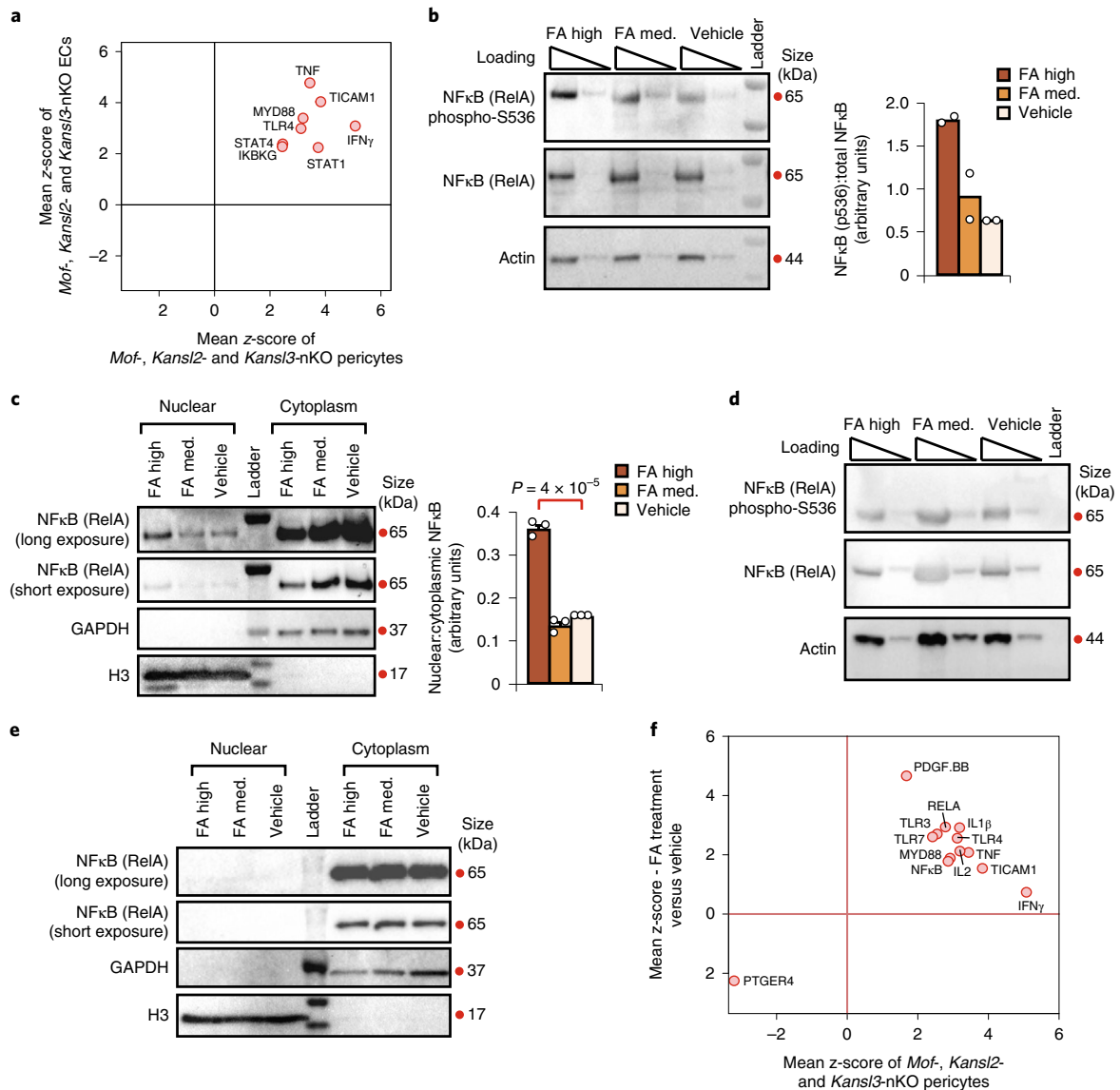


**Fig. 5 | LCFAs activate NF $\kappa$ B in brain pericytes.** **a**, Gene regulatory networks activated and repressed in both pericytes and endothelial cells (ECs) isolated from nKO brains. Regulatory networks found in the 30 most significantly deregulated networks in both pericytes and ECs were included. Data are derived from  $n = 4$  (*Nes-Cre*<sup>+/+</sup> and *Kansl3*-nKO) and 3 (*Mof*-nKO and *Kansl2*-nKO) animals for pericytes; and  $n = 4$  (*Nes-Cre*<sup>+/+</sup> and *Mof*-nKO) and 3 (*Kansl2*-nKO and *Kansl3*-nKO) animals for EC. **b**, Levels of S536-phosphorylated NF $\kappa$ B (RelA, p65 subunit) in primary brain pericytes treated with LCFAs. The S536-phosphorylated NF $\kappa$ B levels were standardized to the total NF $\kappa$ B levels. Quantification of NF $\kappa$ B (p536):total NF $\kappa$ B (right). Data are presented as the mean of two independent experiments. **c**, Localization of NF $\kappa$ B (RelA, p65 subunit) in the cytoplasm versus nucleus of primary brain pericytes following LCFA treatment (left). Quantification of nuclear:cytoplasmic NF $\kappa$ B levels (right). The cytoplasmic NF $\kappa$ B levels were standardized to GAPDH and the nuclear NF $\kappa$ B to histone H3. Data are presented as the mean  $\pm$  s.e.m. of  $n = 3$  independent experiments and were analysed using a two-tailed Student's *t*-test. **d**, Levels of S536-phosphorylated NF $\kappa$ B (RelA, p65 subunit) in b.End3 brain ECs after 16 h of LCFA treatment. The experiment was repeated twice with similar results. **e**, Nuclear and cytoplasmic NF $\kappa$ B (RelA, p65 subunit) levels in brain endothelial b.End3 cells in response to LCFA treatment. The experiment was repeated twice with similar results. **f**, Comparison of global changes in regulatory transcriptional networks in primary brain pericytes treated with LCFAs (*y* axis) against pericytes isolated via EMBRACE from the *Mof*-nKO, *Kansl2*-nKO and *Kansl3*-nKO brains (*x* axis). An overlap in the activation of inflammatory networks (for example, TLR-MYD88-NF $\kappa$ B) was observed. *y* axis,  $n = 3$  independent experiments per treatment; *x* axis,  $n = 4$  (*Nes-Cre*<sup>+/+</sup> and *Kansl3*-nKO) and 3 (*Mof*-nKO and *Kansl2*-nKO) animals. FA high refers to a cocktail of 200  $\mu$ M C14:0, 200  $\mu$ M C16:0, 20  $\mu$ M C20:0 and 10  $\mu$ M C24:0. FA med. refers to 50  $\mu$ M C14:0, 50  $\mu$ M C16:0, 5  $\mu$ M C20:0 and 2.5  $\mu$ M C24:0. Protein sizes are indicated in kDa. Statistical source data and unprocessed blots are provided.

morphology (Fig. 6b,c and Extended Data Fig. 6b,c). The microvessels in *Mof*-nKO brains were highly dilated and displayed significant thinning of the extracellular matrix (Fig. 6d,e). In rare cases, the capillaries had completely collapsed and the surrounding area was highly disrupted (Extended Data Fig. 6c, (i) and (ii)). Around 67% of pericytes showed detachment from the blood vessels in *Mof*-nKO

brains, a phenotype rarely observed in *Nes-Cre*<sup>+/+</sup> animals (Fig. 6c). In contrast to the widespread morphological changes in the microvasculature, vessel bifurcation, recruitment of mural cells as well as the total number of endothelial cells and pericytes in *Mof*-nKO brains did not differ from controls (Extended Data Fig. 6d-f). Furthermore, no significant changes in the vascularization of

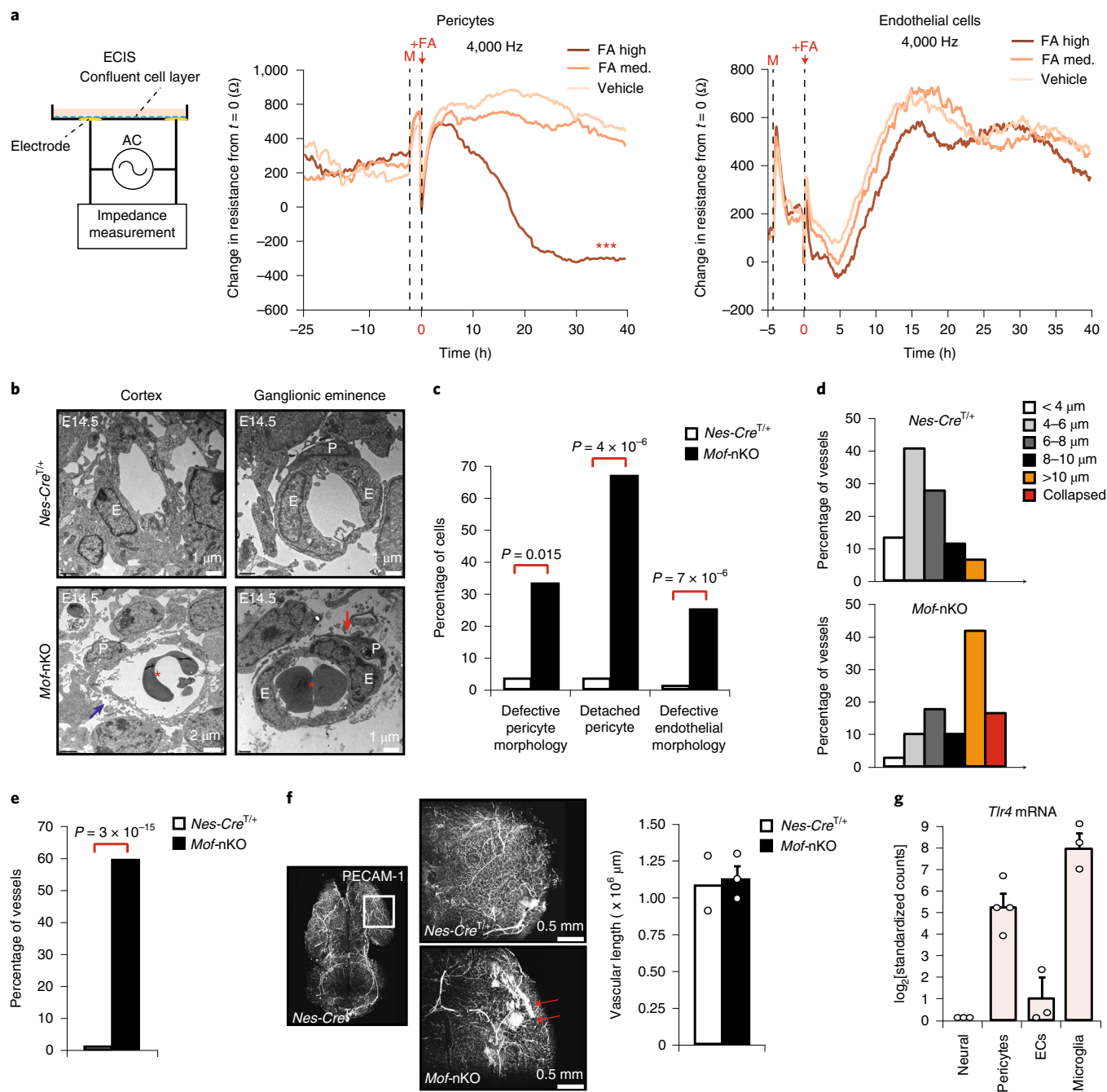


**Fig. 6 | Neural MOF depletion results in the breakdown of neural microvasculature.** **a**, Impedance measurements of primary brain pericytes (middle) and primary dermal endothelial cells (right) in response to LCFAs. Data were analysed using a two-tailed Student's *t*-test. \*\*\* $P < 0.001$ . All treatments were performed in duplicate. The experiment was repeated three times with similar results. M, medium change; +FA, LCFA addition. **b**, Representative electron micrographs of blood vessels in the cortex (left) and ganglionic eminence (right). Capillaries from *Mof-nKO* brains were dilated (red asterisk) and showed gaps in the extracellular matrix (blue arrow). Pericytes were frequently detached or detaching (marked by a red arrow). Further examples are provided in Extended Data Fig. 6b,c. A total of 79 capillaries in 2 *Mof-nKO* brains and 63 capillaries in 2 *Nes-Cre<sup>+/+</sup>* brains were analysed. P, pericytes; E, endothelial cells. **c**, Quantification of morphological defects in endothelial cells and pericytes. Data were analysed using a two-tailed Fisher's exact test;  $n = 90$  (from two *Mof-nKO* brains) and 56 (from two *Nes-Cre<sup>+/+</sup>* brains) endothelial cells;  $n = 30$  (from two *Mof-nKO* brains) and 22 (from two *Nes-Cre<sup>+/+</sup>* brains) pericytes. **d**, Quantification of the capillary diameters in *Mof-nKO* (bottom) and *Nes-Cre<sup>+/+</sup>* controls (top).  $n = 78$  (from two *Mof-nKO* brains) and 61 (from two *Nes-Cre<sup>+/+</sup>* brains) capillaries. **e**, Quantification of capillaries displaying thinning of the vessel-associated extracellular matrix. Data were analysed using a two-tailed Fisher's exact test;  $n = 79$  (from two *Mof-nKO* brains) and 63 (from two *Nes-Cre<sup>+/+</sup>* brains) capillaries. **f**, Representative light-sheet images of the vasculature in whole *Mof-nKO* and *Nes-Cre<sup>+/+</sup>* brains (left). The area in the forebrain in a white box (left-most image) is displayed at higher magnifications for *Mof-nKO* and *Nes-Cre<sup>+/+</sup>* brains. Blood clots (red arrows) were observed in the forebrain of *Mof-nKO* brains. Total brain vasculature (right). Data are presented as the mean  $\pm$  s.e.m. of  $n = 3$  (*Mof-nKO*) and 2 (*Nes-Cre<sup>+/+</sup>*) animals. **g**, Expression levels of *Tlr4* mRNA in pericytes ( $n = 4$  animals), neural cells ( $n = 3$  animals), endothelial cells ( $n = 3$  animals) and microglia ( $n = 3$  animals) isolated from *Nes-Cre<sup>+/+</sup>* brains at E14.5. Data are presented as the mean  $\pm$  s.e.m. Statistical source data are provided.

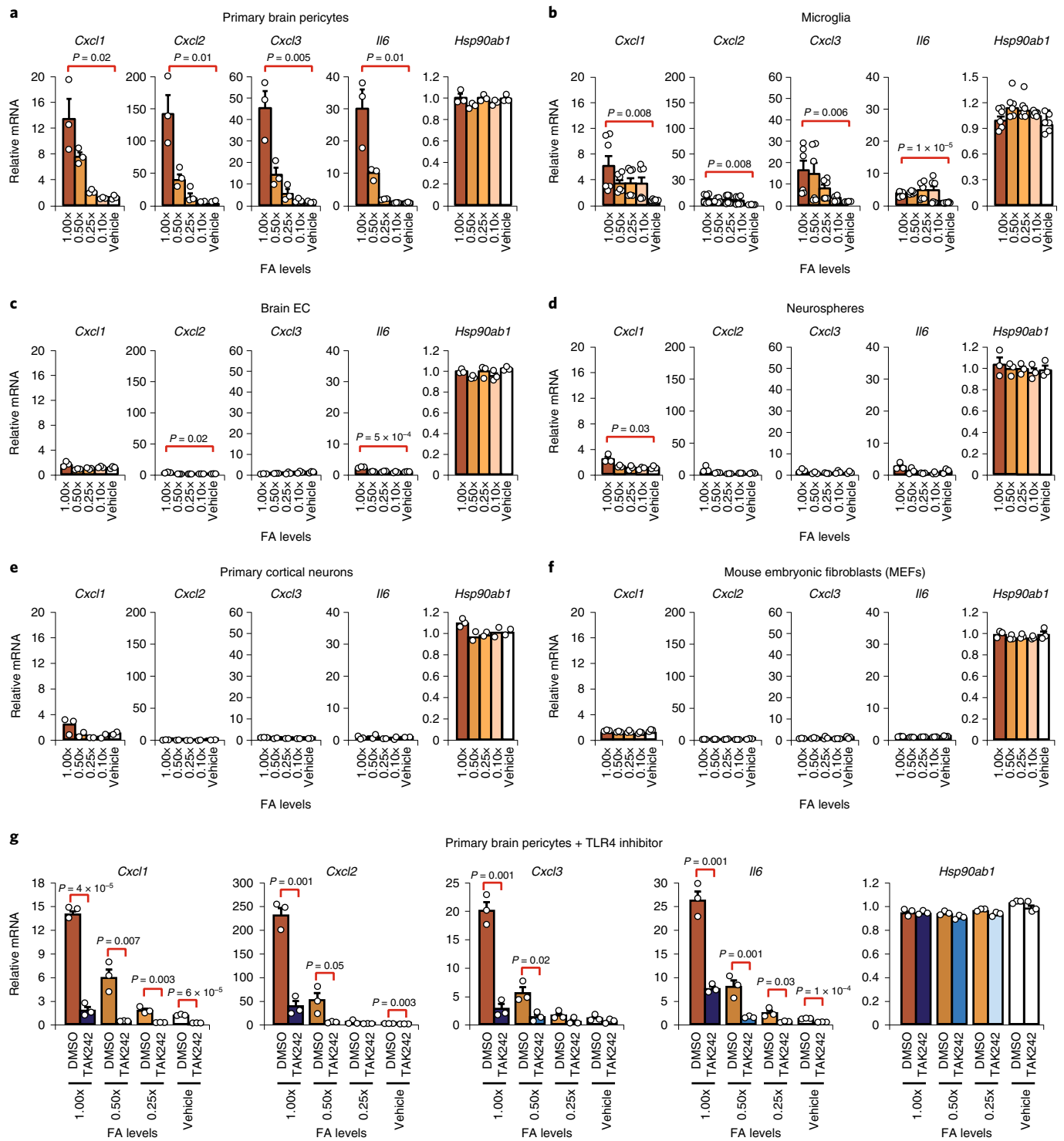


**Fig. 7 | Free LCFAs trigger a TLR4-driven NF $\kappa$ B inflammatory response in pericytes. a–f**, Expression of the pro-inflammatory NF $\kappa$ B target genes *Cxcl1*, *Cxcl2*, *Cxcl3* and *Il6* in primary brain pericytes (**a**), primary microglia (**b**), b.End3 brain endothelial cells (**c**), E14.5 brain-derived neurospheres (**d**), cortical neurons from E16.5 embryonic brains (**e**) and MEFs in response to LCFa treatment (**f**). Only brain pericytes and microglia showed a strong LCFa-induced pro-inflammatory response, which is consistent with the expression of *Tlr4* in these two cell types (Fig. 6g). **g**, LCFa-induced expression of the NF $\kappa$ B target genes *Cxcl1*, *Cxcl2*, *Cxcl3* and *Il6* in primary brain pericytes in the presence of TAK-242 or vehicle (DMSO). Data are presented as the mean  $\pm$  s.e.m. and were analysed using a two-tailed Student's *t*-test. 1.00xFA refers to a cocktail of 200  $\mu$ M C14:0, 200  $\mu$ M C16:0, 20  $\mu$ M C20:0 and 10  $\mu$ M C24:0. Each subsequent treatment was undertaken at the stated fraction of the 1.00x cocktail. Gene expression levels were standardized to *Hsp90ab1* and *Gapdh*. **a**,  $n = 3$  independent experiments. **b**,  $n = 6$  cultures, each from an independent animal. **c**,  $n = 3$  independent experiments. **d**,  $n = 3$  cultures, each from an independent animal. **e**,  $n = 3$  (each from one animal for the 1.00xFA treatment) and 2 (all other treatment concentrations) separate cultures. **f**,  $n = 3$  independent MEF cultures, each from a separate embryo. **g**,  $n = 3$  independent experimental replicates. The value of each biological replicate represents the mean of three technical replicates. Statistical source data are provided.

the brain or zonation of endothelial cells were observed (Fig. 6f, Extended Data Fig. 7a–d and Supplementary Video 1). Together, these analyses suggest that MOF deficiency in neural cells does not impact vascular development but rather leads to morphological changes in pericytes and breakdown of neural microvasculature.

**LCFAs induce pericyte activation in a TLR4-dependent manner.** We were particularly intrigued by the specific activation of pericytes, but not endothelial cells, in response to LCFAs. Given that TLR activation triggers NF $\kappa$ B signalling<sup>40</sup>, and our *in vivo* and *in vitro* analyses showed molecular signatures of TLR-mediated NF $\kappa$ B activation, we screened for expression of TLRs in brain cells in a single-cell RNA-seq (scRNA-seq) dataset of an E18.5 brain<sup>41</sup>. *Tlr4* and *Tlr12* were strongly expressed in pericytes, whereas *Tlr3* was specifically expressed in endothelial cells (Extended Data Fig. 7e). The presence of *Tlr4* in pericytes was particularly interesting, as TLR4 is known to mediate the pro-inflammatory response to free LCFAs in macrophages and adipocytes<sup>42,43</sup>. In agreement with the scRNA-seq data, we found strong expression of *Tlr4* in EMBRACE-isolated pericytes and microglia, but not endothelial or neural cells (Fig. 6g). Consistent with *Tlr4* expression, brain pericytes and microglia strongly activated the NF $\kappa$ B target genes *Cxcl1*, *Cxcl2*, *Cxcl3* and *Il6* in a LCFA-concentration-dependent manner (Fig. 7a,b). This was consistent with the strong activation of NF $\kappa$ B-driven transcriptional networks in pericytes and microglia isolated from *Mof*-nKO brains (Fig. 2f and Extended Data Fig. 8). In contrast, strong LCFA-induced activation of NF $\kappa$ B target genes was not observed in brain endothelial cells, neurospheres, primary cortical neurons or MEFs (Fig. 7c–f), cells that express low levels of *Tlr4*. We next addressed whether we could rescue the LCFA-driven pro-inflammatory response in brain vascular pericytes by inhibiting TLR4. Treatment of pericytes with the TLR4 inhibitor TAK-242 strongly mitigated the pro-inflammatory response to LCFAs (Fig. 7g), suggesting that LCFAs do indeed induce a pro-inflammatory response in vascular pericytes in a TLR4–NF $\kappa$ B-dependent manner.

***Mof* deletion in neural cells induces the accumulation of fatty acids in neighbouring pericytes.** We questioned if there was a direct link between the accumulation of LCFAs in *Mof*-KO neural cells and pericyte activation. We established neurosphere cultures and quantified free fatty acids in the media. We observed increased levels of free fatty acids in the medium of *Mof*-KO neurospheres (Fig. 8a). We next investigated whether LCFAs originating in neurospheres could be taken up by pericytes. We utilized BODIPY FL-C16, a fluorescent mimetic for the LCFA palmitate, which accumulates in primary brain pericytes in a concentration-dependent manner when added to the cell culture medium (Extended Data Fig. 7f). We loaded *Mof*-KO and WT neurospheres with BODIPY

FL-C16 and subsequently introduced WT pericytes, which had no previous exposure to BODIPY FL-C16, into neurosphere cultures (Extended Data Fig. 7g). We detected a two-fold increase in the levels of BODIPY FL-C16 in pericytes co-cultured with *Mof*-KO neurospheres compared with controls (Fig. 8b). This suggests that pericytes are able to detect increased LCFAs resulting from *Mof* depletion in neighbouring neural cells.

**Human KdV fetal brain shows signs of haemorrhaging.** We next explored whether aspects of our mouse models may also be conserved in human patients with KdV carrying mutations in the NSL complex member *KANSL1*. In concordance with the increased ventricular volume in *Mof*-nKO brains and defects in lipid metabolism in *Mof*-KO neurospheres, patients with KdV display a dilation of the lateral ventricle and dysgenesis of the corpus callosum<sup>33</sup>, an area composed almost entirely of complex lipids. While patients with KdV typically display a normal life expectancy, we were able to identify a patient with *KANSL1* deletion that died at 29 weeks of gestation, a developmental time point similar to E14.5 in the mouse. We examined the brain of this patient for signs of haemorrhaging through Prussian blue staining, which marks iron deposits. Interestingly, we observed positive Prussian blue staining in the brain of the fetus with KdV but not in an age-matched control, suggesting the presence of bleeding (Fig. 8c). Together with our mouse models, these analyses suggest that vascular dysfunction may be a feature of KdV and encourages further examination.

## Discussion

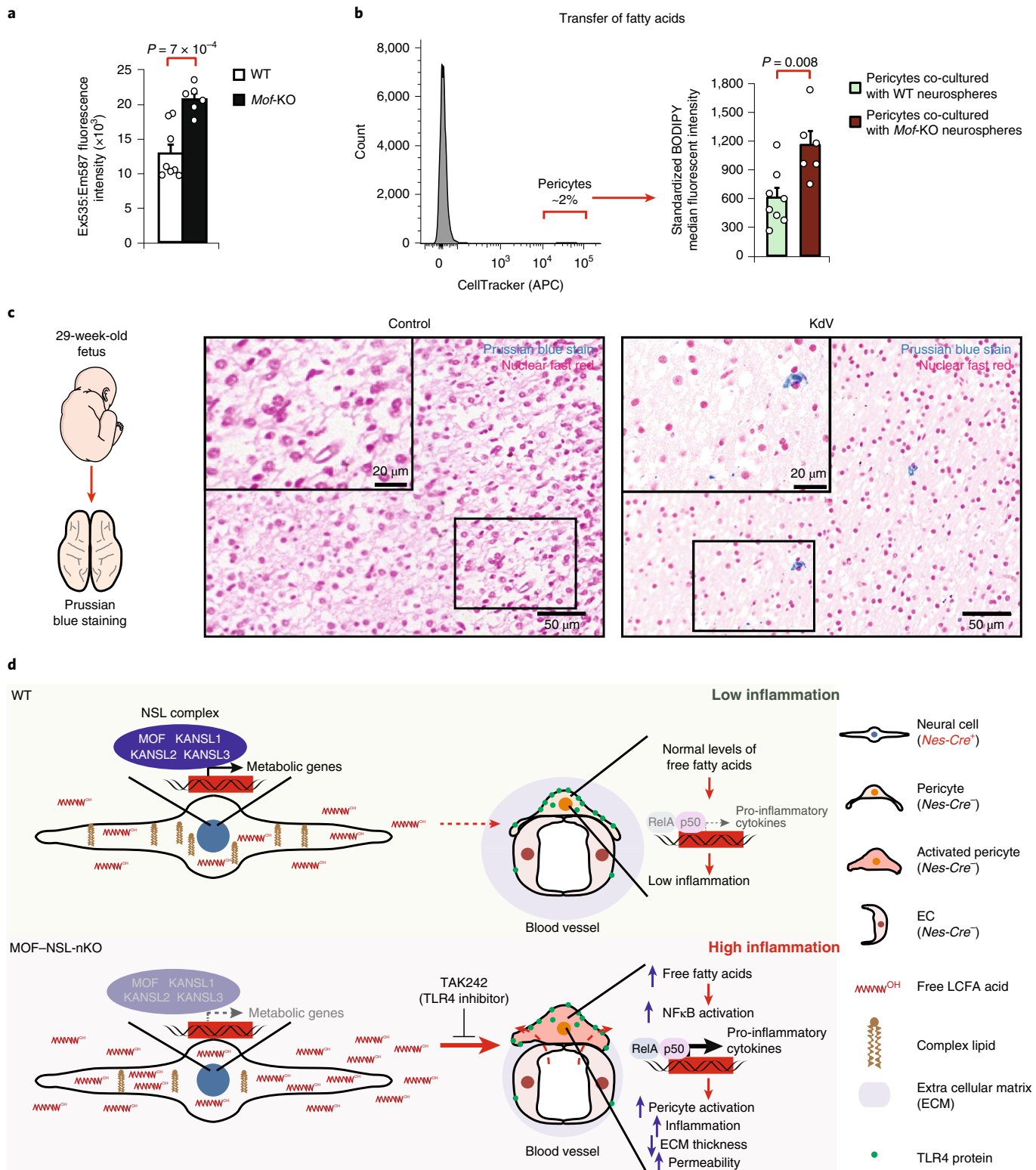
In this study, we set out to address the role of the NSL complex in neural cells through the use of mouse models and complementary mechanistic analyses. We established that the MOF–NSL complex is responsible for maintaining neural cell metabolism in the developing brain. Our complementary *in vivo* and *in vitro* analyses revealed that metabolic defects, in particular an increase in free LCFAs, induce a TLR4–NF $\kappa$ B-mediated inflammatory response in pericytes that leads to increased vascular permeability and haemorrhaging (Fig. 8d). Our work unveils an important and previously unknown metabolite-based example of cell-to-cell communication. Metabolic defects in neural cells are sensed by pericytes, which in turn activate an inflammatory response that results in a loss of vascular integrity in the brain. Thus, changes in the metabolic milieu of one cell type in a complex organ can directly impact the functionality of surrounding cells and thereby affect overall organ function.

Compared with other organs, the neural vasculature is tightly regulated via the blood–brain barrier and closely monitors the transport of proteins and metabolites<sup>44</sup>. Consistent with this, neural vasculature possesses the highest concentration of pericyte coverage, with estimates ranging between one pericyte to every 1–3 endothelial cells<sup>45</sup>. A reduction in pericyte number and increased

**Fig. 8 | Pericytes sense extracellular metabolic changes caused by MOF loss.** **a**, Quantification of extracellular free fatty acids in the cell culture media of *Mof*-KO and control neurosphere cultures.  $n=6$  *Mof*-KO and 8 control WT independent neurosphere cell lines, each generated from an independent embryo. **b**, FA transfer between neural cells and pericytes. *Mof*-KO and control neurosphere cultures were incubated overnight with 1  $\mu$ M BODIPY FL-C16 and subsequently washed three times. WT brain pericytes, which had never previously been exposed to BODIPY FL-C16, were labelled with CellTracker (APC) and added at a ratio of 1:50 pericytes:neurosphere cells. After an overnight incubation, the levels of BODIPY FL-C16 in APC-positive pericytes were analysed using flow cytometry. A diagram depicting the experimental design is provided in Extended Data Fig. 7g.  $n=6$  *Mof*-KO and 8 WT independent neurosphere cultures, each generated from an embryo at E14.5. **a,b**, Data are presented as the mean  $\pm$  s.e.m. and were analysed using a two-tailed Student's *t*-test. **c**, Histology sections of brains from 29-week-old fetuses, control and affected by KdV, stained with Prussian blue and nuclear fast red. Positive Prussian blue staining marks the presence of iron deposits and indicates the presence of bleeding 1–2 d before death. This assay was repeated three times along with positive (sections from patients with known haemorrhaging) and negative controls. Magnified views of the boxed region in the main images are shown in the top left. **d**, Working model. The NSL complex acts at the level of chromatin to maintain expression of metabolic networks. In the absence of the NSL complex, there is deregulation of metabolic gene transcription, leading to significant changes in the neural metabolic milieu. The most significant change is the accumulation of free LCFAs. Free LCFAs also accumulate extracellularly and induce a TLR4–NF $\kappa$ B-dependent pro-inflammatory response in vascular pericytes. The activation of pericytes is sufficient to cause morphological changes that are consistent with increased vascular permeability and haemorrhaging.

vascular permeability has been reported in ageing and neurodegenerative disorders<sup>46,47</sup>. In fact, one of the earliest defects observed in human patients with Alzheimer's disease is increased capillary permeability and breakdown of vascular function, which is associated with damage to pericytes<sup>48</sup>. These findings suggest that vascular defects may precede and promote the development of neurodegenerative disorders. However, a major outstanding question has been how vascular dysfunction occurs in the first place.

Our findings suggest that a defective neural metabolic environment can induce vascular inflammation, pericyte dysfunction and increased vascular permeability. In agreement, administration of the pro-inflammatory TLR4 agonist lipopolysaccharide to mice induces morphological changes in brain pericytes, detachment of pericytes from the vasculature, remodelling of extracellular-matrix components and increased vascular permeability<sup>49</sup>—all of which are defects that we observe in *Mof*-nKO brains. Furthermore, chronic



administration of a high-fat diet in mice induces systemic inflammation, including increased inflammatory cytokines in the brain, and significantly increases the predisposition to neurodegenerative disorders such as Alzheimer's disease<sup>50,51</sup>. Thus, although metabolic disturbances, vascular breakdown and neuroinflammation are known hallmarks of neural disease, our work establishes that neural metabolic disturbances can act as a trigger to induce vascular breakdown and promote a vicious cycle of inflammation that underpins neural pathologies.

Lysine acetylation levels are highly influenced by the cellular metabolic environment<sup>52</sup>. The nutritional state of cells modulates acetyl-CoA levels and subsequently histone acetylation<sup>53</sup>, suggesting that the cellular metabolic state can control aspects of chromatin structure and transcription. Although there is now a building consensus for the metabolic environment regulating chromatin, in the current study we find that the reverse is also true. The NSL complex preferentially targets metabolic genes during neural development and is required to maintain their transcription. Thus, our work uncovers an additional layer of cooperation between the cellular chromatin and metabolic states that is required for homeostasis.

Koolen-de Vries syndrome, arising from *KANSL1* haploinsufficiency, is a debilitating developmental disorder reported in approximately 1:16,000 live births and presents with variable clinical symptoms affecting multiple organs<sup>31,34</sup>. Although KdV is clinically well-defined, the molecular changes have remained unknown. Our analyses of NSL complex mouse models suggest that there are likely to be metabolic and vascular defects in patients with KdV. Consistent with this, dysgenesis of the corpus callosum, a structure rich in complex lipids, is observed in all tested patients with KdV<sup>33</sup>. Furthermore, given the report of dilated ventricles in 85% of patients with KdV<sup>33</sup> and our discovery of haemorrhaging in a fetal KdV brain (Fig. 8c), it is possible that vascular defects are an unappreciated and common feature of KdV pathology. Accordingly, it will be pertinent to determine whether patients with KdV display a defective metabolic profile, signs of neuroinflammation and/or breakdown of vascular function, as treatment of these pathologies will result in better patient outcomes.

Together, our study uncovers the importance of the NSL complex as a 'homeostat' of the neural metabolic environment. Furthermore, we provide evidence that the metabolic environment can regulate the functionality of neural pericytes and thereby vascular function. Our work shows the significance of metabolite-based communication in maintaining brain homeostasis during development. Further work dissecting the contributions of individual cell types will be key to a full understanding of the complex pathophysiology of developmental syndromes.

### Online content

Any methods, additional references, Nature Research reporting summaries, source data, extended data, supplementary information, acknowledgements, peer review information; details of author contributions and competing interests; and statements of data and code availability are available at <https://doi.org/10.1038/s41556-020-0526-8>.

Received: 18 November 2019; Accepted: 22 April 2020;

Published online: 15 June 2020

### References

- Mirabella, A. C., Foster, B. M. & Bartke, T. Chromatin deregulation in disease. *Chromosoma* **125**, 75–93 (2016).
- Butler, J. S., Koutelou, E., Schibler, A. C. & Dent, S. Y. Histone-modifying enzymes: regulators of developmental decisions and drivers of human disease. *Epigenomics* **4**, 163–177 (2012).
- Cho, K. S., Elizondo, L. I. & Boerkoel, C. F. Advances in chromatin remodeling and human disease. *Curr. Opin. Genet. Dev.* **14**, 308–315 (2004).
- van Karnebeek, C. D., Shevell, M., Zschocke, J., Moeschler, J. B. & Stockler, S. The metabolic evaluation of the child with an intellectual developmental disorder: diagnostic algorithm for identification of treatable causes and new digital resource. *Mol. Genet. Metab.* **111**, 428–438 (2014).
- Kinnear, D. et al. Prevalence of physical conditions and multimorbidity in a cohort of adults with intellectual disabilities with and without Down syndrome: cross-sectional study. *BMJ Open* **8**, e018292 (2018).
- Cooper, S. A. et al. Multiple physical and mental health comorbidity in adults with intellectual disabilities: population-based cross-sectional analysis. *BMC Fam. Pract.* **16**, 110 (2015).
- Matson, J. L. & Cervantes, P. E. Comorbidity among persons with intellectual disabilities. *Res. Autism Spectr. Disord.* **7**, 1318–1322 (2013).
- Bannister, A. J. & Kouzarides, T. Regulation of chromatin by histone modifications. *Cell Res.* **21**, 381–395 (2011).
- Rajagopal, N. et al. Distinct and predictive histone lysine acetylation patterns at promoters, enhancers, and gene bodies. *G3* **4**, 2051–2063 (2014).
- Wang, Z. et al. Combinatorial patterns of histone acetylations and methylations in the human genome. *Nat. Genet.* **40**, 897–903 (2008).
- Voss, A. K. & Thomas, T. Histone Lysine and genomic targets of histone acetyltransferases in mammals. *BioEssays* **40**, e1800078 (2018).
- Seto, E. & Yoshida, M. Erasers of histone acetylation: the histone deacetylase enzymes. *Cold Spring Harb. Perspect. Biol.* **6**, a018713 (2014).
- Arboleda, V. A. et al. De novo nonsense mutations in *KAT6A*, a lysine acetyltransferase gene, cause a syndrome including microcephaly and global developmental delay. *Am. J. Hum. Genet.* **96**, 498–506 (2015).
- Petrij, F. et al. Rubinstein–Taybi syndrome caused by mutations in the transcriptional co-activator *CBP*. *Nature* **376**, 348–351 (1995).
- Roelfsema, J. H. et al. Genetic heterogeneity in Rubinstein–Taybi syndrome: mutations in both the *CBP* and *EP300* genes cause disease. *Am. J. Hum. Genet.* **76**, 572–580 (2005).
- Tham, E. et al. Dominant mutations in *KAT6A* cause intellectual disability with recognizable syndromic features. *Am. J. Hum. Genet.* **96**, 507–513 (2015).
- Clayton-Smith, J. et al. Whole-exome-sequencing identifies mutations in histone acetyltransferase gene *KAT6B* in individuals with the Say-Barber-Biesecker variant of Ohdo syndrome. *Am. J. Hum. Genet.* **89**, 675–681 (2011).
- Simpson, M. A. et al. De novo mutations of the gene encoding the histone acetyltransferase *KAT6B* cause Genitopatellar syndrome. *Am. J. Hum. Genet.* **90**, 290–294 (2012).
- Kraft, M. et al. Disruption of the histone acetyltransferase *MYST4* leads to a Noonan syndrome-like phenotype and hyperactivated MAPK signaling in humans and mice. *J. Clin. Invest.* **121**, 3479–3491 (2011).
- Sheikh, B. N. Crafting the brain—role of histone acetyltransferases in neural development and disease. *Cell Tissue Res.* **356**, 553–573 (2014).
- Sheikh, B. N. & Akhtar, A. The many lives of KATs—detectors, integrators and modulators of the cellular environment. *Nat. Rev. Genet.* **20**, 7–23 (2019).
- Thomas, T., Dixon, M. P., Kueh, A. J. & Voss, A. K. Mof (*MYST1* or *KAT8*) is essential for progression of embryonic development past the blastocyst stage and required for normal chromatin architecture. *Mol. Cell Biol.* **28**, 5093–5105 (2008).
- Akhtar, A. & Becker, P. B. Activation of transcription through histone H4 acetylation by MOF, an acetyltransferase essential for dosage compensation in *Drosophila*. *Mol. Cell* **5**, 367–375 (2000).
- Taipale, M. et al. hMOF histone acetyltransferase is required for histone H4 lysine 16 acetylation in mammalian cells. *Mol. Cell Biol.* **25**, 6798–6810 (2005).
- Chelmicki, T. et al. MOF-associated complexes ensure stem cell identity and *Xist* repression. *eLife* **3**, e02024 (2014).
- Shogren-Knaak, M. et al. Histone H4-K16 acetylation controls chromatin structure and protein interactions. *Science* **311**, 844–847 (2006).
- Gilissen, C. et al. Genome sequencing identifies major causes of severe intellectual disability. *Nature* **511**, 344–347 (2014).
- Koolen, D. A. et al. Mutations in the chromatin modifier gene *KANSL1* cause the 17q21.31 microdeletion syndrome. *Nat. Genet.* **44**, 639–641 (2012).
- Zollino, M. et al. Mutations in *KANSL1* cause the 17q21.31 microdeletion syndrome phenotype. *Nat. Genet.* **44**, 636–638 (2012).
- Sheikh, B.N., Guhathakurta, S. & Akhtar, A. The non-specific lethal (NSL) complex at the crossroads of transcriptional control and cellular homeostasis. *EMBO Rep.* **20**, e47630 (2019).
- Koolen, D. A. et al. Clinical and molecular delineation of the 17q21.31 microdeletion syndrome. *J. Med. Genet.* **45**, 710–720 (2008).
- Morgan, A. T. et al. Early speech development in Koolen de Vries syndrome limited by oral praxis and hypotonia. *Eur. J. Hum. Genet.* **26**, 75–84 (2018).
- Myers, K. A. et al. The epileptology of Koolen-de Vries syndrome: electro-clinico-radiologic findings in 31 patients. *Epilepsia* **58**, 1085–1094 (2017).
- Koolen, D. A. et al. The Koolen-de Vries syndrome: a phenotypic comparison of patients with a 17q21.31 microdeletion versus a *KANSL1* sequence variant. *Eur. J. Hum. Genet.* **24**, 652–659 (2016).

35. Raja, S. J. et al. The nonspecific lethal complex is a transcriptional regulator in *Drosophila*. *Mol. Cell* **38**, 827–841 (2010).
36. Ballabh, P. et al. Angiogenic inhibition reduces germinal matrix hemorrhage. *Nat. Med.* **13**, 477–485 (2007).
37. Braun, A. et al. Paucity of pericytes in germinal matrix vasculature of premature infants. *J. Neurosci.* **27**, 12012–12024 (2007).
38. Sheikh, B. N. et al. Systematic Identification of cell–cell communication networks in the developing brain. *iScience* **21**, 273–287 (2019).
39. Fuchs, C. D. et al. Absence of adipose triglyceride lipase protects from hepatic endoplasmic reticulum stress in mice. *Hepatology* **56**, 270–280 (2012).
40. Liu, T., Zhang, L., Joo, D. & Sun, S.C. NF- $\kappa$ B signaling in inflammation. *Signal Transduct. Target. Ther.* **2**, 17023 (2017).
41. Han, X. et al. Mapping the mouse cell atlas by Microwell-seq. *Cell* **172**, e1017 (2018).
42. Huang, S. et al. Saturated fatty acids activate TLR-mediated proinflammatory signaling pathways. *J. Lipid Res.* **53**, 2002–2013 (2012).
43. Shi, H. et al. TLR4 links innate immunity and fatty acid-induced insulin resistance. *J. Clin. Invest.* **116**, 3015–3025 (2006).
44. Zhao, Z., Nelson, A. R., Betsholtz, C. & Zlokovic, B. V. Establishment and dysfunction of the blood–brain barrier. *Cell* **163**, 1064–1078 (2015).
45. Armulik, A., Genove, G. & Betsholtz, C. Pericytes: developmental, physiological, and pathological perspectives, problems, and promises. *Dev. Cell* **21**, 193–215 (2011).
46. Montagne, A. et al. Blood–brain barrier breakdown in the aging human hippocampus. *Neuron* **85**, 296–302 (2015).
47. Sengillo, J. D. et al. Deficiency in mural vascular cells coincides with blood–brain barrier disruption in Alzheimer’s disease. *Brain Pathol.* **23**, 303–310 (2013).
48. Nation, D. A. et al. Blood–brain barrier breakdown is an early biomarker of human cognitive dysfunction. *Nat. Med.* **25**, 270–276 (2019).
49. Nishioku, T. et al. Detachment of brain pericytes from the basal lamina is involved in disruption of the blood–brain barrier caused by lipopolysaccharide-induced sepsis in mice. *Cell Mol. Neurobiol.* **29**, 309–316 (2009).
50. Busquets, O. et al. Long-term exposition to a high fat diet favors the appearance of  $\beta$ -amyloid depositions in the brain of C57BL/6J mice. A potential model of sporadic Alzheimer’s disease. *Mech. Ageing Dev.* **162**, 38–45 (2017).
51. Denver, P., Gault, V. A. & McClean, P. L. Sustained high-fat diet modulates inflammation, insulin signalling and cognition in mice and a modified xenin peptide ameliorates neuropathology in a chronic high-fat model. *Diabetes Obes. Metab.* **20**, 1166–1175 (2018).
52. Choudhary, C., Weinert, B. T., Nishida, Y., Verdin, E. & Mann, M. The growing landscape of lysine acetylation links metabolism and cell signalling. *Nat. Rev. Mol. Cell Biol.* **15**, 536–550 (2014).
53. Marino, G. et al. Regulation of autophagy by cytosolic acetyl-coenzyme A. *Mol. Cell* **53**, 710–725 (2014).

**Publisher’s note** Springer Nature remains neutral with regard to jurisdictional claims in published maps and institutional affiliations.

© The Author(s), under exclusive licence to Springer Nature Limited 2020

## Methods

**Animals.** All animal studies were performed according to the German animal care and ethics legislation and were approved by the local government authority, the Committee on Research Animal Care, Regierungspräsidium Freiburg (G-17/102). The study is compliant with all relevant ethical regulations regarding animal research. The *Mof*-floxed<sup>22</sup> and *Nes-Cre* mouse<sup>24</sup> strains have been previously described. The *Nes-Cre* model explicitly utilizes the neural-specific enhancer from the second intron of the *Nestin* gene and therefore does not recapitulate the expression pattern of endogenous *Nestin* but is specific for neural cells in the brain<sup>54–58</sup>. The *Caag-Cre-ERT2* and *Gt(ROSA)26Sor<sup>tm4(AC1TB-tdTomato,-EGFP)LoxP</sup>* (referred to as *mT/mG*; Extended Data Fig. 3b) mice were purchased from Jackson Laboratories. Embryonic stem cells with a targeted *Kansl2* allele (*tm1a*(EUCOMM)Wtsi) were purchased from the International Knockout Mouse Consortium (IKMC; Extended Data Fig. 1a). A vector targeting the *Kansl3* allele was obtained from J. Rientjes (Monash, Australia) and electroporated into freshly isolated embryonic stem cells for targeting (Extended Data Fig. 1a). Embryonic stem cell clones showing correctly targeted *Kansl2* and *Kansl3* alleles were used to generate chimaeras and backcrossed onto a C57BL/6 background. Genotyping was undertaken through standard PCR using the primers listed in Supplementary Table 1. All of the strains were maintained on a C57BL/6 background, under a 14-h light and 10-h dark cycle. Water and standard chow were provided ad libitum.

**Neurosphere culture.** Neurosphere colonies were established from brains isolated from *Mof<sup>fl/fl</sup> Caag-Cre-ERT2<sup>+/+</sup>* and *Mof<sup>fl/fl</sup>* controls at E14.5. The forebrains were dissected, the cortex was removed, and the medial and lateral ganglionic eminence were retained. The samples were washed once in 10 ml sterile PBS and resuspended in neurosphere medium. A single-cell suspension was prepared by triturating with a 200  $\mu$ l pipette. The dissociated cells were passed through a 40- $\mu$ m sieve and cultured in six-well plates in Neurosphere medium (1 $\times$ N2 supplement (Life Technologies, 17502048), 0.2% glucose, 2 mM GlutaMAX, 0.1125% sodium bicarbonate, 15 mM HEPES, 4  $\mu$ g ml<sup>-1</sup> heparin, 20 ng ml<sup>-1</sup> EGF (R&D Systems, 236-EG-200), 10 ng ml<sup>-1</sup> bFGF (R&D Systems, 233-FB-025) and 0.2% BSA, made up in DMEM/F12 (Gibco, 21331-020)). For passaging, neurospheres were collected by brief centrifugation (200g, 4 min), resuspended in accutase (Sigma, A6964), incubated at 37 °C for 1–3 min depending on the passage number, dissociated using a P1000 pipette, washed in DMEM/F12 medium and re-plated in neurosphere medium. The neurospheres were split at a ratio of 1:5 to 1:6. The neurospheres were plated at a density of 30,000 cells cm<sup>-2</sup> for experiments. After plating (24 h), 5  $\mu$ M tamoxifen (4-hydroxytamoxifen; Sigma, T176) was added to both *Mof<sup>fl/fl</sup> Caag-Cre-ERT2<sup>+/+</sup>* (*Mof-KO*) and *Mof<sup>fl/fl</sup>* (WT) cultures for 2 d. The neurospheres were subsequently washed and re-plated without tamoxifen for 24 h before analyses. Cultures were maintained at 37 °C and 5% CO<sub>2</sub>.

**MEFs.** The MEF lines were established as previously described<sup>59</sup>. Briefly, E13.5 embryos were collected from the male *Mof<sup>fl/fl</sup> Caag-Cre-ERT2<sup>+/+</sup>*  $\times$  female *Mof<sup>fl/fl</sup>* cross. The animals were decapitated and organs were removed. The carcass was incubated on ice for 30 min with 500  $\mu$ l of a 2.5% (wt/vol) pancreatin and 0.5% (wt/vol) trypsin solution. The pancreatic trypsin solution was removed and the carcass was incubated at 37 °C for 5 min. The reaction was stopped by adding 1,000  $\mu$ l of 2% FCS in PBS solution. The tissue was dissociated using a P1000 pipette, washed once and plated in a 15-cm dish in complete MEF medium (DMEM supplemented with GlutaMAX (Life Technologies), 100 U ml<sup>-1</sup> penicillin, 100  $\mu$ g ml<sup>-1</sup> streptomycin and 10% FCS). The cells were counted at every passage and plated at a density of 12,500 cells cm<sup>-2</sup>. All experiments were undertaken at passage 3. To induce *Mof* deletion, *Mof<sup>fl/fl</sup> Caag-Cre-ERT2<sup>+/+</sup>* (*Mof-KO*) as well as control *Mof<sup>fl/fl</sup>* (WT) MEFs were treated with 1  $\mu$ M tamoxifen (Sigma, T176) for 3.5 d. The cells were maintained at 37 °C with 5% CO<sub>2</sub>.

**Endothelial cell culture.** The brain endothelial cell line b.End3 was cultured on plates coated with 0.4% gelatine in DMEM medium supplemented with GlutaMAX, 100 U ml<sup>-1</sup> penicillin, 100  $\mu$ g ml<sup>-1</sup> streptomycin and 10% FCS. The cells were maintained at 37 °C in 10% CO<sub>2</sub>. The cells were split 1:3 at confluence.

**Cortical neuron culture.** Wild-type C57/BL6 embryos at E16.5 were collected and killed by cervical dislocation. The cortices were acutely dissected and incubated in 400  $\mu$ l digestion solution (0.13 Wünsch units (WU) ml<sup>-1</sup> Liberase TM (Worthington, Roche, 05401119001), 80 U ml<sup>-1</sup> DNase I (NEB) and 5 mM MgCl<sub>2</sub> in PBS) and incubated at 37 °C in a thermoshaker set at 800 r.p.m. for 40 min. The cortices were triturated using a P1000 pipette, passed through a 70- $\mu$ m cell sieve, collected by centrifugation (200g, 4 min) and plated in 6-cm plates pre-coated with laminin. The plates were coated with laminin (Life Technologies, 23017-015) diluted to 20  $\mu$ g ml<sup>-1</sup> in PBS supplemented with Mg<sup>2+</sup> and Ca<sup>2+</sup> for 2 h at 37 °C, and washed twice previous to plating. The cells were maintained in cortical neuron medium (NeuroBasal medium (Life Technologies, 21103-049) supplemented with B27 (Life Technologies, 17504-044), 100 U ml<sup>-1</sup> penicillin, 100  $\mu$ g ml<sup>-1</sup> streptomycin and 2 mM GlutaMAX). The medium was changed 48 h after culture and neurons were treated with LCFAs on day 5 of culture for a total treatment time of 16 h.

**Microglia culture.** Primary microglia were prepared from the hippocampal and cortical regions of postnatal day 2 C57BL6/J mice. Brain homogenates were filtered through 70- $\mu$ m filters and the cell suspensions were seeded in 75-cm<sup>2</sup> flasks with filter covers (TPP, 90026). The flasks were pre-coated with 5 ml poly-L-lysine (Sigma, P8920), incubated for 1 h and washed three times with PBS. The cells were cultured in DMEM medium (Thermo Fischer, 11971-025) supplemented with 10% FCS (Thermo Fischer, 10270106) and 1% penicillin/streptomycin (Biochrom, A2213) for 14 d to form a confluent cell monolayer. The medium was changed every 2–4 d. M-CSF (25 ng ml<sup>-1</sup>; Peprotech, 315-02) was added to the culture in fresh medium 24 h before harvesting the microglia. To passage the microglia, the cultures were shaken on a rotary shaker (200 r.p.m.) for 2 h. The detached microglia were counted and seeded in fresh medium with M-CSF in six-well plates pre-coated with poly-L-lysine (3  $\times$  10<sup>5</sup> cells per well).

**Primary pericyte isolation and culture.** Pericytes were isolated from adult mouse brains based on the protocols of Tigges and co-workers<sup>60</sup>. Briefly, six brains were isolated from six- to eight-week-old mice. The olfactory bulbs, cerebellum and medulla were removed and the brains were thinly sliced using a sterile razor blade. After washing in MEM solution (Thermo Scientific, 41090093), tissue from the six brains was pooled and collected by centrifugation (300g, 5 min). The tissue was incubated in enzymatic solution at 37 °C for 70 min with gentle mixing every 10 min. The enzymatic solution was made using the Papain dissociation system (Worthington, LK003150) with 30 U ml<sup>-1</sup> papain, 40 mg ml<sup>-1</sup> DNase type IV and 0.24 mg ml<sup>-1</sup> L-cysteine in Earl's balanced salt solution. The digested tissue was further homogenized by passing the brain tissue ten times through an 18-gauge needle, followed by passing the homogenate a further ten times through a 21-gauge needle. The cells were washed and transferred to a 15-ml Falcon tube containing 1.7  $\times$  volume of 22% BSA to remove myelin. The cells were collected by centrifugation (1,000g, 10 min), the lipid layer was removed and the cell pellet was resuspended in 5 ml endothelial cell growth medium (10% FCS, 25  $\mu$ g ml<sup>-1</sup> heparin, 1  $\mu$ g ml<sup>-1</sup> ascorbic acid, 2 mM GlutaMAX, 100 U ml<sup>-1</sup> penicillin, 100  $\mu$ g ml<sup>-1</sup> streptomycin and 30  $\mu$ g ml<sup>-1</sup> endothelial growth supplement (Millipore, 02-102) in Hams F12 solution). The cells were collected by centrifugation (300g, 5 min), resuspended in 4 ml endothelial cell growth medium and plated in two 3.5-cm collagen-coated plates. Twenty hours after plating, the cells were washed three times in PBS and given fresh medium. The cells were passaged at a ratio of 1:4 every 7 d for the first two passages. Following the second passage, the cells were cultured in pericyte medium (ScienCell, 1201) and were confluent every 3–4 d.

**LCFA treatment.** The LCFAs were purchased from Sigma and dissolved in 100% ethanol at the following concentrations: C14:0, 200 mM (M3128); C16:0, 200 mM (P0500); C20:0, 20 mM (A3631) and C24:0, 5 mM (L6641). Fatty-acid-free BSA (Sigma, A8806) was dissolved in PBS to a final concentration of 11% and filter sterilized. The LCFAs were conjugated with the fatty-acid-free BSA at 37 °C for 2 h and then added to cells at the indicated concentrations. The FA high cocktail consisted of 200  $\mu$ M C14:0, 200  $\mu$ M C16:0, 20  $\mu$ M C20:0 and 10  $\mu$ M C24:0; the FA medium cocktail consisted of 50  $\mu$ M C14:0, 50  $\mu$ M C16:0, 5  $\mu$ M C20:0 and 2.5  $\mu$ M C24:0. As the MEFs and b.End3 cells were cultured in 10% FCS, the fatty acids were depleted from the FCS used in the MEF and b.End3 media using the lipid removal agent (LRA; Sigma, 13360-U Supelco) before performing experiments. Microglia were treated with LCFAs in the presence of 0.5% FCS. The cells were analysed 16 h after the addition of the LCFAs. For rescue experiments, TAK-242 (Sigma, 614316) was added to the cells at a final concentration of 1  $\mu$ M for 30 min before the administration of LCFAs.

**Fatty acid depletion from FCS.** Fatty acids were depleted from FCS using LRA (Sigma, 13360-U Supelco). Briefly, 1 g LRA was added to 25 ml FCS and incubated overnight on a spinning wheel at 4 °C. The LRA was removed by centrifuging twice at 4,000 r.p.m. (4 min) and the supernatant was kept. The FCS was subsequently filter sterilized.

**Neurosphere and pericyte co-culture.** *Mof-KO* and WT neurospheres were supplemented with 1  $\mu$ M BODIPY FL-C16 (4,4-difluoro-5,7-dimethyl-4-bora-3a,4a-diaza-s-indacene-3-hexadecanoic acid; Life Technologies, D3821). After culturing overnight (18 h), the neurospheres were washed three times and resuspended in 20 ml DMEM/F12 basal medium supplemented with 0.1125% sodium bicarbonate. Wild-type brain pericytes were labelled by incubating with 1  $\mu$ M CellTracker deep red dye (Life Technologies, C34565) for 30 min, and then washed, trypsinized and plated with neurospheres at ratio of approximately 1:50 pericytes:neurosphere cells. The neurosphere-pericyte co-culture was maintained overnight in neurosphere medium and the BODIPY FL-C16 levels were quantified in APC-positive pericytes by flow cytometry on a BD Fortessa instrument. The median fluorescence intensity of BODIPY FL-C16 in pericytes was standardized to the ratio of pericytes:neurosphere cells to ensure the data correctly reflected the number of neurosphere cells in culture.

**Histology.** Embryos were collected at E14.5, killed by decapitation and fixed in 4% paraformaldehyde. Sections of 4- $\mu$ m thickness were cut and stained with haematoxylin and eosin. Prussian blue staining was conducted as follows: slides

were deparaffinized in xylene, incubated in a freshly mixed staining solution containing 50 ml of 2% potassium hexacyanoferrate (II) trihydrate solution (Merck, 1.04984.0500) and 50 ml of 1 M hydrochloric acid (Fisher Scientific, J/4320/15) for 30 min. The slides were washed extensively in water, counterstained with Nuclear fast red (Morphisto, 10264.00500), transferred to xylene and coverslipped using Vitro-Clud (R. Langenbrinck, 04-0001) as the mounting reagent. Histological images were acquired using a BZ-9000 microscope (BioRevo, Keyence).

**MRI scans.** Embryos at E14.5 were fixed in 4% paraformaldehyde supplemented with 2 mM gadolinium (III) for 10 d at 4 °C. After 10 d, the samples were embedded in 1% low-melt agarose supplemented with 2 mM gadolinium (III) and imaged on a 9.4 T small-bore animal scanner (BioSpec 94/21, Bruker Biospin) using a dedicated mouse quadrature-resonator (Bruker). The MRI protocol consisted of two localizers and a T2-weighted TurboRARE (rapid acquisition with relaxation enhancement) three-dimensional (3D) sequence. The TurboRARE 3D sequence that was used to delineate the ventricles featured a field of view of  $13 \times 13 \times 13$  mm, a matrix size of  $256 \times 256 \times 64$  pixels and a resolution of  $51 \times 51 \times 203$   $\mu\text{m}$  (TR/TEeff/FA: 1,800 ms/36 ms/180°). Volumetric analyses were performed using the MIPAV software (v7.3.0, NIH).

**Electron microscopy.** Brains from E14.5 embryos were acutely dissected and fixed in a freshly prepared solution of 4% paraformaldehyde and 0.05% glutaraldehyde in PBS. Sections (50  $\mu\text{m}$ ) were then cut on a vibratome, followed by contrastation using 1% osmium tetroxide (Sigma-Aldrich). After dehydration, the samples were embedded in epoxy resin (Durcupan, Sigma-Aldrich) and ultrathin sections were prepared using a Leica UC6 ultramicrotome. Ultrathin sections were analysed using a CM100 Philips transmission electron microscope. The diameter of the blood vessels was quantified by measuring the cross-section of each vessel across three different points and then calculating their average.

**Immunofluorescence.** For immunofluorescence staining, brains from E14.5 embryos were frozen in optimal cutting template (VWR, 00411243). Sections with a 6- $\mu\text{m}$  thickness were cut on a cryostat and placed on gelatine-coated slides. For staining, the slides were defrosted and fixed in 4% paraformaldehyde. Permeabilization was performed using 0.3% Triton X-100 for 20 min, and sections were blocked in the appropriate buffer as outlined in Supplementary Table 4. The sections were incubated with the appropriate primary antibodies (Supplementary Table 4) for 60 min at room temperature in a wet box. After three washes at room temperature, cells were incubated with secondary Alexa-Fluor-conjugated antibodies (Supplementary Table 4). The cells were counterstained using DAPI (1:500) and imaged on the LSM 780 part of an Elyra PS1 microscope (Zeiss), using an EC Plan Neofluar  $\times 10/0.3$  air objective for overview images and a Plan Apochromat  $\times 63/1.4$  oil objective for zoomed-in images. The 405 nm, 488 nm, 561 nm and 642 nm laser lines and standard filter sets were used. For quantification of proliferating cells in the ventricular zone, phospho-H3-positive cells were manually counted in the first three cell layers immediately adjacent to the lateral ventricle.

**Light-sheet microscopy.** Brains from E14.5 embryos were acutely isolated and passively cleared using the PACT method<sup>64</sup>. Briefly, the brains were fixed in 4% paraformaldehyde for 1 h and then incubated overnight at 4 °C in a hydrogel monomer solution (A4P0; 4% acrylamide and 0.25% photo-initiator (no. VA-044) in PBS). This was followed by nitrogen degassing and the samples were incubated at 37 °C for 3–5 h to initiate tissue–hydrogel hybridization. The tissue–hydrogel matrices were then incubated in 8% SDS for 2–5 d at 37 °C for tissue clearing. For immunostaining, the cleared brain samples were incubated with an antibody raised against PECAM1 (1:250; Supplementary Table 4) in a buffer containing 2% FCS, 0.1% Triton X-100 and 0.01% sodium azide for 7 d at room temperature. Following washing, the brains were incubated with fluorescently labelled secondary antibodies for a further 7 d. After washing in PBS, the samples were embedded in 2% low-melting-agarose cylinders and incubated in RIMS medium for refractive-index matching for 2 d before 3D image acquisition in the same medium with a Light-sheet Z.1 microscope (Zeiss) using a 561 nm laser, a standard filter set, EC Plan-NEOFLUAR  $\times 5/0.16$  detection objective and PCO.Edge sCMOS camera (PCO). Data were visualized and analysed using Imaris software (v9.1.0, Bitplane) and arivis Vision4D software (Arivis). Vessels associated with the meninges were excluded from all analyses.

**Blood vasculature analysis of 100- $\mu\text{m}$  gelatine-embedded sections.** Brains from E14.5 embryos were fixed for 2 h in 4% paraformaldehyde and embedded in a solution containing 6.3% (wt/vol) gelatine and 27% (wt/vol) albumin in water. Once embedded, the samples were further fixed overnight in 4% paraformaldehyde at 4 °C. Sections with a thickness of 100  $\mu\text{m}$  were cut on a vibratome (Zeiss) and stored in PBS. For staining, the sections were fixed again in 4% paraformaldehyde for 30 min, rinsed in PBS and blocked overnight in 10% FCS. The sections were stained overnight with antibodies raised against PECAM1 and PDGFR $\beta$  at 4 °C (Supplementary Table 4). The sections were washed four times over a 6-h period and then incubated overnight with secondary anti-goat Alexa 488 and anti-rabbit Alexa 555 antibodies (Supplementary Table 4) at 4 °C. After a further four washes,

the sections were placed on slides, coverslipped and imaged using the Zeiss LSM 780 confocal system. The acquired images were processed using Imaris (v9.1.0) to extract the relevant statistics. Blood vessels associated with the meninges were excluded from all analyses. To determine the recruitment of mural cells to blood vessels, the intensity of raw PDGFR $\beta$ :PECAM1 signal was calculated. No distinction between the types of blood vessels was made for these analyses.

**ECIS.** Slides (8W10E) were pre-treated with 10 mM L-cysteine for 30 min, washed twice with ddH<sub>2</sub>O and coated with fibronectin for 1 h (for endothelial culture) or collagen for 2 h (for pericyte culture). Primary dermal endothelial cells ( $1 \times 10^5$ ) or  $4.5 \times 10^4$  primary brain pericytes were seeded onto the electrodes and cultured to confluence. Continuous impedance measurements were performed at 37 °C and 10% CO<sub>2</sub> for primary endothelial cells or at 5% CO<sub>2</sub> for primary pericytes using an ECIS Z $\Theta$  instrument (Applied Biophysics). Resistance of the monolayer was calculated using the ECIS software (Applied Biophysics) before and after the addition of LCFAs.

**Metabolic analysis. GC–MS analysis.** Neurosphere cultures were spun down (200g, 4 min) and washed twice in ice-cold PBS. The pellets were snap frozen and metabolite extraction for all samples was done simultaneously. The pellets were thawed on ice, 1 ml of an 80:20 ethanol:water solution was added together with spike-in controls (norvaline and D27 myristic acid) and the samples were shaken at 70 °C for 3 min. The samples were briefly incubated on ice and centrifuged (20,000g, 4 °C, 5 min), and the supernatant was kept for analyses. The cell pellets were stored for protein quantification and standardization of MS data. The supernatant was centrifuged (20,000g, 4 °C, 5 min), transferred to new tubes, dried in a speed-vac (room temperature) and metabolites were stored at –80 °C before measuring. For measurements, the samples were resuspended in 15  $\mu\text{l}$  pyridine with 10 mg ml<sup>–1</sup> methoxyamine and incubated at 30 °C for 1 h. Subsequently, the samples were centrifuged for 3 min at 20,000g, and 10  $\mu\text{l}$  of the supernatant was transferred to a GC vial. Automated just-in-time derivatization (addition of 20  $\mu\text{l}$  *N*-tert-butyltrimethylsilyl-*N*-methyltrifluoroacetamide with 1% tert-butyl-dimethyl-chlorosilane, followed by mixing and 1 h incubation at 80 °C) was performed directly before measurement on an Agilent 7890 GC with a DB5MS 30 m  $\times$  0.25 mm  $\times$  0.25  $\mu\text{m}$  column coupled to an Agilent 5977 MS using EI ionization. Peaks were identified by comparison of the retention time and mass spectrum to known standards and to the National Institute of Standards and Technology (NIST) library. Quantification was based on the peak areas. The metabolite levels were standardized to internal controls and cell numbers, which were estimated through protein quantification.

**Lipidomics.** Ice-cold methanol (400  $\mu\text{l}$ ) and 400  $\mu\text{l}$  ice-cold water was added to pelleted neurospheres. The samples were thoroughly mixed by vortexing and transferred to glass tubes. Next, 800  $\mu\text{l}$  chloroform was added and the samples were shaken for 5 min. The samples were centrifuged (3,500 r.p.m., swing rotor, 4 °C, 5 min), and 750  $\mu\text{l}$  of the hydrophobic phase was extracted using a glass pipette and transferred to 2-ml glass tubes. The material at the interphase of the hydrophobic and hydrophilic phases was saved for protein quantification. The lipid-containing supernatants were split in two, one for measurement of positively charged lipids and the other for negatively charged lipids. The samples were dried in a speed-vac (room temperature) and stored at 4 °C. Before measurement, the samples were reconstituted in 50  $\mu\text{l}$  of a 2:1:1 mix of 2-propanol:acetonitrile:water and measured by targeted lipidomics on an Agilent 1290 infinity II UHPLC coupled to a Bruker impact II QTOF-MS. The lipid levels were standardized to the total cell number, which was estimated through protein quantification.

**Free-LCFA analyses.** These analyses were based on the method of Fuchs and co-workers<sup>77</sup>. Pelleted and frozen neurospheres were resuspended in 1 ml of a 50:50 methanol:water solution. After transferring to glass tubes, 10  $\mu\text{l}$  <sup>13</sup>C-labelled C26:0 was added as a spike-in control. The samples were mixed, and 1,000  $\mu\text{l}$  chloroform was added and mixed via vortexing for 5 min at room temperature. The samples were centrifuged (3,600 r.p.m., swing bucket rotor, 4 °C, 5 min) and the chloroform hydrophobic phase was kept. The remaining sample including the hydrophilic phase was dried and used for protein quantification. The hydrophobic phase was dried in a speed-vac (20 min, temperature off) and resuspended in 50  $\mu\text{l}$  acetonitrile. Next, 1.7  $\mu\text{l}$  2,3,4,5,6-pentafluorobenzyl bromide (1 g ml<sup>–1</sup>; Sigma, 101052) and 10  $\mu\text{l}$  2-(diisopropylamino)ethanol (Sigma, 471488) were added to each sample. The samples were mixed at room temperature for 20 min, dried in a speed-vac and resuspended in 40  $\mu\text{l}$  heptane for measurement. The samples were measured on an Agilent 7890 GC with a DB5MS 30 m  $\times$  0.25 mm  $\times$  0.25  $\mu\text{m}$  column coupled to an Agilent 5977 MS using EI ionization. Peaks were identified by comparison of the retention time and mass spectrum to known standards. Quantification was based on the peak areas. Free-FA levels were standardized to the <sup>13</sup>C-C26:0 spike-in control and cell numbers (estimated by protein quantification).

**Free fatty acid measurements in medium.** Free fatty acids in neurosphere medium were quantified using the BioVision free fatty acid quantification kit (K612) as per manufacturer's instructions. 50  $\mu\text{l}$  of neurosphere medium was used per test and measurements were performed in duplicate.

**Total fatty acid extraction from MEFs.** *Mof<sup>fl/fl</sup> Caag-Cre-ERT2<sup>+/+</sup> (Mof-KO)* and *Mof<sup>fl/fl</sup> (WT)* cells were treated with tamoxifen (1  $\mu$ M, 3.5 d), passaged and plated overnight at a density of 17,000 cells  $\text{cm}^{-2}$ . Reference plates were set up in parallel for cell counting to standardize the data to the precise number of cells in each culture. For the extraction of fatty acids, cells were collected in glass vials in a mixture of 80% methanol and 20% hydrochloric acid (pure, 34%) and thoroughly mixed. D27 myristic acid was spiked in as a control. The mixture was incubated at 99 °C for 2 h. After cooling, the fatty acids were extracted twice using hexane: Hexane (2 ml) was added to each vial, thoroughly mixed by vortexing and incubated at room temperature for 5 min. The vials were then centrifuged for 1 min at 1,800g and the hexane phase was retained. Hexane was dried under  $\text{N}_2$  gas and the samples were resuspended in 30  $\mu$ l heptane. The fatty acids were measured on an Agilent 7890 GC with a DB5MS 30 m  $\times$  0.25 mm  $\times$  0.25  $\mu$ m column coupled to an Agilent 5977 MS using EI ionization. Peaks were identified by comparison of the retention time and mass spectrum to known standards and to the NIST library. Quantification was based on peak areas.

**Seahorse analysis.** Mitochondrial respiration analyses were carried out essentially as previously described<sup>62</sup>. However, 50,000 freshly isolated cells from embryo brains at E14.5 were plated in each well for analysis. Analyses were carried out 2 h after plating. All drugs—oligomycin, FCCP, rotenone and antimycin A—were purchased from Sigma and used at a final concentration of 1  $\mu$ M.

**Mitochondrial DNA quantification.** For the isolation of DNA, cells were lysed in SDS buffer and treated with proteinase K (Thermo Scientific, 25530015) and RNase A (Sigma-Aldrich, R4875). DNA was purified using phenol:chloroform and precipitated using 0.1 $\times$ volume sodium butyrate (3 M) and 2.5 $\times$ volume ethanol (100%). The levels of mitochondrial DNA content were determined by quantifying the *Rnr1*, *Col1*, *Atp6* and *Nd6* alleles encoded by the mitochondrial genome and standardizing these data to the autosomal genome loci *Tra2b* and *Opa1*. Quantification was carried out using SYBR green chemistry (SensiMix, Bioline QT605) on a LightCycler 480 (Roche). Primer sequences are provided in Supplementary Table 3.

**Flow cytometry.** Neural cells, pericytes, endothelial cells and microglia were simultaneously isolated from embryo brains at E14.5 using the EMBRACE methodology<sup>38</sup>. Briefly, the brains were acutely isolated from embryos at E14.5 and meninges removed. The samples were incubated in digestion solution (0.13 WU  $\text{ml}^{-1}$  Liberase TM (Worthington, Roche, 0540119001), 80 U  $\text{ml}^{-1}$  DNase I (NEB) and 5 mM  $\text{MgCl}_2$  in PBS) and incubated at 37 °C in a thermoshaker set at 800 r.p.m. After 20 min, brains were triturated using a P1000 pipette and incubated for a further 20 min. The cells were passed through a 100- $\mu$ m sieve, washed once in PBS and incubated with the PDGFR $\beta$  antibody (Supplementary Table 4) diluted in FACS buffer (2% FCS in PBS) for 30 min on ice. After two washes in 1 ml FACS buffer, the cells were resuspended in 400  $\mu$ l antibody mix (CD102, PECAM1, CD41, CD45, CD11b and Alexa Fluor 488 anti-goat IgG antibodies; Supplementary Table 4) diluted in FACS buffer. Zombie dye (1:200; Biolegend, 423106) was added as a viability marker. The cells were incubated on ice for 60 min, washed twice in PBS and resuspended in 1 ml FACS buffer. The cells were passed through a 100- $\mu$ m sieve before FACS. All FACS was carried out on a FACS Aria (BD) and analyses on a BD Fortessa. Analyses were undertaken using the FlowJo software v9.8.1 and v10.

**Quantification of red blood cells in E14.5 brains.** Brains were dissociated as described above. Cells were incubated in 400  $\mu$ l FACS buffer with antibodies raised against CD11b, CD45 and Ter-119 (Supplementary Table 4). Zombie dye (1:200; Biolegend, 423106) was used as a viability marker. The cells were incubated for 60 min on ice, washed three times in FACS buffer and analysed on a BD Fortessa instrument. The number of Ter-119<sup>+</sup>CD11b<sup>-</sup> cells were quantified using the FlowJo (v10) software.

**RNA-seq. E14.5 brains.** Brains were dissected from embryos at E14.5, the meninges were removed and the brains snap frozen. RNA was extracted using a RNeasy mini kit (Qiagen, 74104). Libraries were prepared for sequencing using the Illumina ribo-depletion gold kit and sequenced on a NextSeq 500 instrument. Around  $45 \times 10^6$  reads were obtained for each sample and mapped to the GRCm38 (mm10) genome assembly using HISAT2 (v2.0.0). Fragments were counted at the gene level using featureCounts (v1.5.0). Differential-expression analysis was performed using edgeR (v3.14). Genes were considered differentially expressed with an FDR cut-off of 0.05 and  $\log_2[\text{fold change}] \geq 0.5$ . The raw data from these experiments have been uploaded to the Gene Expression Omnibus (GEO) and are available under the accession number GSE138981.

**Pericytes and neural, endothelial and microglial cells.** Neural cells, pericytes, endothelial cells and microglia were isolated from brains at E14.5 as described earlier using the FACS-based EMBRACE methodology (Extended Data Fig. 3a). For each biological replicate, cells from a single brain at E14.5 were used. The cells were sorted into ice-cold PBS supplemented with 2% FCS, collected by centrifugation (300g, 5 min, 4 °C) and the pellets were snap frozen and stored at -80 °C. To ensure consistency, RNA extraction and library preparation were

performed simultaneously for all samples from a given cell type. RNA from neural cells was extracted using a RNeasy mini kit (Qiagen, 74104), and from pericytes, endothelial cells and microglia using a miRNAeasy micro kit (Qiagen). The RNA quality was checked using a Bioanalyzer (Agilent). Complementary DNA (cDNA) was prepared from the isolated RNA using a SMART-seq v4 ultra low input RNA kit for sequencing (Clontech, 634891). Thereafter, libraries were prepared using a Nextera XT DNA library preparation kit (Illumina, FC-131-1096) and sequenced on the HiSeq 3000 or NextSeq 500 instrument. Reads were trimmed and mapped to the GRCm38 (mm10) genome assembly using STAR<sup>63</sup>. The reads were identified using FeatureCount<sup>64</sup>. Genes that were differentially expressed were identified using DESeq2 (ref. <sup>65</sup>) with an FDR cut-off of 0.05. The raw data from these experiments have been uploaded to the GEO and are available under the accession number GSE138981. KEGG pathway and Gene-Ontology-term analyses were carried out using DAVID<sup>66</sup>. The RNA-seq data were compared with the previously published comprehensive MOF, KANSL3 and MCRS1 ChIP-seq datasets (GSE51746)<sup>25</sup>. Differences in preferential binding of MOF and KANSL3 to genes downregulated in *Mof*-nKO neural cells were determined using a two-sided Wilcoxon rank-sum test. Ingenuity pathway analysis (Qiagen) was used to investigate the networks and pathways dysregulated in the pericytes, endothelial cells and microglia isolated from *Mof*-nKO, *Kansl2*-nKO and *Kansl3*-nKO brains. Heatmaps were generated using the gplots Heatmap.2 package in R.

**Fatty-acid-treated brain pericytes.** Wild-type brain pericytes were extracted from adult brains as described above. Long-chain fatty acids were conjugated for 2 h with fatty acid-free BSA (11% wt/vol in PBS). At passage 10, pericytes were treated overnight (16 h) with a cocktail of LCFAs (200  $\mu$ M C14:0, 200  $\mu$ M C16:0, 20  $\mu$ M C20:0 and 10  $\mu$ M C24:0) as well as a vehicle control. The cells were rinsed twice in PBS and RNA was extracted using a RNeasy mini kit (Qiagen, 74104). RNA was quantified using a Bioanalyzer (Agilent) and sequenced on a HiSeq 3000 instrument. Around  $60 \times 10^6$  reads were obtained per sample. Reads were trimmed for adaptors using TrimGalore (v0.4.4) and mapped to the GRCm38 (mm10) genome assembly using STAR (v2.5.3a). Fragments were counted using featureCounts (v1.5.2) and differential expression was performed using DESeq2 (v1.14.1). Quality checks were performed using deepTools (v3.0.2) and multiQC (v1.2). Differentially expressed genes were used for subsequent analysis with a cut-off of FDR < 0.05, a fold change  $\geq 0.5$  and base-mean > 50. The raw data from these experiments have been uploaded to the GEO and are available under the accession number GSE138981. Analyses of activated networks were performed using the Ingenuity (Qiagen) analysis.

**H4K16ac and panH3 ChIP.** Neural cells were isolated from *Mof*-nKO and *Nes-Cre<sup>+/+</sup>* control brains at E14.5 using the EMBRACE methodology by gating on PDGFR $\beta$ -PECAM1-CD102-CD45-CD41-CD11b<sup>-</sup>zombie-dye<sup>-</sup> cells. After FACS, the cells were collected by centrifugation (5 min, 300g, 4 °C), crosslinked in 1% paraformaldehyde (diluted in DMEM with 10% FCS), quenched with 0.125 M glycine, washed twice in PBS with protein inhibitors and frozen at -80 °C. Nuclei were extracted, counted and processed for ChIP using antibodies raised against H4K16ac and histone H3 using the RELACS protocol<sup>67</sup>. One microgram of antibody was used for each immunoprecipitation (Supplementary Table 4). Enrichment of H4K16ac in *Nes-Cre<sup>+/+</sup>* controls over *Mof*-nKO was determined using a two-sided Wilcoxon rank-sum test with the deepStats R package. The raw data are available under the accession number GSE138981.

**scRNA-seq analysis.** Single-cell RNA-seq was carried out using the CEL-Seq2 protocol as previously described<sup>68</sup>. Briefly, single cells were sorted via FACS into individual wells of a 384-well plate containing 240 nl primer mix and 1.2  $\mu$ l mineral oil. The 384-well plates were centrifuged at 2,200g (10 min, 4 °C) and stored at -80 °C. RNA from each cell was reverse transcribed using a 160 nl reverse transcription reaction and 2.2  $\mu$ l second-strand reaction mix. The prepared cDNA was pooled from 96-wells into a single tube (a total of 4 tubes per 384-well plate). The samples were cleaned and in vitro transcribed, and libraries were generated for sequencing. The libraries were sequenced on an Illumina HiSeq 3000 platform at a depth of approximately 200,000 reads per cell. Sequencing data were mapped to the mm10 mouse reference genome using bwa (v0.6.2-r126). Cells expressing at least 1,500 transcripts and the endothelial cell marker *Flt1* were selected. A total of 401 endothelial cells were analysed. For the zonation analysis, diffusion pseudotime (dpt)<sup>69</sup> was implemented and diffusion maps were generated using the destiny R package. The number of nearest neighbours, *k*, was set to 100. Self-organising maps (SOMs) were generated using the FateID package<sup>68</sup> on the basis of the ordering computed by dpt as input. Only genes with > 3 counts after size normalization in at least a single cell were included for the SOM analysis. Smooth zonation profiles were derived by applying local regression on normalized transcript counts after ordering cells by dpt. Next, a one-dimensional SOM with 200 nodes was computed on these profiles after z-transformation. Neighbouring nodes were merged if the Pearson's correlation coefficient of the average profiles of these nodes exceeded 0.85. The remaining aggregated nodes represent the gene modules shown in the SOM figures. To determine whether there was a significant enrichment of *Mof*-nKO or WT cells across parts of the zonation axis, a Fisher's exact test was performed on each of the four quadrants of the pseudo-temporally ordered cells.

Data from the scRNA-seq analyses have been uploaded to the GEO under the accession number [GSE133079](https://www.ncbi.nlm.nih.gov/geo/query/acc.cgi?acc=GSE133079).

**Identification of PDGFR $\beta$ -high mural cells.** To determine the ratio of pericytes:smooth muscle cells in the FACS-isolated PDGFR $\beta$ -high mural cell population, scRNA-seq analyses of EMBRACE-isolated PDGFR $\beta$ -high cells<sup>38</sup> from WT brains at E14.5 were carried out. The identity of pericytes and smooth muscle cells was determined using previously identified markers<sup>70</sup> and overlaid with data from the scRNA-seq EMBRACE analyses. These data are available under the accession number [GSE133079](https://www.ncbi.nlm.nih.gov/geo/query/acc.cgi?acc=GSE133079). Approximately 96% ( $n = 340$  of 354) of mural cells were found to be pericytes and about 4% ( $n = 14$  of 354) displayed a smooth muscle cell identity.

**Quantification of DNA recombination.** To quantify recombination of *Mof*, *Kansl2* and *Kansl3* alleles, quantitative DNA PCRs were carried out. The floxed and deleted alleles were quantified using SYBR green chemistry (SensiMix, Bioline, QT605). Data were standardized to WT DNA loci. DNA isolated from WT and knockout animals were used as positive and negative controls, respectively. The genotyping primers provided in Supplementary Table 1 were used.

**Molecular biology.** For quantitative reverse-transcription PCR analyses, RNA was extracted from whole brains or neural cells using a RNeasy mini kit (Qiagen, 74106). For endothelial cells, pericytes and microglia, RNA was extracted using a miRNAeasy micro kit (Qiagen). Reverse transcription reactions were carried out using the Superscript III first strand synthesis system (Thermo Fischer, 18080-051) as per the manufacturer's instructions. The transcript levels were quantified using SYBR green chemistry on an LC480 instrument (Roche). The primer sequences are provided in Supplementary Table 2. Data were standardized to housekeeping genes as defined in the figure legends.

Cell fractionation was undertaken using a Subcellular protein fractionation kit for cultured cells (Thermo Scientific, 78840) as per the manufacturer's instructions.

Immunoprecipitation assays were carried out on endogenous E14.5 brain lysates prepared in HMG150 buffer (25 nM HEPES pH 7.6, 12.5 mM MgCl<sub>2</sub>, 10% glycerol, 150 mM KCl, 0.5% Tween-20 and Protease inhibitor complete mini (Roche, 04693159001)). A 50:50 combination of Sepharose protein A and protein G beads (GE Healthcare, 17-5280-02 and 17-0618-05), blocked with 0.2 mg ml<sup>-1</sup> BSA, was used to pre-clear the brain lysates. Each immunoprecipitation was performed on 300  $\mu$ g protein with 3  $\mu$ g MOF (Abcam), KANSL1, KANSL2, KANSL3, MCERS1 or MSL3 antibodies (Supplementary Table 4) or 3  $\mu$ g rabbit IgG (Abcam, ab172730) overnight at 4 °C. Following the immunoprecipitation, 100  $\mu$ l of blocked protein A/G beads were added, incubated for 1 h at 4 °C, washed three times in HMG150 (10 min each), eluted in ROTI-load (Roth, K929.1) and used for western blot analysis.

Western blot analyses were performed using standard methods. Briefly, 20  $\mu$ g whole-cell lysates or 5  $\mu$ g cellular fractions were run on a 4–12% gradient gel (Thermo Fischer) and proteins were transferred to a PVDF membrane (Roche, 03010040001). The membrane was blocked in 5% skim milk and incubated overnight with the appropriate primary antibody (Supplementary Table 4). After washing, the membrane was incubated with the appropriate secondary horseradish peroxidase (HRP)-conjugated antibody (anti-rabbit HRP (GE Healthcare, NA934) and anti-goat HRP (Santa Cruz, sc2354)) and developed using the Lumi-Light reagent (Roche, 12015200001) with detection of chemiluminescence on a Bio-Rad Chemidoc XRS+ instrument. Quantification and image analyses were carried out using the Image Lab software (v5.2, Bio-Rad Laboratories).

**MOF lentivirus expression.** Wild-type FLAG-tagged MOF as well as a catalytically inactive FLAG-tagged E350Q MOF were cloned into the pCHDblast MCSNard plasmid (Addgene vector no. 22661) using the BamHI and XhoI cloning sites. The 'negative vector' contained a 22 bp fragment inserted into the same vector but lacked an open reading frame. This vector contains a CMV promoter and a blasticidin selection marker. Lentivirus was produced as previously described<sup>25</sup> and MEFs were infected 1 d after treatment with tamoxifen. Cell selection was carried out over 4 d using 5  $\mu$ g ml<sup>-1</sup> blasticidin. Total fatty acid extraction and western blot analyses were carried out as described earlier.

**Ethics statement for assays using human brain samples.** Autopsies were obtained from 29-week-old fetuses and processed for histology. Signed consent forms were obtained from the parents. Ethics approval was obtained from Université Grenoble-Alpes CHU Grenoble and University of Freiburg, Germany.

**Statistics and reproducibility.** Categorical data such as genotypes are presented in absolute numbers and were analysed using a  $\chi^2$  or Fischer's exact test as indicated in the figure legends. Sequencing data and MS-based metabolomics data are generally presented on a log<sub>2</sub> scale as this better represents the large spread of the data. All other numerical data are presented as the mean  $\pm$  s.e.m. and were analysed using a two-sided Student's *t*-test. The statistical test compared the marked genotype (or group) with the appropriate *Nes-Cre*<sup>+/+</sup> or WT controls. The number of times the experiment was repeated has been indicated in the figure legends. In all instances, the repeat experiments displayed similar results.

**Reporting Summary.** Further information on research design is available in the Nature Research Reporting Summary linked to this article.

## Data availability

All sequencing data from this study have been uploaded to the NCBI GEO database. Raw data pertaining to RNA-seq experiments are deposited under the accession number [GSE138981](https://www.ncbi.nlm.nih.gov/geo/query/acc.cgi?acc=GSE138981), scRNA-seq data under [GSE133079](https://www.ncbi.nlm.nih.gov/geo/query/acc.cgi?acc=GSE133079), and H4K16ac and histone H3 ChIP-seq data under [GSE138981](https://www.ncbi.nlm.nih.gov/geo/query/acc.cgi?acc=GSE138981). Previously published MOF, KANSL3 and MCERS1 ChIP-seq profiles used in this study are deposited under [GSE51746](https://www.ncbi.nlm.nih.gov/geo/query/acc.cgi?acc=GSE51746). Identity of genes specifically enriched in different E14.5 brain cell populations were derived from: <http://betsholtzlab.org/VascularSingleCells/database.html> and <https://mpi-ie.shinyapps.io/braininteractomeexplorer>. All other data supporting the findings of this study are available from the corresponding author on reasonable request.

## References

- Tronche, F. et al. Disruption of the glucocorticoid receptor gene in the nervous system results in reduced anxiety. *Nat. Genet.* **23**, 99–103 (1999).
- Zimmerman, L. et al. Independent regulatory elements in the nestin gene direct transgene expression to neural stem cells or muscle precursors. *Neuron* **12**, 11–24 (1994).
- Proctor, J. M., Zang, K., Wang, D., Wang, R. & Reichardt, L. F. Vascular development of the brain requires  $\beta 8$  integrin expression in the neuroepithelium. *J. Neurosci.* **25**, 9940–9948 (2005).
- Graus-Porta, D. et al.  $\beta 1$ -class integrins regulate the development of laminae and folia in the cerebral and cerebellar cortex. *Neuron* **31**, 367–379 (2001).
- Braun, T. P. et al. Expression of myeloid differentiation factor 88 in neurons is not requisite for the induction of sickness behavior by interleukin-1 $\beta$ . *J. Neuroinflammation* **9**, 229 (2012).
- Sheikh, B. N. et al. MOZ (MYST3, KAT6A) inhibits senescence via the INK4A–ARF pathway. *Oncogene* **34**, 5807–5820 (2015).
- Tigges, U., Welsch-Alves, J. V., Boroujerdi, A. & Milner, R. A novel and simple method for culturing pericytes from mouse brain. *Microvascular Res.* **84**, 74–80 (2012).
- Yang, B. et al. Single-cell phenotyping within transparent intact tissue through whole-body clearing. *Cell* **158**, 945–958 (2014).
- Chatterjee, A. et al. MOF acetyl transferase regulates transcription and respiration in mitochondria. *Cell* **167**, 722–738 (2016).
- Dobin, A. et al. STAR: ultrafast universal RNA-seq aligner. *Bioinformatics* **29**, 15–21 (2013).
- Liao, Y., Smyth, G. K. & Shi, W. featureCounts: an efficient general purpose program for assigning sequence reads to genomic features. *Bioinformatics* **30**, 923–930 (2014).
- Love, M. I., Huber, W. & Anders, S. Moderated estimation of fold change and dispersion for RNA-seq data with DESeq2. *Genome Biol.* **15**, 550 (2014).
- Huang da, W., Sherman, B. T. & Lempicki, R. A. Systematic and integrative analysis of large gene lists using DAVID bioinformatics resources. *Nat. Protoc.* **4**, 44–57 (2009).
- Arrighoni, L. et al. RELACS nuclei barcoding enables high-throughput ChIP-seq. *Commun. Biol.* **1**, 214 (2018).
- Herman, J. S., Sagar & Grün, D. FateID infers cell fate bias in multipotent progenitors from single-cell RNA-seq data. *Nat. Methods* **15**, 379–386 (2018).
- Haghverdi, L., Buttner, M., Wolf, F. A., Büttner, F. & Theis, F. J. Diffusion pseudotime robustly reconstructs lineage branching. *Nat. Methods* **13**, 845–848 (2016).
- He, L. et al. Analysis of the brain mural cell transcriptome. *Sci. Rep.* **6**, 35108 (2016).

## Acknowledgements

We thank the Core Imaging facility (IMCF, University of Basel) and in particular W. Heusermann for technical assistance provided on the SPIM light-sheet microscope. We thank B. Joch, K. Seidel, H. Al-Hasani and J. Seyffert for technical assistance, as well as T. Vogel, S. Weise (University of Freiburg), R. Adams, H. W. Jeong and E. Watson (MPI for Molecular Biomedicine, Münster) for their helpful discussions. We thank M. Shvedunova for help with writing and editing the manuscript. B.N.S. was funded by an Alexander von Humboldt fellowship. This work was supported by the CRC 992 and CRC 1381 awarded to A.A. and by the German Research Foundation (DFG) under Germany's Excellence Strategy (CIBSS, EXC-2189, project ID 390939984).

## Author contributions

B.N.S. and A.A. conceived and initiated the project. B.N.S., S.G., T.H.T., M.S., B.H., H.H., T.S., N.A., O.M., O.K., W.R., A.C., L.J.B., D.v.E. and J.M.B. planned and carried out experiments. B.N.S., G.R., V.B., O.B., N.A. and J.M.B. carried out the bioinformatics analyses. J.T. and H.S. diagnosed, genetically tested and provided brain biopsies of patients with KdV. B.N.S., S.G., T.H.T., M.S., G.R., V.B., S.A., J.M.B. and A.A. analysed

data and interpreted the results. B.N.S., T.B., T.B.H., D.G., D.V., M.P. and A.A. supervised the project. B.N.S. and A.A. wrote the manuscript. All authors corrected and approved the manuscript.

### Competing interests

The authors declare no competing interests.

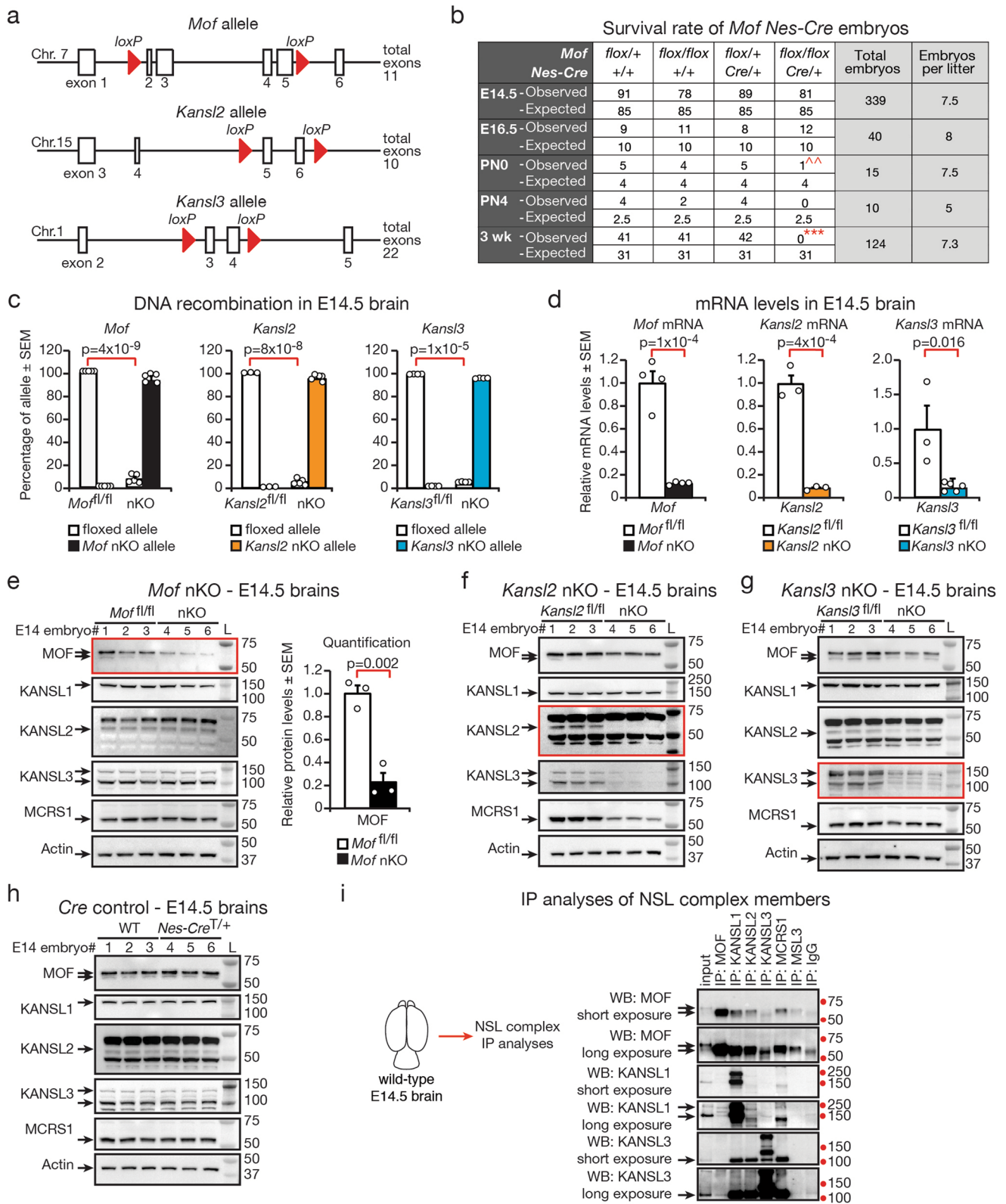
### Additional information

**Extended data** is available for this paper at <https://doi.org/10.1038/s41556-020-0526-8>.

**Supplementary information** is available for this paper at <https://doi.org/10.1038/s41556-020-0526-8>.

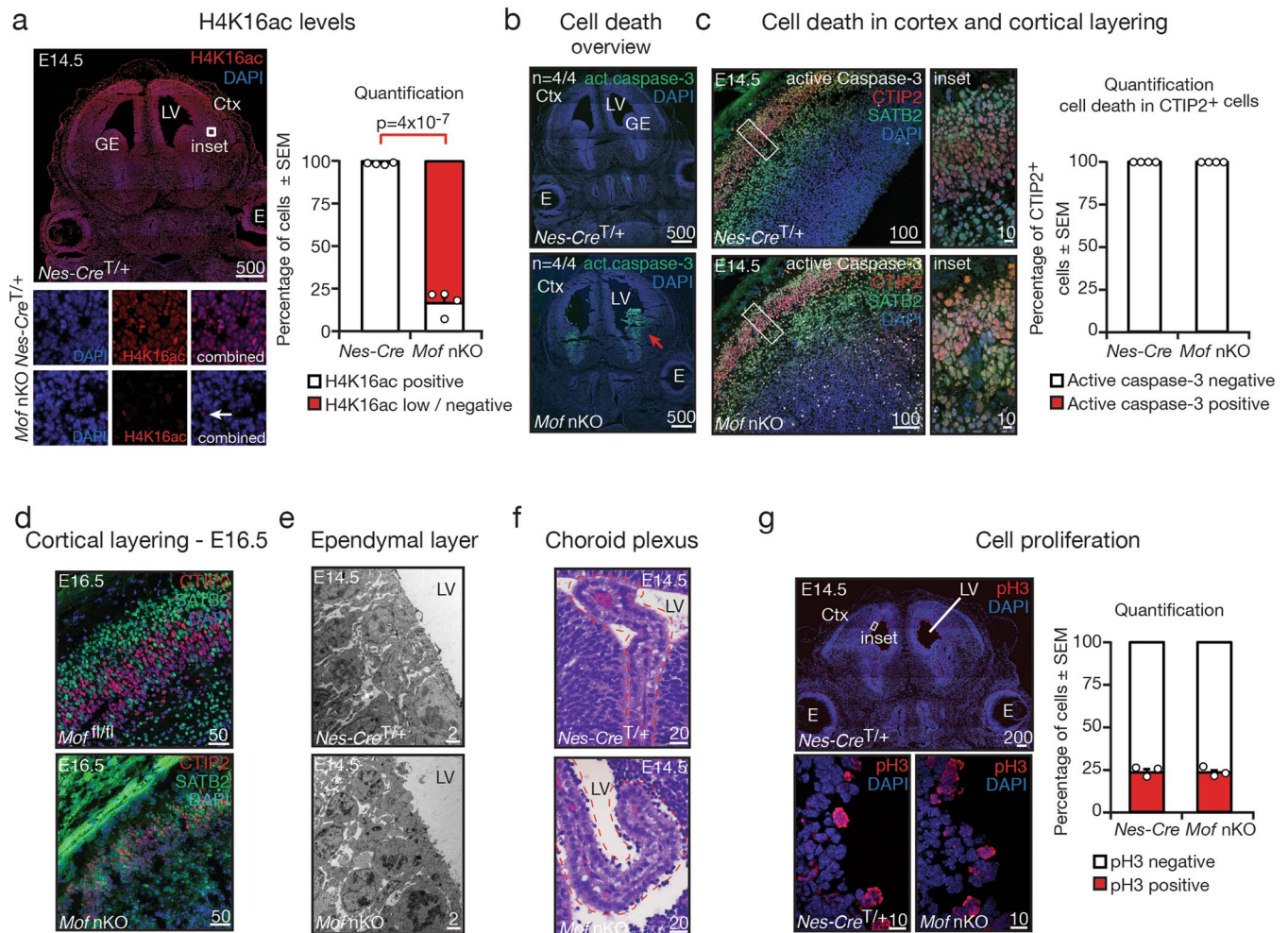
**Correspondence and requests for materials** should be addressed to A.A.

**Reprints and permissions information** is available at [www.nature.com/reprints](http://www.nature.com/reprints).

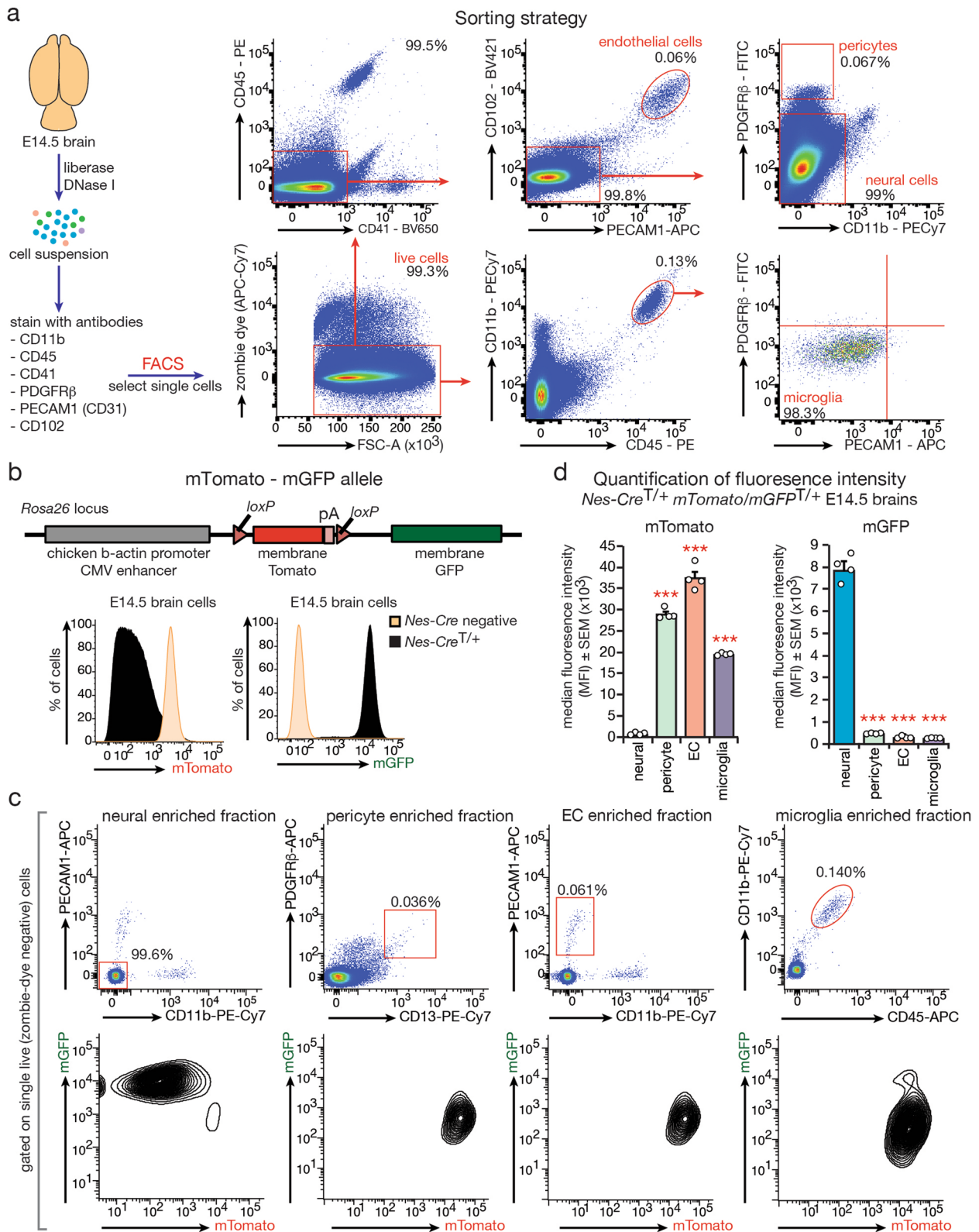


Extended Data Fig. 1 | See next page for caption.

**Extended Data Fig. 1 | Nes-Cre depletes the NSL complex from the E14.5 brain.** **a**, Diagrams depicting the floxed *Mof*, *Kansl2* and *Kansl3* alleles. **b**, Survival of progeny from a *Mof*<sup>fl/+</sup> *Nes-Cre*<sup>+/+</sup> × *Mof*<sup>fl/fl</sup> cross. *Mof*-nKO animals were found at Mendelian ratios before birth, but none survived until weaning. \*\*\* $p=5 \times 10^{-9}$  ( $\chi^2$  test). ^ denotes dead embryo. **c**, Quantification of *Mof*, *Kansl2* and *Kansl3* allele recombination in E14.5 brains. Knockout and floxed alleles were quantified using quantitative genomic PCR.  $n = 5$  *Mof*-nKO, 5 *Mof*<sup>fl/fl</sup>; 5 *Kansl2*-nKO, 3 *Kansl2*<sup>fl/fl</sup>; 4 *Kansl3*-nKO, 4 *Kansl3*<sup>fl/fl</sup> embryos. **d**, *Mof*, *Kansl2* and *Kansl3* mRNA levels in E14.5 nKO brains.  $n = 4$  *Mof*-nKO, 4 *Mof*<sup>fl/fl</sup>; 3 *Kansl2*-nKO, 3 *Kansl2*<sup>fl/fl</sup>; 5 *Kansl3*-nKO, 3 *Kansl3*<sup>fl/fl</sup> embryos. **e**, Protein expression of NSL complex members in E14.5 *Mof*-nKO brains. MOF protein was strongly reduced (quantification provided), but other NSL complex members were unchanged.  $n = 3$  embryos per genotype. **f**, Expression of NSL complex members in *Kansl2*-nKO brains. KANSL2 protein was depleted and reduced levels of MCRS1, KANSL3 and MOF were observed.  $n = 3$  embryos per genotype. **g**, Expression of NSL complex members in E14.5 *Kansl3*-nKO brains. KANSL3 protein was depleted, while MOF showed a mild reduction.  $n = 3$  embryos per genotype. **h**, Levels of NSL complex members in WT versus *Nes-Cre*<sup>+/+</sup> E14.5 brains. *Nes-Cre* alone did not affect the levels of NSL complex members.  $n = 3$  brains per genotype. **i**, Immunoprecipitation (IP) with antibodies raised against NSL complex members MOF, KANSL1, KANSL2, KANSL3 and MCRS1 as well as MSL complex member MSL3 were carried out, followed by Western blot analyses for MOF, KANSL1 and KANSL3. The experiment was repeated 3 times. Data in panels **c**, **d** and **e** are presented as mean  $\pm$  s.e.m. and were analysed using a two-tailed Student's *t*-test. L indicates ladder. Statistical source data and unprocessed blots are shown in Source Data Extended Data Fig. 1.

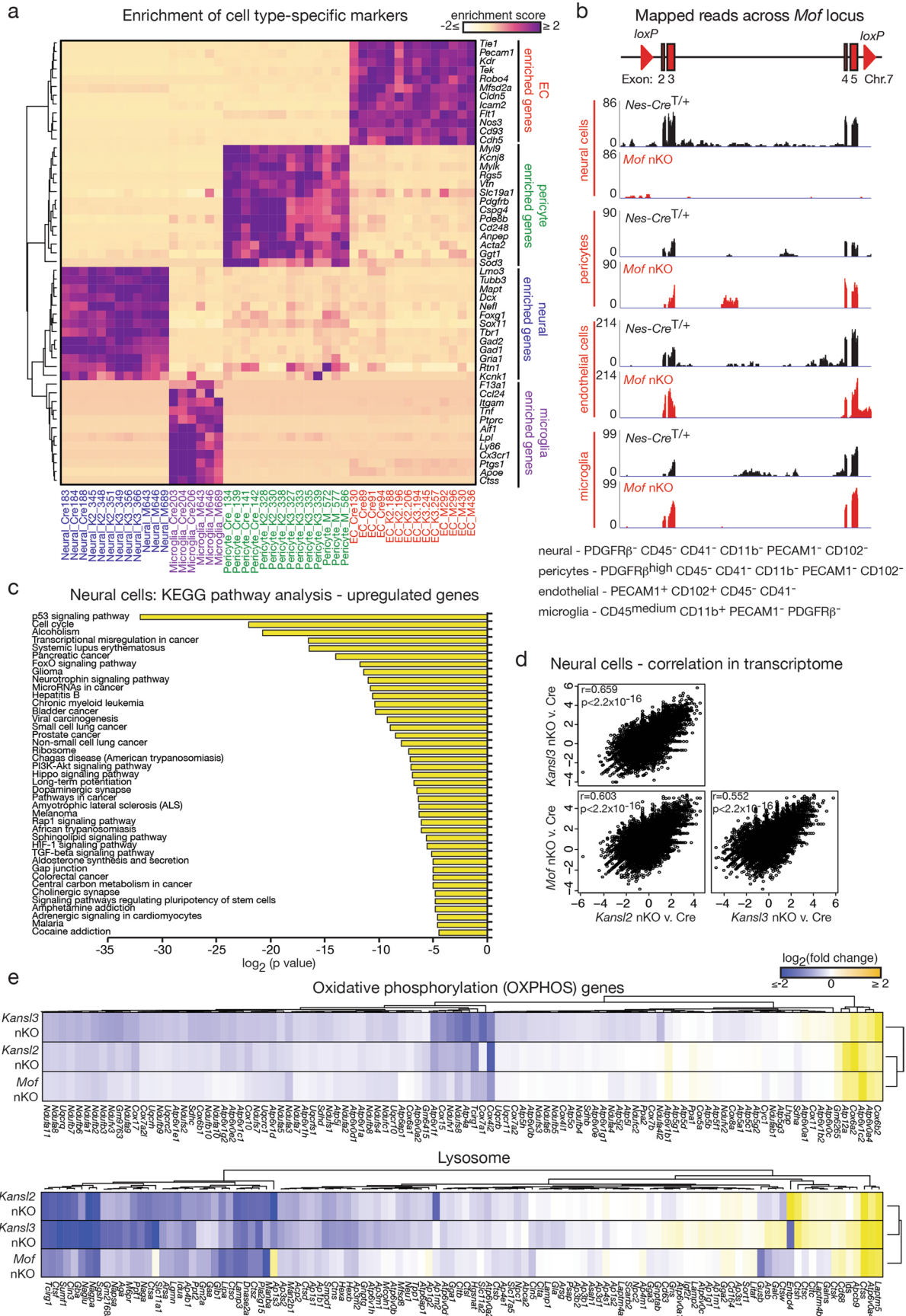


**Extended Data Fig. 2 | *Mof*-nKO causes disruption of the ganglionic eminence.** **a**, Quantification of H4K16ac using immunofluorescence. Left panel: Representative H4K16ac staining in the E14.5 brain. Area indicated by the white box was quantified in *Mof*-nKO and *Nes-Cre*<sup>T/+</sup> brains. The white arrow signifies the occasional H4K16ac-positive cells in *Mof*-nKO. Right panel: enumeration of H4K16ac-positive cells.  $n = 4$  animals per genotype, with 388 to 871 cells counted per sample. **b**, Activated caspase-3 staining showing extensive cell death in the ganglionic eminence region of the E14.5 *Mof*-nKO brain (marked by red arrow). 4 embryos per genotype were analysed. **c**, Staining of the E14.5 cortex with neuronal markers CTIP2 and SATB2 and cell death marker activated caspase-3. White squares represent the area from which the inset images are derived. Right panel: Quantification of activated caspase-3 and CTIP2 double positive cells.  $n = 4$  animals per genotype, with 1310 CTIP2<sup>+</sup> cells analysed from *Mof*-nKO, and 1597 from *Nes-Cre*<sup>T/+</sup> animals. **d**, Immunostaining of E16.5 *Mof*-nKO cortices for neuronal markers CTIP2 and SATB2. **e**, Transmission electron microscope (TEM) images of the ventricular zone lining the lateral ventricle at E14.5. **f**, Histological analysis of the choroid plexus. The choroid plexus is indicated with the red dotted line. 3 animals per genotype were analysed in **d-f**. **g**, Quantification of cell proliferation via phospho-histone H3 (pH3) staining in the ventricular zone. Positive cells were counted in the first three cell layers adjacent to the lateral ventricle.  $n = 3$  animals per genotype; 1931 *Mof*-nKO, 937 *Nes-Cre*<sup>T/+</sup> cells analysed. Data in panels **a**, **c** and **g** are presented as mean  $\pm$  s.e.m. and were analysed using a two-tailed Student's *t*-test. Ctx - cortex, E - eye, GE - ganglionic eminence, LV - lateral ventricle. All scale bars are provided in  $\mu$ m. Statistical source data are shown in Source Data Extended Data Fig. 2.



Extended Data Fig. 3 | See next page for caption.

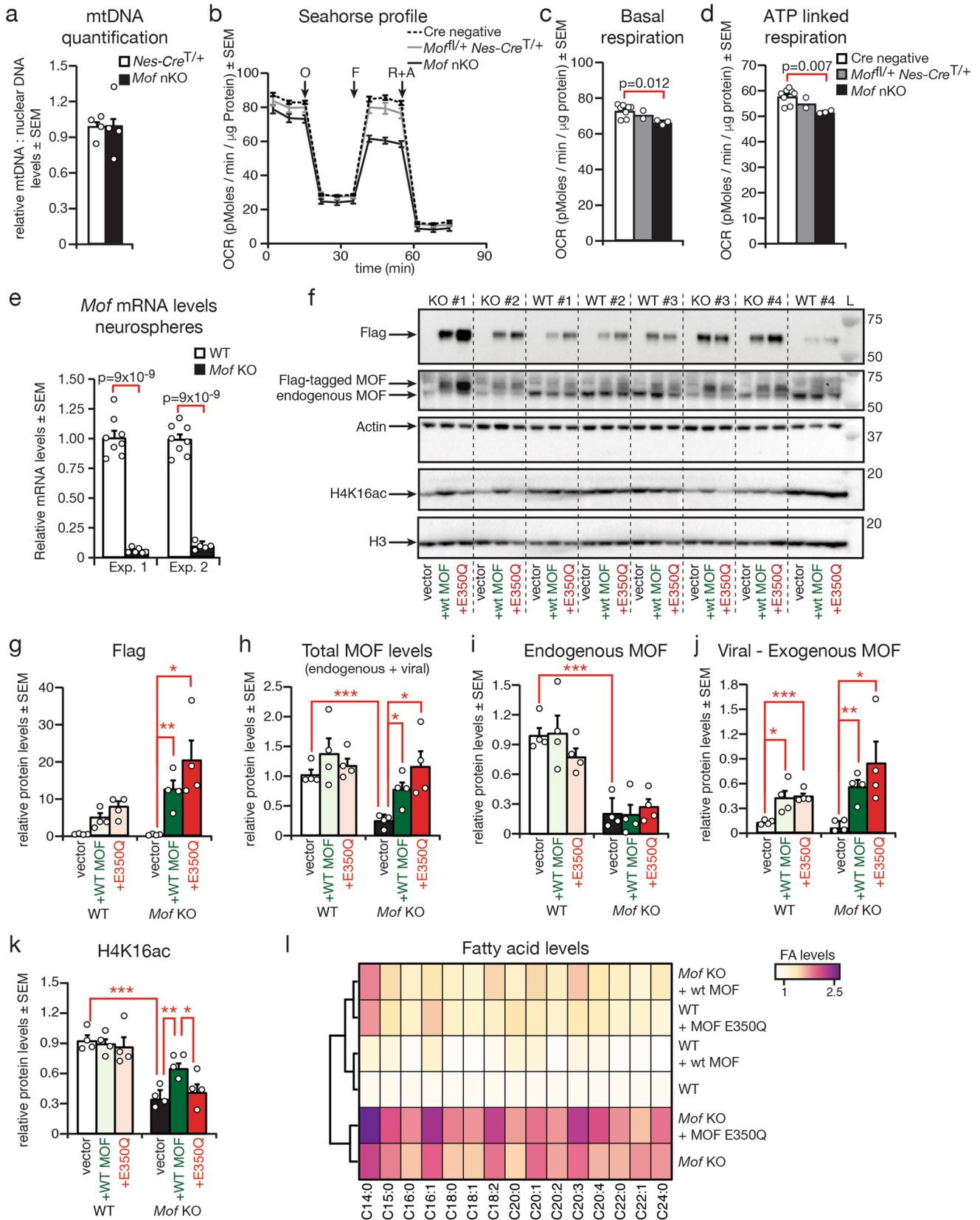
**Extended Data Fig. 3 | Nes-Cre is specifically active in neural cells.** **a**, EMBRACE<sup>38</sup> sorting strategy for the simultaneous isolation of cell populations enriched for neural cells (CD11b<sup>-</sup>, CD45<sup>-</sup>, CD41<sup>-</sup>, PDGFRβ<sup>-</sup>, PECAM1<sup>-</sup>, CD102<sup>-</sup>), pericytes (PDGFRβ<sup>high</sup>, CD11b<sup>-</sup>, CD45<sup>-</sup>, CD41<sup>-</sup>, PECAM1<sup>-</sup>, CD102<sup>-</sup>), endothelial cells (PECAM1<sup>+</sup>, CD102<sup>+</sup>, CD45<sup>-</sup>, CD41<sup>-</sup>) and microglia (CD11b<sup>+</sup>, CD45<sup>medium</sup>, PDGFRβ<sup>-</sup>, PECAM1<sup>-</sup>) from the E14.5 brain. **b**, Diagrammatic depiction of the *mTomato-mGFP* allele. Membrane-targeted (m) Tomato is expressed ubiquitously but is flanked by *loxP* sites. Following Cre-mediated recombination, *mTomato* is spliced out and *mGFP* expression activated. The histograms show mTomato and mGFP expression in E14.5 brain cells in the presence and absence of the *Nes-Cre*. As expected, *Nes-Cre*-mediated recombination results in lower levels of mTomato and activation of mGFP expression. 4 *mT/mG<sup>V+</sup> Nes-Cre<sup>V+</sup>* E14.5 embryos were analysed. **c**, Exemplary FACS plots showing mTomato and mGFP expression in populations enriched for neural cells (PECAM1<sup>-</sup>, CD11b<sup>-</sup>), pericytes (PDGFRβ<sup>high</sup>, CD13<sup>high</sup>), endothelial cells (EC, PECAM1<sup>+</sup> CD11b<sup>-</sup>) and microglia (CD11b<sup>+</sup> CD45<sup>medium</sup>). 4 *mT/mG<sup>V+</sup> Nes-Cre<sup>V+</sup>* E14.5 embryos were analysed. **d**, Quantification (median fluorescence intensity) of mTomato and mGFP expression in cell populations enriched for neural, pericytes, endothelial and microglial cells by flow cytometry. Increased mGFP expression and loss of mTomato expression was observed in neural cells. Only high mTomato expression was evident in the pericyte, endothelial and microglia enriched fractions. n = 4 *mT/mG<sup>V+</sup> Nes-Cre<sup>V+</sup>* E14.5 embryos. Data are presented as mean ± s.e.m. Data were analysed using a two-tailed Student's t-test via pair-wise comparisons of neural cells with each of the other cell populations. Asterisks signify statistical significance at \*\*\**p* < 0.001. Precise *p*-values of all comparisons and statistical source data are shown in Source Data Extended Data Fig. 3.



Extended Data Fig. 4 | See next page for caption.

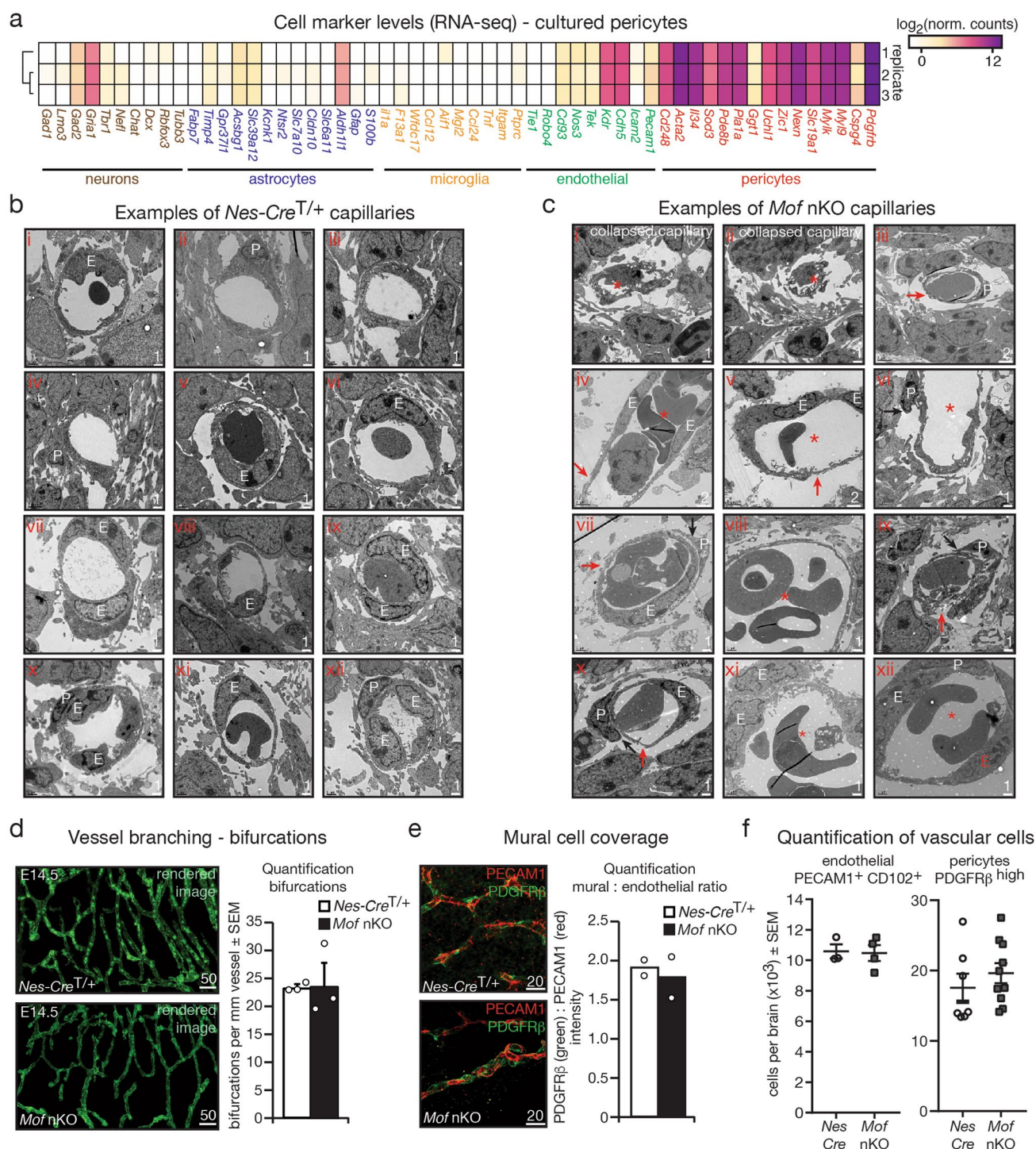
71. Vanlandewijck, M. et al. A molecular atlas of cell types and zonation in the brain vasculature. *Nature* 554, 475–480 (2018).

**Extended Data Fig. 4 | Neural deletion of the NSL complex causes metabolic changes.** **a**, Enrichment of marker genes in neural cells, pericytes, endothelial cells and microglia in cell populations isolated using the EMBRACE methodology. The enrichment score was calculated using standardized counts from the DESeq2 output with the formula  $[(C - \text{average}[C])/sd]$ . C represents the standardized read counts in the given cell population. Average[C] is the average counts of the gene across all four cell populations. sd is the standard deviation. The list of enriched genes for each population was extracted from <http://betsholtzlab.org/VascularSingleCells/database.html><sup>71</sup> and <https://mpi-ie.shinyapps.io/braininteractomeexplorer><sup>38</sup>. Number of animals analysed: Neural cells, 3 per genotype; pericytes, 4 *Nes-Cre*<sup>+/+</sup>, 3 *Mof*-nKO, 3 *Kansl2*-nKO, 4 *Kansl3*-nKO; endothelial cells (EC), 4 *Nes-Cre*<sup>+/+</sup>, 4 *Mof*-nKO, 3 *Kansl2*-nKO, 3 *Kansl3*-nKO; microglia 3 per genotype. **b**, IGV profiles showing reads mapped via RNA-seq across the *Mof* locus. No reads were detected between the *loxP* sites in neural cells from *Mof*-nKO brains, where the *Nes-Cre* is active. In contrast, reads across the *Mof* locus in pericytes, endothelial cells and microglia isolated from *Mof*-nKO brains were unchanged compared to *Nes-Cre*<sup>+/+</sup> controls. Number of animals analysed: Neural cells, 3 per genotype; pericytes, 4 *Nes-Cre*<sup>+/+</sup>, 3 *Mof*-nKO; endothelial cells (EC), 4 per genotype; microglia, 3 per genotype. **c**, KEGG pathways significantly enriched amongst genes upregulated in *Mof*-nKO neural cells. Data are presented on a log<sub>2</sub> scale. n = 3 brains per genotype. Data were analysed using a Fisher exact test via the DAVID platform<sup>66</sup>. **d**, Correlation plots for gene expression changes in *Mof*-nKO, *Kansl2*-nKO and *Kansl3*-nKO neural cells. Gene expression changes in the presented comparisons were used to calculate the Pearson's coefficient (r). n = 3 brains per genotype. **e**, Heatmaps showing the downregulation of OXPHOS and lysosome pathway genes in *Mof*-nKO, *Kansl2*-nKO and *Kansl3*-nKO neural cells. The gene lists were downloaded from the KEGG pathway database and converted to the corresponding mouse genes. n = 3 animals per genotype. Statistical source data are shown in Source Data Extended Data Fig. 4.

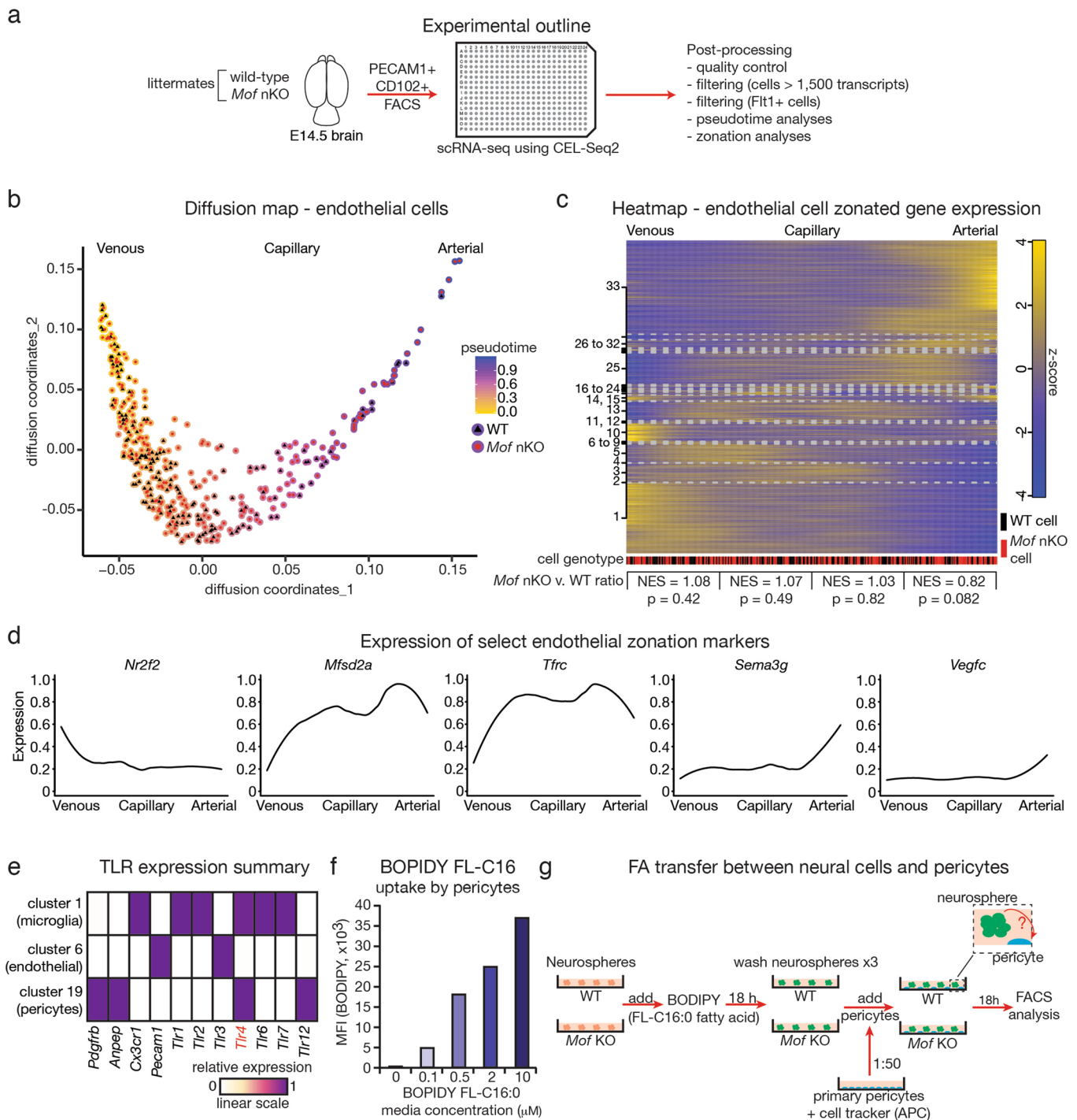


Extended Data Fig. 5 | See next page for caption.

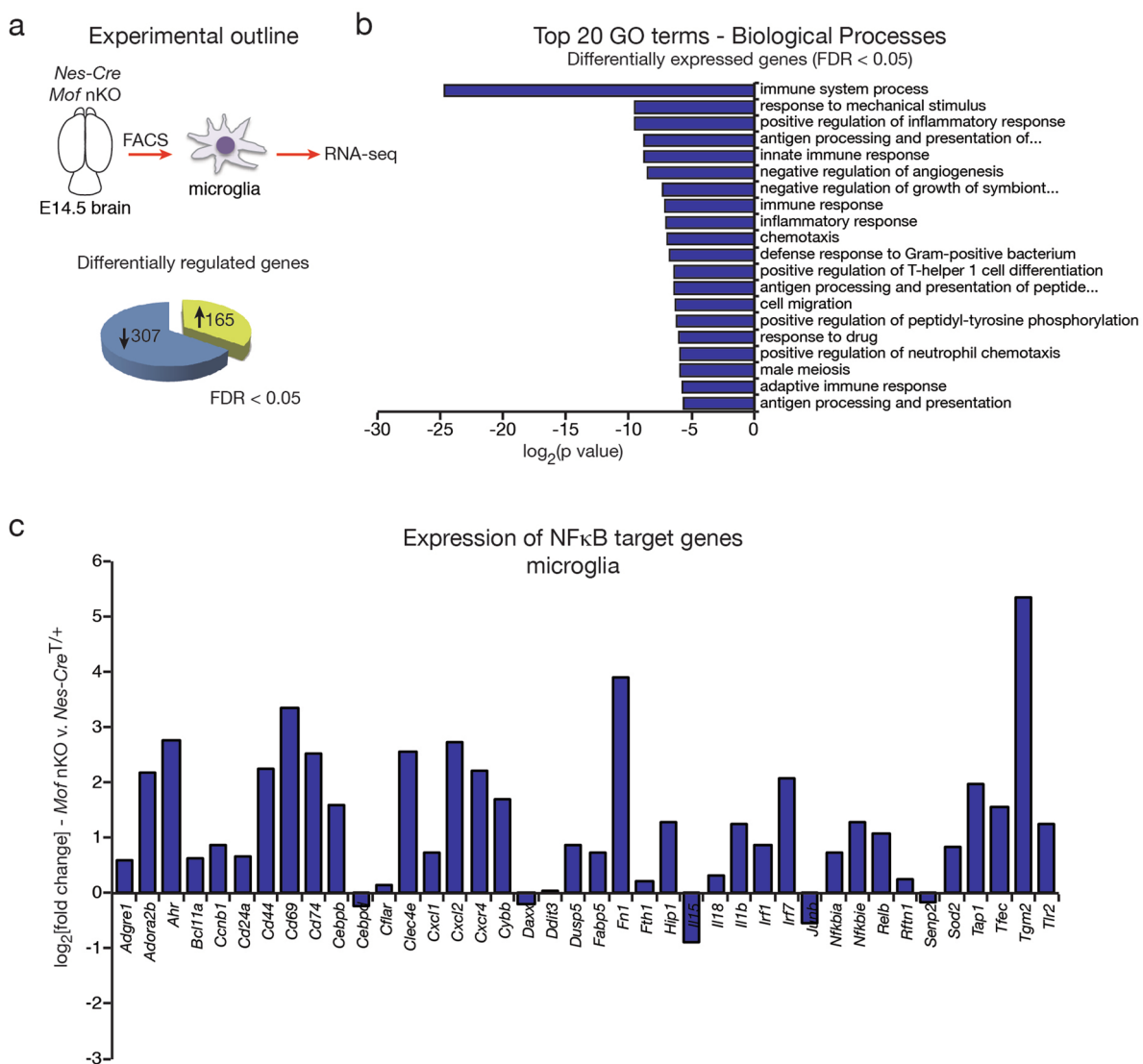
**Extended Data Fig. 5 | Catalytic activity of MOF regulates levels of LCFAs.** **a**, Quantification of mitochondrial DNA via genomic qPCR.  $n = 4$  brains per genotype. **b**, Mitochondrial respiration in cells acutely isolated from E14.5 brains and analysed using the Seahorse analyser.  $n = 3$  *Mof*-nKO, 2 *Mof*<sup>fl/+</sup> *Nes-Cre*<sup>fl/+</sup>, 8 *Cre*-negative. A-antimycin A, F-FCCP, O-oligomycin, R-rotenone. **c**, Quantification of basal respiration rate from Seahorse profiles (panel **b**). **d**, Quantification of ATP-linked respiration from Seahorse profiles (panel **b**). **e**, *Mof* mRNA levels in *Mof*-KO and WT neurosphere cultures following 4-hydroxy-tamoxifen (4OHT) treatment. Exp.1  $n = 6$  *Mof*-KO, 8 WT; Exp.2  $n = 5$  *Mof*-KO, 8 WT neurosphere cultures. **f**, Western blot analysis of MOF, Flag-tagged MOF, Actin, H4K16ac and histone H3 protein levels after re-expression of WT and E350Q MOF in *Mof*-KO and control MEFs. L indicates ladder. Protein sizes are indicated in kDa. 4 independent MEF lines per genotype and per treatment were analysed. **g-k**, Quantification of **g**, Flag expression, **h** Total MOF, **i** endogenous MOF, **j** exogenous MOF and **k** H4K16ac levels in WT and *Mof*-KO cultures. Quantification was carried out from the blots shown in panel **f**. Total MOF levels are a combination of Flag-tagged MOF (exogenous, higher MW) and endogenous MOF. Flag-tagged and endogenous MOF levels were standardized to Actin. H4K16ac levels were standardized to histone H3. Asterisks signify statistical significance at \* $p < 0.05$ , \*\* $p < 0.01$  and \*\*\* $p < 0.001$ . Precise  $p$ -values are provided in Source Data Extended Data Fig. 5.  $n = 4$  independent MEF lines per genotype and per treatment. **l** LCFA levels in WT and *Mof*-KO MEFs after the re-expression of WT and E350Q mutant MOF. 4 MEF lines per genotype and per treatment were analysed. Data are presented as mean  $\pm$  s.e.m. and were analysed using a two-tailed Student's  $t$ -test. Statistical source data and unprocessed blots are shown in Source Data Extended Data Fig. 5.



**Extended Data Fig. 6 | Neural MOF depletion causes breakdown of neural microvasculature.** **a**, Heatmap showing enrichment of pericyte markers in cultured primary brain pericytes. The assay was repeated 3 times (represented by the 3 replicates). **b**, Examples of control *Nes-Cre<sup>T/+</sup>* capillaries. 63 capillaries of 2 *Nes-Cre<sup>T/+</sup>* brains were analysed. **c**, Electron microscopy images of select *Mof*-nKO capillaries. Images i and ii show collapsed capillaries with only remnants visible (marked by red asterisks). Capillaries from *Mof*-nKO brains were highly dilated (iv, v, vi, viii, xi and xii for example, marked with asterisks), often showed breakdown or thinning of the vessel-associated extracellular matrix (red arrows in images iii, iv, v, vii, ix and x), as well as detaching pericytes (black arrows in images vi, vii, ix and x). 79 capillaries of 2 *Mof*-nKO brains were analysed. Full quantifications are provided in Fig. 6c-e. **d**, Quantification of vessel branching (bifurcations). PECAM1 and PDGFR $\beta$  staining was undertaken. Four matching areas of the cortex were imaged, vasculature rendered using the *Imaris* software and the number of bifurcations determined.  $n = 3$  animals per genotype; 2 sections per animal; 4 cortical areas per section. **e**, Quantification of mural cells at blood vessels. E14.5 brain sections were stained for PECAM1 and PDGFR $\beta$  and the ratio of PDGFR $\beta$ :PECAM1 staining intensity was used as a readout for the presence of mural cells.  $n = 2$  animals per genotype. **f**, FACS identification and quantification of endothelial cells (PECAM1<sup>+</sup>, CD102<sup>+</sup>, CD45<sup>-</sup>, CD41<sup>-</sup>) and pericytes (PDGFR $\beta$ <sup>high</sup>, CD11b<sup>-</sup>, CD45<sup>-</sup>, CD41<sup>-</sup>, PECAM1<sup>-</sup>, CD102<sup>-</sup>) in *Mof*-nKO and *Nes-Cre<sup>T/+</sup>* brains. Endothelial cells:  $n = 4$  *Mof*-nKO, 3 *Nes-Cre<sup>T/+</sup>*; Pericytes:  $n = 10$  *Mof*-nKO, 7 *Nes-Cre<sup>T/+</sup>* brains. Data in panels **d** and **f** are presented as mean  $\pm$  s.e.m. and were analysed using a two-tailed Student's *t*-test. Scale bars are provided in  $\mu\text{m}$ . E - endothelial cell, P - pericyte. Statistical source data are shown in Source Data Extended Data Fig. 6.



**Extended Data Fig. 7 | Endothelial cells in *Mof*-nKO brains show normal zonation.** **a**, Experimental design. Endothelial cells (PECAM1<sup>+</sup> CD102<sup>+</sup>) were isolated by FACS and scRNA-seq undertaken using mCEL-Seq2<sup>68,72</sup>. Cells expressing more than 1,500 unique transcripts and the endothelial marker *Flt1* were filtered. A total of 401 endothelial cells were subsequently analysed. **b**, Diffusion map showing zonation profile of endothelial cells isolated from *Mof*-nKO and WT littermates and analysed by scRNA-seq. Pseudotime is interpreted here as a spatial zonation coordinate along the arterial → capillary → venous axis. **c**, Self-organizing-map (SOM) depicting the expression of zoned genes in *Mof*-nKO and WT endothelial cells. The red (*Mof*-nKO) and black (WT) bars below the SOM represent the genotype of each endothelial cell along the arterial → capillary → venous zonation axis. In each of the four quadrants, no difference in the ratio of *Mof*-nKO:WT endothelial cells was observed (Fisher test). NES - normalized enrichment score. A NES of 1 refers to an equivalent ratio *Mof*-nKO and WT cells, a NES > 1 refers to fewer *Mof*-nKO cells, while a NES < 1 refers to increased *Mof*-nKO cells in each quadrant. **d**, Expression of the zoned marker genes *Nr2f2*, *Mfsd2a*, *Tfrc*, *Sema3g* and *Vegfc* across the arterial → capillary → venous axis. 3 animals per genotype were analysed in **b-d**. **e**, Summary of *Tlr* gene expression in microglia / macrophage (cluster 1), endothelial (cluster 6) and pericyte (cluster 19) populations derived from the study of Han and co-workers<sup>41</sup>. **f**, Presence of BODIPY FL-C16 in primary brain pericytes cultured for 18 h in increasing concentrations of BODIPY FL-C16. MFI - median fluorescence intensity. **g**, Experimental design for LCFA tracing experiment presented in Fig. 8b. Statistical source data are shown in Source Data Extended Data Fig. 7.



**Extended Data Fig. 8 | Mof-nKO microglia display an NFκB pro-inflammatory signature.** **a**, Experimental outline. Microglia (CD11b<sup>+</sup>, CD45<sup>medium</sup>, PDGFRβ<sup>+</sup>, PECAM1<sup>+</sup>) were isolated from *Mof*-nKO and *Nes-Cre*<sup>+/+</sup> control brains and analysed via RNA-seq. With a false discovery rate (FDR) cut-off of 0.05, 165 genes were found to be significantly upregulated and 307 genes significantly downregulated. *n* = 3 animals per genotype. **b**, GO term (Biological Processes) analyses for differentially expressed genes (FDR < 0.05) in *Mof*-nKO microglia versus controls. Pathways related to inflammation such as “immune system processes” and “positive regulation of inflammatory response” were significantly enriched. Data were analysed using a Fisher exact test via the DAVID platform<sup>66</sup>. *n* = 3 animals per genotype. **c**, Expression of NFκB target genes in microglia derived from *Mof*-nKO brains compared to *Nes-Cre*<sup>+/+</sup> controls. Data are presented on a log<sub>2</sub> scale. Expression of the majority of NFκB target genes was upregulated in microglia derived from *Mof*-nKO brains. *n* = 3 animals per genotype. Statistical source data are shown in Source Data Extended Data Fig. 8.

## Reporting Summary

Nature Research wishes to improve the reproducibility of the work that we publish. This form provides structure for consistency and transparency in reporting. For further information on Nature Research policies, see [Authors & Referees](#) and the [Editorial Policy Checklist](#).

### Statistics

For all statistical analyses, confirm that the following items are present in the figure legend, table legend, main text, or Methods section.

n/a Confirmed

- The exact sample size ( $n$ ) for each experimental group/condition, given as a discrete number and unit of measurement
- A statement on whether measurements were taken from distinct samples or whether the same sample was measured repeatedly
- The statistical test(s) used AND whether they are one- or two-sided  
*Only common tests should be described solely by name; describe more complex techniques in the Methods section.*
- A description of all covariates tested
- A description of any assumptions or corrections, such as tests of normality and adjustment for multiple comparisons
- A full description of the statistical parameters including central tendency (e.g. means) or other basic estimates (e.g. regression coefficient) AND variation (e.g. standard deviation) or associated estimates of uncertainty (e.g. confidence intervals)
- For null hypothesis testing, the test statistic (e.g.  $F$ ,  $t$ ,  $r$ ) with confidence intervals, effect sizes, degrees of freedom and  $P$  value noted  
*Give  $P$  values as exact values whenever suitable.*
- For Bayesian analysis, information on the choice of priors and Markov chain Monte Carlo settings
- For hierarchical and complex designs, identification of the appropriate level for tests and full reporting of outcomes
- Estimates of effect sizes (e.g. Cohen's  $d$ , Pearson's  $r$ ), indicating how they were calculated

*Our web collection on [statistics for biologists](#) contains articles on many of the points above.*

### Software and code

Policy information about [availability of computer code](#)

#### Data collection

Ingenuity software (v01-12, Qiagen)  
FlowJo software (v9.8.1, v10)  
Image Lab software (v5.2, Bio-Rad Laboratories)  
MIPAV software (v7.3.0, NIH)  
Imaris software (v9.1.0, Bitplane)  
Vision4D software (v2.12.6 Arivis)  
ECIS software (v1.2.78, Applied Biophysics)  
FACSDiVA software (v9, BD)  
Paravision (v6.01)

#### Data analysis

##### RNA Sequencing – E14.5 brains

Libraries were prepared for sequencing using the Illumina ribo-depletion Gold kit and sequenced on the NextSeq 500 instrument. Around 45 million reads were obtained for each sample and mapped to the GRCh38 (mm10) genome assembly using HISAT2 (v2.0.0). Fragments were counted at gene level using featureCounts (v1.5.0) using options (-C -Q 10 -primary -p -B -s 2) upon GENCODE (m4) annotation. Differential expression analysis was performed using edgeR (v3.14). Genes were considered differentially expressed with an FDR cut-off of 0.05 and  $\log_2$  (fold change)  $\geq |0.5|$ . The raw data from these experiments has been uploaded to GEO and is available under GSE138981.

##### RNA Sequencing – Neural, endothelial, pericytes and microglial cells

Libraries were prepared using the Nextera XT DNA library preparation kit (Illumina FC-131-1096) and sequenced on the HiSeq 3000 or NextSeq 500 instruments. Downstream analyses were carried out using the Snakepipes package (v1.0 for neural cells, v1.2.2 for other cell types). Briefly, reads were trimmed via Trimalore (v0.4.5 for neural cells, v0.5.0 for other cell types) and mapped to the GRCh38 (mm10) genome assembly using STAR (v2.6.1). The identity of reads was identified through FeatureCount (v1.6.1 for neural cells, v1.6.4 for other cell types). Differentially expressed genes were identified using DESeq2 (v1.18.1 for neural cells, v1.22.1 for other cell types). The raw data from these experiments has been uploaded to GEO and is available under GSE138981.

**RNA Sequencing – Fatty acid treated brain pericytes**

Reads were trimmed for adapters using TrimGalore (v0.4.4) and mapped to the GRCm38 (mm10) genome assembly using STAR (v2.5.3a). Fragments were counted using featureCounts (v1.5.2) and differential expression was performed using DESeq2 (v1.14.1). Quality checks were performed using deepTools (v3.0.2) and multiQC (v1.2). Differentially expressed genes were used for subsequent analysis with a cut-off of  $FDR < 0.05$ , fold change  $\geq |0.5|$  and base-mean of  $> 50$ . The raw data from these experiments has been uploaded to GEO and is available under GSE138981. Analysis of activated networks were performed using the Ingenuity (Qiagen) analysis.

**scRNA-seq analysis**

Sequencing data were mapped to the mm10 mouse reference genome using bwa (v0.6.2-r126). For the zonation analysis, diffusion pseudotime (dpt) was implemented and diffusion maps generated using the destiny R package (v2.10.2). The number of nearest neighbours,  $k$ , was set to 100. SOMs were generated using the FateID package (v0.1.5) on the basis of the ordering computed by dpt as input. Only genes with  $>3$  counts after size normalization in at least a single cell were included for the SOM analysis. Smooth zonation profiles were derived by applying local regression on normalized transcript counts after ordering cells by dpt. Next, a one-dimensional SOM with 200 nodes was computed on these profiles after z-transformation. Neighboring nodes were merged if the Pearson's correlation coefficient of the average profiles of these nodes exceeded 0.85. The remaining aggregated nodes represent the gene modules shown in the SOM figures. Data from the scRNA-seq analyses have been uploaded to GEO under GSE133079.

**H4K16ac and panH3 chromatin immunoprecipitation (ChIP)**

Enrichment of H4K16ac in Nes-CreT/+ controls over Mof-nKO was determined using the Wilcoxon Rank sum test with the deepStats R package. The raw data are available under GSE138981.

For manuscripts utilizing custom algorithms or software that are central to the research but not yet described in published literature, software must be made available to editors/reviewers. We strongly encourage code deposition in a community repository (e.g. GitHub). See the Nature Research [guidelines for submitting code & software](#) for further information.

## Data

Policy information about [availability of data](#)

All manuscripts must include a [data availability statement](#). This statement should provide the following information, where applicable:

- Accession codes, unique identifiers, or web links for publicly available datasets
- A list of figures that have associated raw data
- A description of any restrictions on data availability

All sequencing data from this study have been uploaded to the NCBI GEO database. Raw data pertaining to RNA-seq experiments are deposited under GSE138981, single cell RNA-seq data under GSE133079 and H4K16ac and histone H3 ChIP-seq data under GSE138981. Published MOF, KANSL3 and MCRC1 ChIP-seq. profiles (Chelmicki et al. 2014) were used in this study and are deposited under GSE51746.

## Field-specific reporting

Please select the one below that is the best fit for your research. If you are not sure, read the appropriate sections before making your selection.

Life sciences       Behavioural & social sciences       Ecological, evolutionary & environmental sciences

For a reference copy of the document with all sections, see [nature.com/documents/nr-reporting-summary-flat.pdf](https://www.nature.com/documents/nr-reporting-summary-flat.pdf)

## Life sciences study design

All studies must disclose on these points even when the disclosure is negative.

Sample size	As per good scientific practice, we aimed for a minimum of 3 biological replicates per experiment. If more than 3 replicates were available (as most experiments were done on embryos where the genotype was unknown before the experiment), all replicates were analyzed and have been included in the presented analyses. The differences between genotypes were generally big enough to be observed with 3 replicates.
Data exclusions	Data were generally not excluded, except in the following circumstances where the experiment failed: 1. The genotype of the embryo could not be determined. 2. The protein concentration of cells used for mass-spec quantification could not be determined. 3. Technical replicate failed, where a $>10$ -fold difference compared to other technical replicates was observed.
Replication	Multiple biological replicates were used for each experiment. Where indicated in the figure legend, the experiment was repeated multiple times. In all instances, there was concordance between experiments as well as between biological replicates.
Randomization	Groups were assigned based on genotype. Wherever possible, genotypes were determined after data collection.
Blinding	Wherever possible, genotypes were determined after data collection.

## Reporting for specific materials, systems and methods

## Materials & experimental systems

## Methods

- n/a  Involved in the study
- Antibodies
- Eukaryotic cell lines
- Palaeontology
- Animals and other organisms
- Human research participants
- Clinical data

- n/a  Involved in the study
- ChIP-seq
- Flow cytometry
- MRI-based neuroimaging

## Antibodies

### Antibodies used

Detailed information is available in Supplementary Table 4  
 Antibody - Source - Clone - Lot - Use - Blocking - Concentration  
 Actin HRP conjugated Santa Cruz sc-1616 n/a G2514 WB 5% milk 1:2000  
 AlexaFluor 488 donkey anti-goat IgG Thermo Fisher A11055 n/a 1869589 IF/FACS as 1° antibody 1:400  
 AlexaFluor 488 goat anti-rabbit IgG Thermo Fisher A11034 n/a 1298480 IF as 1° antibody 1:500  
 AlexaFluor 555 goat anti-rabbit IgG Thermo Fisher A21429 n/a 2090567 IF as 1° antibody 1:400  
 AlexaFluor 555 goat anti-rat IgG Thermo Fisher A21434 n/a IF as 1° antibody 1:500  
 AlexaFluor 647 goat anti-mouse IgG Thermo Fisher A21236 n/a 4119153 IF as 1° antibody 1:800  
 Caspase-3 (activated) Promega G748A n/a 0000189431 IF 0.25% gelatine 1:250  
 CD11b PECy7 conjugated BD 552850 M1/70 8114903, 9079635 FACS 2% FCS 1:200  
 CD13 PECy7 conjugated eBioscience 25-0138 WM-15 E13616-107 FACS 2% FCS 1:100  
 CD31 (PECAM1) Abcam ab28364 n/a GR291622-4 Light sheet 2% FCS 1:250  
 CD31 (PECAM1) Abcam ab28364 n/a GR291622-4 vibratome sections 10% FCS 1:250  
 CD31 (PECAM1) APC conjugated eBioscience 17-0311 390 4330203 FACS 2% FCS 1:250  
 CD41 BV650 conjugated BD 740504 MWReg30 8309559 FACS 2% FCS 1:200  
 CD45 APC conjugated BD 561018 30-F11 7163582 FACS 2% FCS 1:400  
 CD45 PE conjugated BD 553081 30-F11 8060633 FACS 2% FCS 1:300  
 CD102 (ICAM-2) FITC conjugated BD 557444 3C4(mIC2/4) 4028696 FACS 2% FCS 1:250  
 CD102 (ICAM-2) BV421 conjugated BD 740018 3C4(mIC2/4) 8311848 FACS 2% FCS 1:250  
 CTIP2 Abcam ab18465 25B6 GR203038-2 IF 0.25% gelatine 1:500  
 Flag HRP conjugated Sigma A8592 M2 SLBD9930V WB 5% milk 1:3000  
 GAPDH Bethyl A300-641a n/a WB 5% milk 1:1000  
 Phospho-H3 Millipore 06-570 n/a 2724351 IF 0.25% gelatine 1:500  
 H3 Abcam 10799 10799 GR3185917-1 WB 5% milk 1:1000  
 H3 Abcam 10799 10799 GR3185917-1 ChIP BSA 1 µg  
 H4K16ac Millipore 07-329 n/a 2459616 IF 0.25% gelatine 1:200  
 H4K16ac Millipore 07-329 n/a 2459616 WB 5% BSA 1:1000  
 H4K16ac Millipore 07-329 n/a 2459616 ChIP BSA 1 µg  
 KANSL1 Abnova PAB20355 n/a A80306 WB/IP 5% milk 1:1000  
 KANSL2 Sigma HPA038497 n/a R35610, A106354 WB/IP 5% milk 1:500  
 KANSL3 Sigma HPA035018 n/a A96145 WB/IP 5% milk 1:500  
 MCERS1 Proteintech 11362-1-A-P n/a 00017639 WB/IP 5% milk 1:1000  
 MOF (KAT8) Bethyl A300-992A n/a A300-992A-2 WB 5% milk 1:1000  
 MOF (KAT8) Abcam ab200660 n/a GR3247613-110 WB/IP 5% milk 1:1000  
 MSL3 USB129933 n/a L17071753, C17092005 WB/IP 5% milk 1:1000  
 NFκB (pan) Cell Signalling 8242S D14E12 9 WB 5% milk 1:1000  
 NFκB (phosphoS536) Cell Signalling 3033S 93H1 16 WB 5% BSA 1:1000  
 PDGFRβ R&D systems AF1042 n/a GOV0415021, GOV0417041 vibratome sections 10% FCS 1:250  
 PDGFRβ R&D systems AF1042 n/a GOV0415021, GOV0417041 FACS 2% FCS 1:150  
 SATB2 Abcam ab51502 SATB  
 A4B10 GR207579-10 IF 0.25% gelatine 1:50  
 Ter-119 PE conjugated BD 553673 TER-119 5048792 FACS 2% FCS 1:400

### Validation

Caspase-3 (activated)  
 tested on tissue culture cells where cell death was induced by increasing H2O2.

CD11b PECy7 conjugated  
 Widely used monoclonal antibody. Previously tested on bone marrow derived cells. Ref: Sheikh et al. 2015, Blood.

CD13 PECy7 conjugated  
 Tested by observing overlap between CD13 staining and PDGFRb staining in FACS Ref: Extended data Fig. 3c in this study.

CD31 (PECAM1) - Abcam  
 Tested via IF staining to ensure blood vessel localisation. Ref: Sheikh et al. 2019 iScience; Extended data Fig. 6c in this study.

CD31 (PECAM1) APC conjugated

Tested by isolating PECAM1 positive cells and ensuring their endothelial identity by qPCR, scRNA seq and total RNA seq. Also tested by ensuring overlap with other endothelial cell marker, CD102 by FACS. Ref: Sheikh et al. 2019 iScience; Extended data Fig. 3a and 4a in this study.

#### CD41

Widely used monoclonal antibody. Previously tested on bone marrow derived cells. Ref: Sheikh et al. 2015, Blood.

#### CD45

Widely used monoclonal antibody. Tested here by staining lymphocytes from blood. Previously tested on bone marrow derived cells. Ref: Sheikh et al. 2015, Blood.

#### CD102 (ICAM-2)

Tested by isolating CD102 positive cells and ensuring their endothelial identity by qPCR, scRNA seq and total RNA seq. Also tested by ensuring overlap with other endothelial cell marker, PECAM1 (CD31) by FACS. Ref: Sheikh et al. 2019 iScience; Extended data Fig. 3a and 4a in this study.

#### CTIP2

Tested by staining WT E16.5 cortices and ensuring the expression pattern matches the published expected pattern in differentiating neurons - please see Extended data Fig. 2d.

#### Flag HRP conjugated

Tested on cells over-expressing FLAG-tagged MOF versus negative vector - please see Extended data Fig. 5f.

#### Phospho-H3

Tested via IF on proliferating cells. Ensured the nuclear-specific expression in positive cells.

#### H3

Tested via Western Blot. Gave band of correct size (Extended data Fig. 5f). Antibody widely used for ChIP seq. - the Abcam website cites 71 references.

#### H4K16ac

Tested on MOF KO cells (MOF is the only known enzyme for H4K16ac) - the H4K16ac band was lost in Western blot, H4K16ac signal was lost in IF of MOF KO brains (Extended Fig. 2a), and H4K16ac signal was lost in ChIP of MOF KO neural cells (Fig. 3c)

#### KANSL1

Tested in Kansl1 knockdown cells (Ref: Chatterjee et al. 2016, Cell). KANSL1 Western blot signal reduced upon knockdown.

#### KANSL2

Tested in Kansl2 KO brain lysates (Extended data Fig. 2f). KANSL2 signal significantly reduced in Western blot upon Kansl2 KO. Also tested via IP - KANSL2 in E14.5 brain lysate could pull down other members of NSL complex (Extended data Fig 2i).

#### KANSL3

Tested in Kansl3 KO brain lysates (Extended data Fig. 2g). KANSL3 signal significantly reduced in Western blot upon Kansl3 KO. Also tested via IP - KANSL3 in E14.5 brain lysate could pull down other members of NSL complex (Extended data Fig 2i).

#### MCRS1

Previously tested and used for ChIP by the lab (Ref: Chelmicki et al. 2014, eLife). Tested via Western blot in this study - gave the expected band size (Extended data Fig 2e-h). Also tested via IP - MCRS1 in E14.5 brain lysate could pull down other members of NSL complex (Extended data Fig 2i).

#### MOF (KAT8) - Bethyl

Previously published (Ref: Chelmicki et al. 2014, eLife, Chatterjee et al. 2016, Cell). Tested on Mof KO lysates. Expected MOF band lost in Mof KO samples via Western blot (Extended data Fig. 2e).

#### MOF (KAT8) - Abcam

Tested on Mof KO lysates. Expected MOF band lost in Mof KO samples via Western blot.

#### MSL3

Tested via IP - can pull down MOF but not NSL complex members as expected (Extended data Fig. 2i). Previously tested and published by the lab in MSL3 deficient cells (Basilicata et al. 2018 Nature Genetics).

#### NFkB (pan)

Tested via Western blot - gave correct band size. Checked citations provided on the Cell signalling website - antibody used in 1262 studies.

#### NFkB (phospho S536)

Tested via Western blot - gave correct band size. After WB, stripped and stained for pan NFkB - perfectly overlapped with NFkB (phospho S536) staining. Checked citations provided on the Cell signalling website - antibody used in 1507 studies.

#### PDGFR $\beta$

Tested via 1. IF of neural blood vessels - gave correct perivascular staining (Extended data Fig. 6c; Ref: Sheikh et al. 2019 iScience), 2. by FACS isolation for PDGFR $\beta$  cells - analysed identity via scRNAs-seq: correctly isolated pericytes (Ref: Sheikh et al. 2019 iScience).

#### SATB2

Tested by staining WT E16.5 cortices and ensuring the expression pattern matches the published expected pattern in differentiating neurons - please see Extended data Fig. 2d.

Ter-119 PE conjugated

Widely used monoclonal antibody. Previously tested on bone marrow derived cells. Ref: Sheikh et al. 2015, Blood.

## Eukaryotic cell lines

Policy information about [cell lines](#)

Cell line source(s)

established 293T cultures for virus generation  
primary fibroblasts generated in this laboratory directly from mouse embryos  
primary pericyte lines generated within this laboratory directly from adult mouse brains  
B.end3 brain endothelial cell line  
primary cortical neuron cultures directly isolated from E16.5 embryonic brains  
primary neurosphere cell lines generated from E14.5 brains  
primary microglia cell lines from PN-02 brains

Authentication

primary brain pericyte cultures were verified by cell surface markers via flow cytometry as well gene expression levels of known markers (Extended data Fig. 6a).

Mycoplasma contamination

All were negative

Commonly misidentified lines  
(See [ICLAC](#) register)

No easily misidentified lines were used.

## Animals and other organisms

Policy information about [studies involving animals](#); [ARRIVE guidelines](#) recommended for reporting animal research

Laboratory animals

All strains were maintained on a C57BL/6 background, under a 14-hour light and 10-hour dark cycle. Water and standard chow were provided ad libitum. Experimentations were undertaken on a mix of males and females. All experiments were undertaken on E14.5 embryos unless indicated in the text.

Strains:

Nes-Cre (Tronche et al., 1999)

Mof floxed (Thomas et al., 2008)

Caag-Cre-ERT2 (from Jackson lab)

Gt(ROSA)26Sortm4(ACTB-tdTomato,-EGFP)Luo/J (from Jackson lab)

Kansl2 allele (tm1a(EUCOMM)Wtsi) (IKMC consortium)

Kansl3 allele was obtained from Jeannette Rientjes (Monash, Australia)

Wild animals

No wild animals were used.

Field-collected samples

No samples collected from the field

Ethics oversight

All animal studies were performed according to the German animal care and ethics legislation and had been approved by the local government authority, the Committee on Research Animal Care, Regierungspräsidium Freiburg (G-17/102).

Note that full information on the approval of the study protocol must also be provided in the manuscript.

## Human research participants

Policy information about [studies involving human research participants](#)

Population characteristics

Both the "control" samples and the Koolen-de-Vries patients were obtained from aborted/dead 29-week-old human fetuses.

Recruitment

During standard genetic screening, we uncovered one patient with Koolen-de-Vries syndrome (confirmed heterozygous deletion of KANSL1 gene). The patient had died of unknown causes at the time of genetic testing.  
No other recruitment criteria were applied.

Ethics oversight

Ethics approval was obtained from Université Grenoble-Alpes CHU Grenoble and University of Freiburg, Germany.

Note that full information on the approval of the study protocol must also be provided in the manuscript.

## ChIP-seq

Data deposition

Confirm that both raw and final processed data have been deposited in a public database such as [GEO](#).

Confirm that you have deposited or provided access to graph files (e.g. BED files) for the called peaks.

Data access links  
May remain private before publication.

H4K16ac and histone H3 ChIP-seq data - GSE138981  
MOF, KANSL3 and MCRS1 ChIP-seq. profiles (Chelmicki et al. 2014) - GSE51746.

Files in database submission

ChIP-seq data files from GSE138981:

Supplementary file	Size	File type
GSE138981_Cre172_WT_H4K16ac.filtered.log2ratio.over_Cre172_WT_input.bw	221.7 Mb	(http) BW
GSE138981_Cre172_WT_panH3.filtered.log2ratio.over_Cre172_WT_input.bw	233.4 Mb	(http) BW
GSE138981_Cre173_WT_H4K16ac.filtered.log2ratio.over_Cre173_WT_input.bw	193.8 Mb	(http) BW
GSE138981_Cre173_WT_panH3.filtered.log2ratio.over_Cre173_WT_input.bw	210.0 Mb	(http) BW
GSE138981_M621_KO_H4K16ac.filtered.log2ratio.over_M621_KO_input.bw	164.7 Mb	(http) BW
GSE138981_M621_KO_panH3.filtered.log2ratio.over_M621_KO_input.bw	213.9 Mb	(http) BW
GSE138981_M622_WT_H4K16ac.filtered.log2ratio.over_M622_WT_input.bw	223.2 Mb	(http) BW
GSE138981_M622_WT_panH3.filtered.log2ratio.over_M622_WT_input.bw	236.3 Mb	(http) BW
GSE138981_M662_KO_H4K16ac.filtered.log2ratio.over_M662_KO_input.bw	159.5 Mb	(http) BW
GSE138981_M662_KO_panH3.filtered.log2ratio.over_M662_KO_input.bw	200.1 Mb	(http) BW
GSE138981_M663_KO_H4K16ac.filtered.log2ratio.over_M663_KO_input.bw	161.0 Mb	(http) BW
GSE138981_M663_KO_panH3.filtered.log2ratio.over_M663_KO_input.bw	213.7 Mb	(http) BW
GSE138981_M666_WT_H4K16ac.filtered.log2ratio.over_M666_WT_input.bw	250.2 Mb	(http) BW
GSE138981_M666_WT_panH3.filtered.log2ratio.over_M666_WT_input.bw	264.8 Mb	(http) BW

Genome browser session  
(e.g. [UCSC](#))

No longer applicable

## Methodology

Replicates

For each of the H4K16ac and histone H3 ChIP seq, 3 Mof KO replicates, 2 littermate WT replicates and 2 Nes-Cre controls at E14.5 were used. ChIP was carried out on viable primary neural cells isolated from E14.5 brains via FACS.

Sequencing depth

H4K16ac - 245 million reads total  
panH3 - 230 million reads total  
input - 230 million reads total

2x 75 bp reads (pair-end)

Antibodies

H4K16ac Millipore 07-329 ChIP 1 µg  
H3 Abcam 10799 ChIP 1 µg  
Information regarding MOF, KANSL3 and MCRS1 profiles is provided in the published manuscript (Chelmicki et al. 2014)

Peak calling parameters

Read mapping was undertaken using Bowtie2.  
No peak calling was done the H4K16ac or panH3 data. Data were standardized to input.  
Log2 [IP : input] enrichment was calculated using Deeptools.

Data quality

Quality tests:

- read mapping quality (from Bowtie2; filtered > 5)
- correlation between replicates
- checked for loss of H4K16ac in Mof nKO cells
- checked for expected distribution of H4K16ac at gene bodies.

There was no peak calling, thus no quality controls for this were required.

Software

Data were analyzed using the R Snakepipes package (Ref: Bhardwaj et al. 2019 Bioinformatics). This package uses:

1. Bowtie2 for mapping.
2. Deeptools for calculating coverage.
3. Deeptools for generation of heatmaps.

Deepstats were used for statistical testing.

## Flow Cytometry

### Plots

Confirm that:

- The axis labels state the marker and fluorochrome used (e.g. CD4-FITC).
- The axis scales are clearly visible. Include numbers along axes only for bottom left plot of group (a 'group' is an analysis of identical markers).
- All plots are contour plots with outliers or pseudocolor plots.
- A numerical value for number of cells or percentage (with statistics) is provided.

## Methodology

Sample preparation	Brains were acutely isolated from E14.5 embryos and meninges removed. Samples were incubated in the digestion solution (0.13 WU/ml liberase TM (Worthington, Roche 05401119001), 80 U/ml DNase I (NEB), 5 mM MgCl <sub>2</sub> in PBS) and incubated at 37° C in a thermoshaker set at 800 rpm. Twenty minutes later, brains were triturated using a P1000 pipette and incubated for a further 20 minutes. Cells were passed through a 100 µm sieve, washed once in PBS and incubated with the PDGFRβ antibody (Supplementary Table 4) diluted in FACS buffer (2% FCS in PBS) for 30 minutes on ice. After 2 washes in 1 ml of FACS buffer, cells were resuspended in 400 µl of the antibody mix (CD102, PECAM1, CD41, CD45, CD11b, AlexaFluor 488 anti-goat IgG, Supplementary Table 4) diluted in FACS buffer. Zombie dye™ (Biolegend 423106, 1:200) was added as a viability marker. Cells were incubated on ice for 60 minutes, washed twice in PBS and resuspended in 1 ml FACS buffer. Cells were passed through a 100 µm sieve prior to FACS.
Instrument	Flow cytometry analysis: Fortessa (BD) For collecting cells via FACS: ARIA (BD)
Software	Data was collected using the BD FACS Diva software Data was analysed using FlowJo v9.8.1 or v10.
Cell population abundance	Abundance in sorted populations as % Neural cells: 99% Pericytes: 0.067% Endothelial cells: 0.06% Microglia: 0.13%  Abundance in sorted populations as numbers per E14.5 brain. Neural cells: ~5.4 x 10 <sup>6</sup> Pericytes: ~4000 Endothelial cells: ~4000 Microglia: ~7000  Purity was determined in two ways: 1. Analyses of marker gene expression in sorted cell populations (Extended data Fig. 4a) 2. Analyses of cellular phenotype using single cell sequencing of cells isolated using the sorting criteria of neural cells, endothelial cells, pericytes and microglia (see Sheikh et al., 2019 iScience for more details)
Gating strategy	Single cells were collected based on FSC/SSC parameters: FSC-area versus FSC-height -> FSC-height versus FSC-width -> SSC-area versus SSC-height -> FSC-area versus SSC-area. Viable cells were gated using the far red Zombie-dye.  Viable cells were collected based on the following criteria Neural cells: PDGFRb- CD45- CD41- CD11b- PECAM1- CD102- Pericytes:PDGFRb(high) CD45- CD41- CD11b- PECAM1- CD102- Endothelial cells: PECAM1+ CD102+ CD45- CD41- Microglia: CD45(medium) CD11b+ PECAM1- PDGFRb-

Tick this box to confirm that a figure exemplifying the gating strategy is provided in the Supplementary Information.

## Magnetic resonance imaging

### Experimental design

Design type	Whole E14.5 embryos with the genotypes wild type, Nes-Cre T/+, Mof-nKO, Kansl2-nKO and Kansl3-nKO were fixed in 4% paraformaldehyde supplemented with 2 mM gadolinium (III) for 10 days at 4°C. After 10 days, samples were embedded in 1% low melt agarose supplemented with 2 mM gadolinium (III) and imaged on a 9.4 tesla small bore animal scanner (BioSpec 94/21, Bruker Biospin, Ettlingen, Germany) using a dedicated mouse quadrature-resonator (Bruker, Ettlingen, Germany). The MRI protocol consisted of two localizers and a T2-weighted TurboRARE (Rapid Acquisition with Relaxation Enhancement) 3D sequence. The TurboRARE 3D sequence that was used to delineate the ventricles featured a FOV of 13x13x13mm; a matrix size of 256x256x64 pixels and a resolution of 51x51x203 µm (TR/TEeff/FA: 1800ms/36 ms/180°). Volumetric analyses were undertaken using the MIPAV software (v7.3.0, NIH)
Design specifications	64 sections in a dorsal - ventral direction were taken.
Behavioral performance measures	N/A- animals were fixed.

### Acquisition

Imaging type(s)	structural
Field strength	9.4
Sequence & imaging parameters	The MRI protocol consisted of two localizers and a T2-weighted TurboRARE (Rapid Acquisition with Relaxation

Sequence & imaging parameters  Enhancement) 3D sequence. The TurboRARE 3D sequence that was used to delineate the ventricles featured a FOV of 13x13x13mm; a matrix size of 256x256x64 pixels and a resolution of 51x51x203  $\mu\text{m}$  (TR/TEeff/FA: 1800ms/36 ms/180°).

Area of acquisition  The whole embryo was imaged.

Diffusion MRI  Used  Not used

## Preprocessing

Preprocessing software  Paravision v6.01

Normalization  Data were not normalized at the preprocessing stage as the MRI scans were done on fixed embryos. The same number of slices and the exact same number of voxels were acquired for each image.

Normalization template  Data were not normalized.

Noise and artifact removal  No noise or artifact removal was performed.

Volume censoring  No volume censoring was performed.

## Statistical modeling & inference

Model type and settings  Changes in the ventricular volume relative to genotype.

Effect(s) tested  ventricular volume.  
 statistical test: two-tailed Student's t-test.  
 For each of the ventricles, each nKO was directly compared to the Nes-Cre control in a pairwise comparison.

Specify type of analysis:  Whole brain  ROI-based  Both

Anatomical location(s)  The ventricular system is easily distinguishable in scans. This was manually annotated for the MIPAV software to allow for volumetric analysis.

Statistic type for inference (See [Eklund et al. 2016](#))  Voxels were used to quantify volume.

Correction  Only 2 groups were compared for each ventricle: the Nes-CreT/+ control samples were compared (pairwise comparisons), in turn, with each of the nKO using a two-tailed Student's t-test.

## Models & analysis

n/a  Involved in the study

Functional and/or effective connectivity

Graph analysis

Multivariate modeling or predictive analysis

Graph analysis  The ventricular volume is plotted against genotype.